UNIVERSITÀ DELLA CALABRIA

Facoltà di Scienze Matematiche, Fisiche e Naturali

Dottorato di Ricerca in Fisica
XIX ciclo
(settore disciplinare Fis/04)

STUDY OF RARE BEAUTY DECAYS WITH ATLAS DETECTOR AT LHC AND MDT CHAMBER PERFORMANCES

Dr. Antonio Policicchio

Supervisore:
Prof. G. CROSETTI

Coordinatore:
Prof. G. CHIARELLO

ANNO ACCADEMICO 2005/2006

to my family

"Physicists are the Peter Pans
of the human race.
They never grow up,
they keep their curiosity."
I. I. Rabi

Acknowledgments

A PhD thesis, the result of three years' work, cannot be accomplished without the help and advice of many people. With the following few words I would like to thank everybody, hoping I won't forget anyone.

Surely the first person to thank is my supervisor Prof. Giovanni "Nanni" Crosetti. In these three years of doctorate Nanni has followed step by step my research activity. His precious advice have always been fundamental to face and solve the different problems. Discussions concerning the issues of high energy physics have been a stimulus for a lot of in-depth study. I want to say thank you to him above all for the appreciation he has showed me.

I owe to Prof. Giancarlo Susinno, leader of ATLAS CS-INFN group (the "boss"), the possibility of having the chance to live the fantastic experience of a doctorate. He has trusted me since I decided to start the difficult path of high energy physics. Through all these years I have always tried to do my best to show him my gratitude. His scientific enthusiasm and his passion for the physics have been the best model I could get.

I want also to thank Prof. Marco Schioppa. The ageing tests have given me the chance to deepen my knowledge on new topics. Working with him has taught me how to love the research carried on in a proper way and how to discover, even with a great amount of work, the truth that lies behind experimental data. His willingness to listen my requests and remarks has been and will always be a very good model.

With Prof.ssa Laura La Rotonda we spent hours at the pc trying to understand the mysteries of GRID! They were useful hours to test my knowledge and to learn something more. Her advice and her helpfulness through these years have been very important.

The "theoretical" doubts I had at the beginning of my studies on rare beauty decays would be still unresolved without arguing with Prof. Alessandro Papa. His knowledge always amazes me.

I want to thank Prof. Enrico Tassi. Discussing with him on some particularly difficult problem has been extremely useful.

I thank Dott.ssa Anna Mastroberardino and Dott.ssa Marcella Capua: their appraisal for the work done has always been rewarding.

I want to thank Prof. Roberto Fiore, INFN group Head, for his patience in signing all the mission authorizations!

How could it be possible not to thank the first person to be informed during these years about all the things going on, all the news, the person who always listened to me, always helped me when I was in need, always gave me the best

advice? Obviously I mean the excellent Dott.ssa Evelin Meoni. I thank her beyond what is a professional relationship, I consider her as a friend.

In the following lines I would like to thank the persons that helped me in the single studies described in this dissertation.

The advice, helpfulness and professional competence in clearing doubts up, mainly in the initial stage of the study on rare beauty decays, of Maria Smizănská (coordinator of ATLAS B-Physics group) have been very useful. I want to thank her. I strongly thank Dott. Pavel Reznicek (Charles University, Prague), Dott. James Catmore (Lancaster University) and Dott. Alessandro De Salvo (La Sapienza University, Rome) for their useful suggestion and the help they gave me during my first step in using GRID tools.

I thank Dott. Fabio Cerutti (LNF Frascati, H8 Muon Test Beam coordinator) for his suggestions during the study of the Muon Spectrometer intrinsic spatial resolution. I thank Dott. Stefano Rosati (La Sapienza University, Rome), Dott.ssa Evelin Meoni (again), Dott.ssa Daniela Rebuzzi(Pavia University) and Dott. Giuseppe Avolio (INFN-Cosenza): working with them was rewarding.

I thank Dott. Paolo Branchini, Dott. Silvestro Di Luise, Dott. Fabrizio Petrucci, Dott. Enrico Graziani, Dott. Antonio Passeri (INFN-Roma3), Dott.ssa Daniela Salvatore, Dott.ssa Evelin Meoni (again!), Dott.ssa Concetta Mazzotta and Gianfranco Morello (INFN-Cosenza). Working with them to the test of the MDT chambers was pleasant and fruitful.

Among the INFN-Cosenza group, I want to say thank you to my colleagues Cristina Adorisio, Federico Zema and Salvatore Fazio as well as to the technicians Franco, Vittorio and Paola.

Last but not least, I must thank my parents: to put up my sudden changes of mood mustn't have been easy. They are fantastic parents. And I must say thank you also to Giovanna: she has always listened to me and has been of great comfort (in spite of some snorting!).

Now, as the PhD is approaching to its end, I'm facing a transition phase. I would like to mark that I really enjoyed working in the ATLAS interesting and various environment, and I really hope that I will be able to participate to such beautiful and challenging project for many more years!

Contents

Introduction

The Large Hadron Collider (LHC) is a proton-proton collider that will operate at a center of mass energy of 14 TeV and at a maximum luminosity of $L = 10^{34} cm^{-2} s^{-1}$. The LHC will reproduce interactions similar to those which existed when the universe was only $\sim 10^{-12} s$ old, conditions which have not been achieved in any previous collider. The primary goals of the LHC project are to discover the origin of particle masses, to explain why different particles have different masses and to search for new phenomena beyond the Standard Model. Also heavy quark systems and precision measurements on Standard Model parameters will be subject of LHC physics studies.

ATLAS (A Toroidal LHC ApparatuS) is one of the two LHC general purpose experiments. The guiding principle in optimizing the ATLAS experiment has been maximizing the discovery potential for New Physics such as Higgs bosons and supersymmetric particles, while keeping the capability of high precision measurements of known objects such as heavy quarks and gauge bosons.

The rate of B-hadron production at the LHC is enormous thanks to the large cross-section for b-quark production and the high luminosity of the machine ($L = 10^{33} cm^{-2} s^{-1}$ even at initial low luminosity). About 1% of collisions produce a b-quark pair. An important range of B-Physics studies has therefore been planned for the ATLAS experiment. An important aim of the B-Physics work is to test the Standard Model through precision measurements of B-hadron decays that together will over-constrain the CKM matrix, to give indirect evidence for New Physics. This program includes: precise measurements of CP violation in B-meson decays, precise measurements of the periods of flavour oscillations in B_s^0 as well as B_d^0 mesons, searches and measurements of very rare decays. Certain rare decays, for which the decay products themselves provide a distinctive signature that can be used in the trigger, will be studied very effectively in ATLAS. These so-called "self-triggering" modes include decays of the type $B \to \mu^+\mu^-(X)$. Such decays involve flavour changing neutral currents and are strongly suppressed in the Standard Model, which predicted branching ratios are typically in the range $10^{-5} - 10^{-9}$. New Physics might result in significant enhancements compared to the Standard Model predictions and thus their measurement provide an indirect search for New Physics.

This thesis presents a study on simulated data for the two semileptonic decays $B \to K^+\mu^+\mu^-$ and $B \to K^{*+}\mu^+\mu^-$. The goal of the study has been to evaluate the ATLAS experiment sensitivity to New Physics discover through precise measurements of these rare semileptonic beauty decays. The ATLAS sensitivity to their branching ratios has thus been assessed. Moreover, the sig-

nal reconstruction and the background rejection strategies for the next ATLAS data taking have been outlined.

Also two studies, on the ATLAS Muon Spectrometer performance and on the ageing and tracking capability in a high rate background of Monitored Drift Tube (MDT) precision chambers, are presented.

The Muon Spectrometer defines the overall dimensions of the ATLAS detector. The outer chambers of the barrel are at a radius of about 11 m and the third layer of the forward muon chambers is located about 23 m from the interaction point. The effort of the INFN-Cosenza group to the spectrometer realization and test was enormous. The test on H8 beam line at CERN during 2004 has given the possibility to test and validate not only the performance of the single spectrometer subsystem but also their integration. The analysis presented in this thesis is dedicated to the evaluation of the intrinsic spatial resolution of the tracking system. The beam momentum has been also measured, for the first time, by means of the Muon Spectrometer. In addition, a comparison of experimental results with a GEANT4-based simulation has constituted an important validation test of the official ATLAS simulation software.

The precision tracking chambers of the Muon Spectrometer have to operate for more than 10 years in the harsh LHC background, due mainly to low energy neutrons and photons. Ageing effects and difficulties in tracking can appear, moreover in view of the upgrade to Super-LHC. Neutron and gamma irradiation tests of the muon system precision chambers have been performed during 2005 at Enea Casaccia research center, in order to study the MDT behaviour after massive irradiation and in a high rate background environment. Analysis on accumulated charge spectra for these tests are here presented.

Chapter 1 is dedicated to the physics of rare semileptonic decays of beauty hadrons. The effective Hamiltonian, in the heavy quark limit, is introduced and the methods to compute the perturbative short-distance and the non-perturbative long-distance contributions are discussed. Results obtained in some supersymmetric models are shown pointing out differences with respect to Standard Model predictions. Current experimental results from beauty factories are also shown.

Chapter 2 provides a general overview of the experimental facilities. The LHC and the ATLAS experiment are described. A section has been dedicated to the description of the ATLAS trigger requirements for B-physics.

Chapter 3 describes the official ATLAS software, the simulation and the reconstruction of beauty events. Also the LHC Computing Grid project is briefly mentioned. Grid facilities have been extensively used for this work.

In **Chapter 4** the analysis results on simulated rare $B \to K^+\mu^+\mu^-$ and $B \to K^{*+}\mu^+\mu^-$ decays are shown. Signal reconstruction and characterization, background rejection and estimation are described in great detail. Moreover, the ATLAS sensitivity to their branching ratio measurements and the possibility to discover New Physics signals are outlined.

Chapter 5 is completely dedicated to the analysis of the experimental H8

test beam data of the summer 2004. The experimental setup is described and results of the tracking system intrinsic resolution measurements are given and compared with GEANT4 simulation.

In **Chapter 6**, after an overview of expected background rate in ATLAS, the neutron and gamma ageing and tracking in a high rate environment tests are described. Accumulated charge spectra analysis strategy and results are shown.

Finally, in the last part, some general conclusions and considerations are given.

Chapter 1

Physics of Rare Semileptonic Decays of Beauty Hadrons

In this chapter the flavour structure of the Standard Model is outlined. The Cabibbo-Kobayashi-Maskawa mixing matrix and the importance of studying flavour changing neutral current $b \to s l^+ l^-$ transitions are discussed. The necessary tools to include QCD perturbative corrections in weak decays and the effective Hamiltonian theory are introduced. In particular rare $B \to K^{(*)} l^+ l^-$ decays are explained following the approach in [1] and [21]. Also supersymmetric model predictions about these decays are summarized and finally current experimental measurements from B-factories are sketched.

1.1 Introduction

The careful investigation of the weak meson decays is mandatory for further testing of the Standard Model (SM) ([2]). Of particular importance is the determination of all Cabibbo-Kobayashi-Maskawa (CKM) matrix elements, the understanding of direct CP violation in nonleptonic K decays, CP violation in the B-system, the search for new CP violation sources, and the rare K and B-decays that are sensitive to the effects of virtual heavy particles, such as the top quark and new particles. Rare B-decays are an important testing ground of the Standard Model and offer a complementary strategy in the search of New Physics by probing the indirect effects of new interactions in higher order processes. The probing of loop-induced couplings can provide a means of testing the detailed structure of the SM at the level of radiative corrections. In particular, $FCNC$ involving $b \to s l^+ l^-$ transitions occur only at the loop level in the SM and hence provide an excellent probe of new indirect effects by yielding informations on the masses and coupling of the virtual particles running in the loops and this explains the attention they have received in recent years.

Since hadrons are involved in the decays, QCD effects are unavoidable and must be understood. To accomplishing this task one employs two tools of quantum field theory: the Operator Product Expansion (OPE) and the

renormalization group. In the OPE an amplitude A for a process such as a weak decay may be written as

$$A = \langle \mathcal{H}_{\text{eff}} \rangle = \sum_i C_i(\mu, M_W) \langle Q_i(\mu) \rangle \tag{1.1.1}$$

Here Q_i are local operator and C_i are the Wilson coefficients. Both Q_i and C_i depend on the QCD renormalization scale μ, and C_i depends on the mass of the W boson and the masses of other heavy particles such as the top quark. The amplitude in (1.1.1) can be view more intuitively as an effective Hamiltonian for the process considered, with Q_i the effective vertexes and C_i the corresponding coupling constants.

OPE separates the full calculation into two distinct parts: the long distance (LD) contributions contained in the operator matrix elements and the short distance (SD) physics described by the Wilson coefficients. The renormalization scale μ separates the two regimes and it is typically chosen to be of the order of a few GeV for the decays of B-mesons. The physical amplitude A cannot depend on μ. The μ dependence of the Wilson coefficients has to cancel the μ dependence present in $\langle Q_i(\mu) \rangle$. The long distance part in equation (1.1.1) deals with low energy strong interactions and therefore poses a very difficult problem. Many approaches have been used to obtain quantitative estimates of hadronic matrix elements ([16]). Despite these efforts the problem is not yet solved satisfactorily and is the most important source of theoretical uncertainty.

In contrast, the short distance QCD interaction can be analyzed using well-established field theory methods. Due to the asymptotic freedom of QCD the strong interaction effects at short distance are calculable in perturbation theory in powers of the strong coupling $\alpha_s(\mu)$. In fact $\alpha_s(\mu)$ is small in the full range of relevant short distance scales of $O(M_W)$ down to $O(1GeV)$ to serve as a reasonable expansion parameter. However, the presence of large logarithms $ln(M_W/\mu)$ multiplying $\alpha_s(\mu)$ in the calculation of Wilson coefficients spoils the validity of the usual perturbation series. It is therefore necessary to perform a renormalization group analysis that allows an efficient summation of logarithmic terms. The usual perturbation theory is replaced by a renormalized-group improved perturbation theory in which the leading order (LO) corresponds to summing the leading logarithm terms $\sim \alpha_s(\mu)^n [\alpha_s(\mu) ln(M_W/\mu)]^n$. Then at next to leading order (NLO), all terms of the form $\sim \alpha_s(\mu)^n [\alpha_s(\mu) ln(M_W/\mu)]^{n-1}$ are summed in addition, and so on. The unphysical left-over μ-dependencies in the decay amplitudes and branching ratios resulting from the truncation of the perturbative series are considerably reduced by including NLO or $NNLO$ corrections ([14]).

1.2 The Flavour Sector in Standard Model

In the quark sector of the Standard Model ([4],[5]), there are six coloured quarks organized in 3 families. The left-handed quarks are put into weak

isospin $SU(2)_L$ doublets

$$\begin{pmatrix} q_{up} \\ q'_{down} \end{pmatrix}_{i=1,2,3} = \begin{pmatrix} u \\ d' \end{pmatrix}_L, \begin{pmatrix} c \\ s' \end{pmatrix}_L, \begin{pmatrix} t \\ b' \end{pmatrix}_L \tag{1.2.1}$$

and the corresponding right-handed fields transform as singlets under $SU(2)_L$. Under the weak interaction an up-quark (with $Q_u = 2/3e$) can decay into a down-quark (with $Q_d = -1/3e$) and a W^+ boson. This process is described by charged current, given as

$$J_\mu^{CC} = \frac{e}{\sqrt{2}\sin\theta_W} \left(\bar{u}, \bar{c}, \bar{t}\right)_L \gamma_\mu V_{\text{CKM}} \begin{pmatrix} d \\ s \\ b \end{pmatrix}_L \tag{1.2.2}$$

where the subscript $L = (1 - \gamma_5)/2$ denotes the left-handed projector and reflects the $V-A$ structure of J_μ^{CC} in the SM. Here the weak mixing Weinberg angle θ_W is a parameter of the SM, which is measured with high accuracy ([6]). The CKM matrix ([7]) describes the mixing between different quark flavours. It contains the angles describing the rotation between the eigen-vectors of the weak interaction (q') and the mass eigen-states (q)

$$\begin{pmatrix} d' \\ s' \\ b' \end{pmatrix} = V_{CKM} \begin{pmatrix} d \\ s \\ b \end{pmatrix} . \tag{1.2.3}$$

Symbolically, V_{CKM} can be written as

$$V_{\text{CKM}} \equiv \begin{pmatrix} V_{ud} & V_{us} & V_{ub} \\ V_{cd} & V_{cs} & V_{cb} \\ V_{td} & V_{ts} & V_{tb} \end{pmatrix} . \tag{1.2.4}$$

In general all the entries are complex numbers, only restricted by unitarity $V_{CKM}V_{CKM}^\dagger = 1$. The matrix depends on three angles and six phases. The freedom to redefine the phases of the quark mass eigen-states can be used to remove five of the phases, leaving a single physical phase, the Kobayashi-Maskawa phase, that is responsible for all CP violation in meson decays in the Standard Model. They are parameters of the SM and can only be obtained from the experiments. The values of the individual matrix elements can in principle all be determined from weak decays of the relevant quarks, or, in some cases, from deep inelastic neutrino scattering. Assuming only three quark generations, the 90% confidence limits on the magnitude of the elements of the complete matrix are ([6]):

$$V_{\text{CKM}} \equiv \begin{pmatrix} 0.9739 \textit{ to } 0.9752 & 0.221 \textit{ to } 0.227 & 0.0029 \textit{ to } 0.0045 \\ 0.221 \textit{ to } 0.227 & 0.9730 \textit{ to } 0.9744 & 0.039 \textit{ to } 0.044 \\ 0.0048 \textit{ to } 0.014 & 0.037 \textit{ to } 0.043 & 0.9990 \textit{ to } 0.9992 \end{pmatrix} . \tag{1.2.5}$$

Some parametrizations of V_{CKM} can be seen in [6].

A useful parametrization of the CKM matrix has been proposed by Wolfenstein ([8])

$$V_{\text{Wolfenstein}} = \begin{pmatrix} 1-\frac{1}{2}\lambda^2 & \lambda & A\lambda^3(\rho-i\eta) \\ -\lambda & 1-\frac{1}{2}\lambda^2 & A\lambda^2 \\ A\lambda^3(1-\rho-i\eta) & -A\lambda^2 & 1 \end{pmatrix} + \mathcal{O}(\lambda^4) \ . \quad (1.2.6)$$

The parameters A, λ, ρ and the phase η are real numbers. λ is related to the Cabibbo angle through $\lambda = \sin\theta_C$ ([6]), which describes the quark mixing with 2 quark families (4 flavours). Since $\lambda \simeq 0.221$, the relative sizes of the matrix elements in (1.2.4) can be read off from Eq. (1.2.6). As can be seen, the diagonal entries are close to unity and the more off-diagonal they are, the smaller is the value. The unitarity of the CKM matrix implies various relations between its elements ([9]). Of particular interest is the relation

$$V_{ud}V_{ub}^* + V_{cd}V_{cb}^* + V_{td}V_{tb}^* = 0. \quad (1.2.7)$$

In terms of the Wolfenstein parametrization the matrix elements involved in (1.2.7) are:

$$V_{ud} = 1 - \frac{1}{2}\lambda^2 - \frac{1}{8}\lambda^4 + O(\lambda^6) \quad (1.2.8)$$

$$V_{ub} = A\lambda^3(\varrho - i\eta) \quad (1.2.9)$$

$$V_{cd} = -\lambda + \frac{1}{2}A^2\lambda^5[1 - 2(\varrho + i\eta)] + O(\lambda^7) \quad (1.2.10)$$

$$V_{cb} = A\lambda^2 + O(\lambda^8) \quad (1.2.11)$$

$$V_{td} = A\lambda^3\left[1 - (\varrho + i\eta)(1 - \frac{1}{2}\lambda^2)\right] + O(\lambda^7) = A\lambda^3(1 - \bar{\varrho} - i\bar{\eta}) \quad (1.2.12)$$

$$V_{tb} = 1 - \frac{1}{2}A^2\lambda^4 + O(\lambda^6) \quad (1.2.13)$$

with

$$\bar{\varrho} = \varrho(1 - \frac{\lambda^2}{2}), \qquad \bar{\eta} = \eta(1 - \frac{\lambda^2}{2}). \quad (1.2.14)$$

The relation (1.2.7) can be represented as a "unitarity" triangle in the complex plane $(\bar{\varrho}, \bar{\eta})$ as show in Figure 1.1.

The unitarity triangle together with $|V_{us}|$ and $|V_{cb}|$ gives a full description of the CKM matrix. The angles and the sides of such triangle are phase convention independent and are physical observables. Their measurement is one of the most important issues at the B-factories.

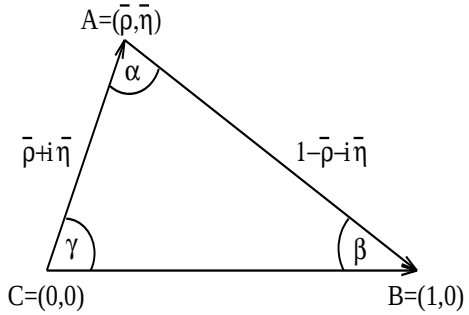

Figure 1.1: *Unitarity triangle.*

1.3 Flavour Changing Neutral Current Transitions

In the SM, the neutral current mediated through the gauge bosons Z^0, γ, g does not change flavour. Therefore, the so-called Flavour Changing Neutral Currents ($FCNC$) do not appear at tree level and are only due to loop effects. The quarks are grouped into *light* (u, d, s) and *heavy* (c, b, t) ones in the sense, that the mass of a heavy quark is much larger than the typical scale of the strong interaction, $\Lambda_{QCD} \sim 200\ MeV$.

The sixth quark, the top, is too heavy to build bound states because it decays too fast. The b-quark is the heaviest one building hadrons. The attention is here concentrated on $B \equiv (bq)$ meson transitions with $q = u, d, s$. Since the b-quark is heavy, the B-system is well suited for a clean extraction of the underlying short-distance dynamics. In B-decays, unlike the K-system, long-distance effects are expected to play a less important role except where such effects are present in a resonant form.

The motivation to investigate $b \to s$ transitions is to improve the knowledge of the CKM matrix elements and to study loop effects. The leading loops are sensitive to the masses and other properties of the internal virtual particles like e.g. the top. They can be heavy and therefore can be studied in a rare B-decay at energies which are much lower than the ones necessary for a direct production of such particles. The idea is to compare the SM based prediction for a rare B-decay with an experiment: a possible deviation gives a hint not only for the existence, but also for the structure of the "New Physics" beyond the SM.

A typical diagram for $b \to s$ is displayed in Figure 1.2 from where the CKM couplings can be directly read off.

1.4 The Effective Hamiltonian Theory

The main tool to calculate rare B-decays in the quantum field theory framework, is the effective Hamiltonian theory. It is a two step program, starting with an operator product expansion and performing a Renormalization Group

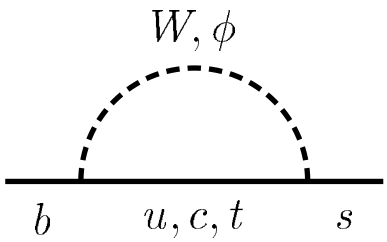

Figure 1.2: *A FCNC $b \to s$ diagram.*

Equation (*RGE*) analysis. The necessary machinery has been developed over the last years, see e.g. [12],[10],[13],[14],[11] as references.

The derivation starts as follows. If the masses of the internal particles m_i are much larger than the external momenta p ($m_i^2 \gg p^2$), then the heavy particles ($W, t, \phi, \ldots$) can be *integrated out*. This concept takes a concrete form with the functional integral formalism. It means that the heavy particles are removed as dynamical degrees of freedom from the theory, hence their fields do not appear in the (effective) Lagrangian. Their residual effect lies in the generated effective vertexes. In this way an effective low energy theory can be constructed from a full theory like the SM. A well known example is the four-Fermi interaction ([15]), where the W-boson propagator is made local for $q^2 \ll m_W^2$ (q denotes the momentum transfer through the W):

$$-i\frac{g_{\mu\nu}}{q^2 - m_W^2} \to i g_{\mu\nu}\left(\frac{1}{m_W^2} + \frac{q^2}{m_W^4} + \ldots\right) , \tag{1.4.1}$$

where the dots denote terms of higher order in $1/m_W$.

Performing an OPE for QCD and electroweak interactions, the effective Hamiltonian for a generic weak transition in the SM can be obtained by integrating out W, t, ϕ. Up to $\mathcal{O}(\frac{1}{m_W^4})$ it is given as:

$$\mathcal{H}_{eff} = -4\frac{G_F}{\sqrt{2}}\lambda_t \sum_{i=1}^{10} C_i(\mu) Q_i(\mu) , \tag{1.4.2}$$

where the weak coupling $g_W = \frac{e}{\sin\theta_W}$ is collected in the Fermi constant G_F

$$\frac{G_F}{\sqrt{2}} = \frac{g_W^2}{8m_W^2} , \tag{1.4.3}$$

$$G_F = 1.16639 \cdot 10^{-5}\ \mathrm{GeV}^{-2} . \tag{1.4.4}$$

The amplitude for a decay is the evaluation of the effective Hamiltonian between initial and final states:

$$A = \langle \mathcal{H}_{\rm eff} \rangle \sim \sum_i C_i(\mu, M_W) \langle Q_i(\mu) \rangle \tag{1.4.5}$$

The on-shell operator basis for $\Delta B = 1$ transitions, where $\Delta B = 1$ refers to the variation of the *beauty* quantum number, is chosen to be ([12]):

Current-Current Operators (Figure 1.3 (a)):

$$Q_1 = (\bar{q}_i c_j)_{\rm V-A} (\bar{c}_j b_i)_{\rm V-A} \qquad Q_2 = (\bar{q} c)_{\rm V-A} (\bar{c} b)_{\rm V-A} \tag{1.4.6}$$

$$Q_1^u = (\bar{q}_i u_j)_{\rm V-A} (\bar{u}_j b_i)_{\rm V-A} \qquad Q_2^u = (\bar{q} u)_{\rm V-A} (\bar{u} b)_{\rm V-A} \tag{1.4.7}$$

QCD-Penguins Operators (Figure 1.3 (b)):

$$Q_3 = (\bar{q} b)_{\rm V-A} \sum_{q' \neq t} (\bar{q}' q)_{\rm V-A} \qquad Q_4 = (\bar{q}_i b_j)_{\rm V-A} \sum_{q' \neq t} \left(\bar{q}'_j q'_i\right)_{\rm V-A} \tag{1.4.8}$$

$$Q_5 = (\bar{q} b)_{\rm V-A} \sum_{q' \neq t} (\bar{q}' q')_{\rm V+A} \qquad Q_6 = (\bar{q}_i b_j)_{\rm V-A} \sum_{q' \neq t} \left(\bar{q}'_j q'_i\right)_{\rm V+A} \tag{1.4.9}$$

Electroweak-Penguins Operators (Figure 1.3 (c)):

$$Q_7 = \frac{3}{2} (\bar{s} d)_{\rm V-A} \sum_q e_q (\bar{q} q)_{\rm V+A} \quad Q_8 = \tfrac{3}{2} (\bar{s}_i d_j)_{\rm V-A} \textstyle\sum_q e_q (\bar{q}_j q_i)_{\rm V+A} \tag{1.4.10}$$

$$Q_9 = \frac{3}{2} (\bar{s} d)_{\rm V-A} \sum_q e_q (\bar{q} q)_{\rm V-A} \quad Q_{10} = \tfrac{3}{2} (\bar{s}_i d_j)_{\rm V-A} \textstyle\sum_q e_q (\bar{q}_j q_i)_{\rm V-A} \tag{1.4.11}$$

Magnetic-Penguins Operators (Figure 1.3 (d)):

$$\begin{aligned} Q_{7\gamma} &= \frac{e}{8\pi^2} m_b \bar{q}_i \sigma^{\mu\nu} (1+\gamma_5) b_i F_{\mu\nu} \\ Q_{8G} &= \frac{g}{8\pi^2} m_b \bar{q}_i \sigma^{\mu\nu} (1+\gamma_5) T^a_{ij} b_j G^a_{\mu\nu} \end{aligned} \tag{1.4.12}$$

Semi-Leptonic Operators (Figure 1.3 (e,f)):

$$Q_{9V} = (\bar{b} q)_{V-A} (\bar{l} l)_V \qquad Q_{10A} = (\bar{b} q)_{V-A} (\bar{l} l)_A \tag{1.4.13}$$

$$Q(\bar{\nu}\nu) = (\bar{q} q)_{V-A} (\bar{\nu}\nu)_{V-A} \qquad Q(\bar{\mu}\mu) = (\bar{q} q)_{V-A} (\bar{\mu}\mu)_{V-A} \tag{1.4.14}$$

where color indices, i and j, in color singlet currents have been suppressed for simplicity, the $V \pm A$ form refers to the Lorentz structure $\gamma_\mu(1 \pm \gamma_5)$ and $\sigma_{\mu\nu} = \frac{i}{2}[\gamma_\mu, \gamma_\nu]$. T^a, $a = 1 \ldots 8$ are the generators of QCD and $F^{\mu\nu}$, $G^{a\mu\nu}$

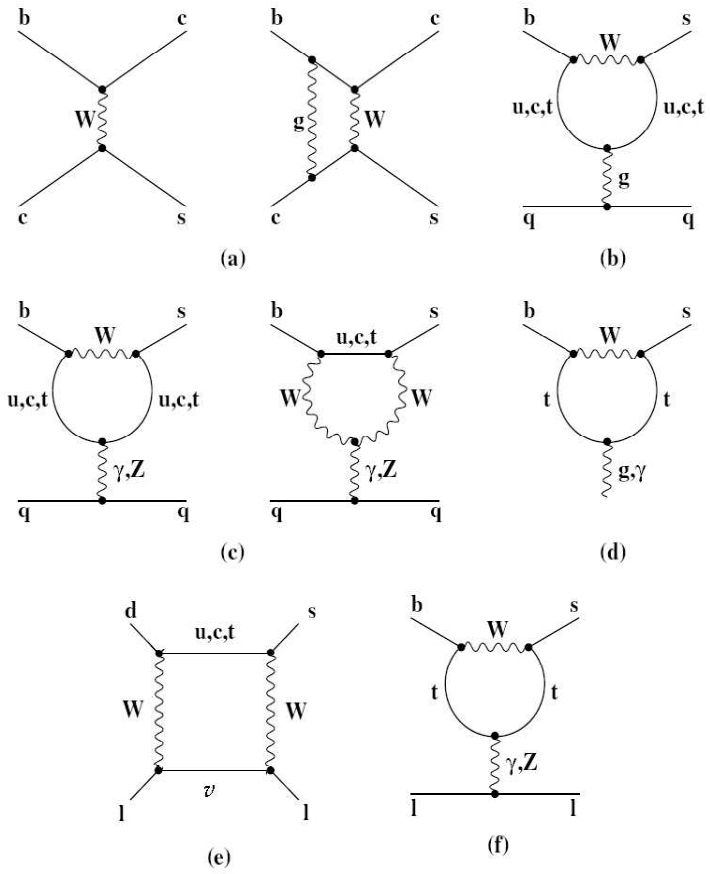

Figure 1.3: *Typical diagrams in the full theory from which the operators (1.4.6)–(1.4.14) originate.*

denote the electromagnetic and chromomagnetic field strength tensor, respectively. As can be seen from the operator basis, only degrees of freedom which are light compared to the heavy integrated out fields (W, t, ϕ), remain in the theory. All operators have dimension 6.

OPE series is equivalent to the full theory when all orders in $1/M_W^2$ are considered. The truncation of the operator series gives a systematic approximation scheme for low-energy processes.

1.5 Short-Distance Contributions

The coupling strength of the introduced effective vertexes O_i is given by the (C-numbers) Wilson coefficients $C_i(\mu)$. Their values are calculated perturbatively from a "matching" of the effective with the full theory. This calculation is performed at the high scale $\mu \sim m_W$ where the coefficients can be worked out in fixed order perturbation theory:

$$C_i(\mu) = C_i^{(0)}(\mu) + \frac{\alpha_s^2}{16\pi^2} C_i^{(1)}(\mu) + \frac{\alpha_s^4}{(16\pi^2)^2} C_i^{(2)}(\mu) + O(\alpha_s^6) \qquad (1.5.1)$$

Since the Wilson coefficients comprises only physics of the high scale, they do not depend on external momenta and small masses. The matching procedure can thus be done in a momentum configuration which simplifies the calculation as much as possible. The RGE ([10],[14]) must be solved in order to evolute the Wilson coefficients from the high scale $\mu \sim m_W$ to the low scale $\mu \sim m_b$ for a B-hadron decay.

The dependence on external momentum is fully contained in the matrix elements of the local operators Q_i between initial and final states. Because low-energy contributions are separates into the matrix elements, these cannot be calculated in perturbation theory for transition between physical meson states. For the extraction of Wilson coefficients, the OPE have to be calculated for unphysical off-shell quarks external states. It is irrelevant that an unphysical amplitude is considered, since the coefficients do not depend on the external states, but rather represent the short-distance structure of the theory. To extract interesting decay amplitudes for physical processes, once one has extracted the coefficient and written down the effective Hamiltonian, some non-perturbative approach have to be utilized for evaluating the matrix elements of local operator.

In more complex case, involving penguin and box diagrams, the Wilson coefficient C_i include the top quark contributions and contributions from other heavy particles such as W and Z bosons and charged Higgs particles or supersymmetric particles in the supersymmetric extension of the SM. An important feature of the OPE is the universality of the Wilson coefficients. They are independent of the external state and therefore they can be view as effective coupling constants and the local operators as the corresponding interaction vertexes.

1.6 Long Distance Contributions

In this section a brief introduction to the method employed for the calculation of the hadronic matrix elements of Q_i operators is given, in particular for meson decays.

The calculation encounters the problem of describing the hadron structure and requires a non-perturbative consideration. To this end various theoretical methods have been adopted ([16]), like: quark models, QCD sum rules and lattice calculation.

QCD sum rules are suitable for describing the low squared momentum transfer q^2 region: the higher q^2 region is hard to get and higher order calculation are not likely to give good results because the appearance of many new parameters in the description of the matrix elements. Lattice QCD simulations, because their most direct connection with QCD, are expected to provide

the most reliable results. The present limitation is that lattice calculations do not yet provide the hadronic matrix elements in the whole accessible kinematic range but only in the large squared momentum transfer region, complementary to sum rules calculations. The quark models have probed to be a fruitful phenomenological method to the description of heavy meson transitions in the full range of squared momentum transfer. However, quark models are not closely related to the QCD Lagrangian and therefore have input parameters which are not directly measurable and may not be of fundamental significance.

A short description of the QCD sum rules approach is presented because their importance for the $b \to s$ transitions discussed later in this chapter.

1.6.1 Hadronic Matrix Elements in Weak Meson Decays

The effective amplitude for a decay of an heavy hadron H into a final state f reads as

$$A_{\text{eff}} \sim \sum_i C_i(\mu)\langle f|Q_i(\mu)|H\rangle. \tag{1.6.1}$$

For a weak exclusive decay of an heavy hadrons such a B-meson, any extraction of the perturbative short-distance effects encoded in the Wilson coefficient of the effective amplitude (1.6.1), requires an accurate separation of the non-perturbative long-distance contributions. The long distance contributions contain informations about the dynamics of the decay and they allow the extraction of the parameters of the SM such as the V_{CKM} matrix elements via the comparison with the experimental data. The theoretical investigation of these contributions encounters the problem of describing the hadron structure, which provides the main uncertainly in the prediction of decays.

Calculations of weak decays of mesons require determination of matrix elements of various transition currents between initial and final meson states. The most general transition between two meson states is shown in Figure 1.4.

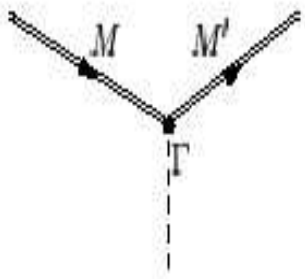

Figure 1.4: *Diagrammatic representation of a transition current* Γ *between initial* (M) *and final* (M') *meson states.*

The interest is turned to the decays of heavy pseudoscalar mesons involving transitions between a heavy quark Q and a light quark q. In general these matrix elements can be written as

$$\langle P'(M',p')|\bar{q}\Gamma Q|P(M,p)\rangle \tag{1.6.2}$$

for decays to pseudoscalar mesons, and

$$\langle V(M',p',\varepsilon^*)|\bar{q}\Gamma Q|P(M,p)\rangle \tag{1.6.3}$$

for decays to vector mesons. $P(M,p)$ is the initial pseudoscalar meson with momentum p and mass M, and $P'(M',p')$ and $V(M',p',\varepsilon^*)$ are the final pseudoscalar and vector mesons with momentum p', mass M' and helicity ε^*. Here Γ describes the Lorentz structure of the current and can be any of the following: γ^μ and $\gamma^\mu\gamma^5$ for the familiar vector and axial currents from the standard electroweak model, and also $\sigma^{\mu\nu}$ and $\sigma^{\mu\nu}\gamma^5$ for the tensor currents, which can arise due to magnetic interactions of hadrons. The form of the matrix elements can then be constructed from sums and products of the two momenta p and p' and a few form factors, scalar functions of Lorentz invariants, such as the squared momentum transfer $q^2=(p-p')^2$, by employing Lorentz symmetry principles. The relativistic invariant form factors contain informations on the dynamics and on the non-perturbative aspects of the decay processes, so that they should be calculated within a non-perturbative approach for any particular initial and final meson states.

1.6.2 QCD Sum Rules Approach

QCD Sum Rules (QRS) ([16]) are based on the following theoretical ideas:

- structure of the QCD vacuum and OPE;
- quark-hadron duality.

The basic investigated quantities in the QSR are the two points correlation functions defined at the Euclidean momentum $Q^2=-q^2$:

$$\Pi(Q^2)=i\int d^4x e^{iq\cdot x}\langle vac|T\left(J(x)J(0)^\dagger\right)|vac\rangle \tag{1.6.4}$$

where $|vac\rangle$ represents the QCD non-perturbative vacuum. The local currents J are made of quarks and gluon fields and have the same quantum numbers of the hadrons one is interested. The (1.6.4) represents the Fourier transform of the non-perturbative propagation amplitude of hadrons from 0 to x. The connection of $\Pi(Q^2)$ to the relevant hadrons is realized by a dispersive representation

$$\Pi(Q^2)=\frac{1}{\pi}\int_{threshold}^{\infty} ds\frac{\rho(s)}{s+Q^2} \tag{1.6.5}$$

where the spectral function $\rho(s) = Im\Pi(s)$ contains informations on the physical hadronic states whit the quantum numbers of J. The left side of (1.6.4) can be evaluated in QCD at large $Q^2 >> \Lambda^2_{QCD}$ by means of the OPE which organizes the result in terms of a sum of products of the short-distance perturbative coefficient times coefficients that are a set of non perturbative quark and gluon operator vacuum matrix elements divided by the inverse powers of Q^2 corresponding to the dimension of the matrix elements:

$$\Pi(Q^2)_{QCD} = \sum_n C_k(Q^2, \alpha_s, \mu) \frac{\langle vac|O_n(\mu)|vac\rangle}{(Q^2)^n} \tag{1.6.6}$$

where C_n are Wilson coefficient. The vacuum matrix elements (condensates) account for the effects on the non perturbative QCD vacuum. Knowledge of the vacuum condensates up to some dimension allows the extrapolation in Q^2 from the asymptotic freedom region down to moderate Q^2 close to the hadronic mass scales.

QSR are obtained by imposing, according to the quark-hadron duality, the requirement that the two description (1.6.5) and (1.6.6) match in a wide range of Q^2. In this way, hadronic properties (masses, coupling constants, *etc.*) can be related to QCD parameters (quark masses, α_s, vacuum condensates). The vacuum condensates $\langle vac|O_n(\mu)|vac\rangle = d_n \neq 0$ must be estimated in some non-perturbative frameworks or inferred from applications of QCD sum rules to cases where the hadronic spectral density $\rho(s)$ is well known. The values of the condensates so determined can be used to make predictions in other channels of interest.

To extend the method of QSR to the calculation of the hadronic form factors, the basic objects to study are three-point correlators of the kind:

$$\Pi(p, p', q)_\mu = i^2 \int d^4x d^4y e^{i(p'\cdot x - p\cdot y)} \langle vac|T\left(J_2(x) J^{V,A}_\mu(0) J_1(y)\right)|vac\rangle \tag{1.6.7}$$

where $q = p - p'$, the currents J_1 and J_2 interpolate the hadrons, and $J^{V,A}_\mu$ are weak currents. The connection of (1.6.7) to hadronic data is obtained through spectral representations involving double spectral functions $\rho(s, s', q^2)$ containing the required form factor $F(q^2)$. The left side of (1.6.7) can be expressed as an OPE in the framework of QCD, accounting for the asymptotic freedom contribution plus non-perturbative vacuum condensates. QCD Sum Rules are obtained by matching these alternatives representations.

Light Cone-QCD Sum Rule

Another possibility to study form factors is represented by the light-cone QCD sum rule approach ($LCSR$) ([19]).
Instead of the current correlator in (1.6.7), correlators with one of the hadrons as an external state are analyzed:

$$\Pi(p,p',q)_\mu = i\int d^4x e^{ip'\cdot x}\langle vac|T\left(J_2(x)J_\mu^{V,A}(0)\right)|H_1(p)\rangle. \tag{1.6.8}$$

With $P^2 = M_{H_1}^2$ fixed, a dispersion relation in the variable p'^2 at fixed q^2 is assumed to hold for (1.6.8), as usual parametrized in terms of the required form factor. The OPE is applied to the T-product on the right side of (1.6.8) and involve in this case contributions to the light-cone wave function of the H_1 hadrons. The wave functions can be modeled in the case of some light hadrons such as pions and kaons and this kind of QSR has some advantages for heavy to light decay form factors.

1.7 Rare $B \to K^{(*)}l^+l^-$ Decays in SM

An effective $|\Delta B| = 1$ Hamiltonian triggering the decay of the B-meson in analysis can be written as

$$\mathcal{H}_{\text{eff}} = -\frac{G_F}{\sqrt{2}}V_{tb}V_{ts}^*\sum_{i=1}^{10}C_i(\mu)Q_i(\mu) \tag{1.7.1}$$

where the local operators are listed in (1.4.6)-(1.4.14).

The $b \to sl^+l^-$ receives dominant contributions from Q_7, Q_9 and Q_{10} operators. In Figure 1.5, the diagrams originate from these operator are showed.

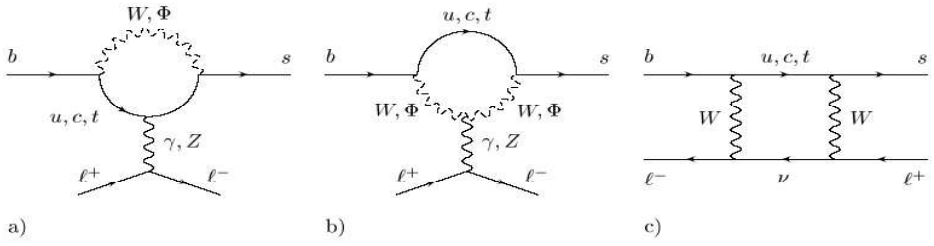

Figure 1.5: *SM Feynman diagrams for the $b \to sll$ transition: a), b) photonic and Z^0 penguin, c) box diagram.*

The Hamiltonian in (1.7.1) leads to the following free quark decay amplitude:

$$\begin{aligned}\mathcal{M}(b\to s\ell^+\ell^-) &= \frac{G_F\alpha}{\sqrt{2}\pi}V_{ts}^*V_{tb}\left\{C_9^{\text{eff}}\left[\bar{s}\gamma_\mu Lb\right]\left[\bar{\ell}\gamma^\mu\ell\right] + C_{10}\left[\bar{s}\gamma_\mu Lb\right]\left[\bar{\ell}\gamma^\mu\gamma_5\ell\right]\right.\\ &\left. -2\hat{m}_bC_7^{\text{eff}}\left[\bar{s}i\sigma_{\mu\nu}\frac{\hat{q}^\nu}{\hat{s}}Rb\right]\left[\bar{\ell}\gamma^\mu\ell\right]\right\}. \end{aligned}\tag{1.7.2}$$

Here, $L/R \equiv (1 \mp \gamma_5)/2$, $s = q^2$, $q = p_+ + p_-$ where $p_\pm$ are the four-momenta of the leptons, respectively. In the following, the hat denotes normalization in terms of the B-meson mass, m_B, e.g. $\hat{s} = s/m_B^2$, $\hat{m}_b = m_b/m_B$. The (1.7.2), although a free quark decay amplitude, contains long-distance effects from the matrix elements of four-quark operators (Current-Current and QCD-Penguins operators), $\langle \ell^+\ell^- s|\mathcal{O}_i|b\rangle$, $1 \leq i \leq 6$, to take into account the contribution coming from the $c\bar{c}$ resonance decaying in two leptons. These long-distance contributions usually are absorbed into a redefinition of the short-distance effective Wilson Coefficients. The expressions for effective Wilson Coefficients are too complicated to present here. Their expressions can be found in [20], [21]. For the short-distance contributions the $NNLO$ corrections calculated in [22] and [23] have been used and here reported in Table 1.1.

C_7^{eff}	C_9^{eff}	C_{10}
-0.313	4.344	-4.669

Table 1.1: *C_7^{eff}, C_9^{eff} and C_{10} Wilson coefficients from [22] and [23].*

Exclusive decays $B \to K^{(*)}\ell^+\ell^-$ are described in terms of matrix elements of the quark operators in Eq. (1.7.2) over meson states, which can be parametrized in terms of form factors.

The matrix elements of the transition involving the pseudoscalar mesons $B \to K$ for the non-vanishing matrix elements, parametrized in terms of form factors, are ($q = p_B - p$):

$$\langle K(p)|\bar{s}\gamma_\mu b|B(p_B)\rangle = f_+(s)\left\{(p_B+p)_\mu - \frac{m_B^2 - m_K^2}{s}\,q_\mu\right\} + \frac{m_B^2 - m_K^2}{s}\,f_0(s)\,q_\mu \tag{1.7.3}$$

and

$$\begin{aligned}\langle K(p)|\bar{s}\sigma_{\mu\nu}q^\nu(1+\gamma_5)b|B(p_B)\rangle &\equiv \langle K(p)|\bar{s}\sigma_{\mu\nu}q^\nu b|B(p_B)\rangle \\ &= i\left\{(p_B+p)_\mu s - q_\mu(m_B^2 - m_K^2)\right\} \\ &\quad \times\frac{f_T(s)}{m_B + m_K}.\end{aligned} \tag{1.7.4}$$

For the vector meson K^* with polarization vector ϵ_μ, the semileptonic form factors of the $V - A$ current is defined by

$$\begin{aligned}\langle K^*(p)|(V-A)_\mu|B(p_B)\rangle &= -i\epsilon_\mu^*(m_B + m_{K^*})A_1(s) + \\ &\quad i(p_B+p)_\mu(\epsilon^* p_B)\,\frac{A_2(s)}{m_B + m_{K^*}} + \\ &\quad iq_\mu(\epsilon^* p_B)\,\frac{2m_{K^*}}{s}\,(A_3(s) - A_0(s)) + \\ &\quad \epsilon_{\mu\nu\rho\sigma}\epsilon^{*\nu}p_B^\rho p^\sigma\,\frac{2V(s)}{m_B + m_{K^*}}\,.\end{aligned} \tag{1.7.5}$$

Note the exact relations

$$\begin{aligned} A_3(s) &= \frac{m_B + m_{K^*}}{2m_{K^*}} A_1(s) - \frac{m_B - m_{K^*}}{2m_{K^*}} A_2(s), \\ A_0(0) &= A_3(0), \\ \langle K^* | \partial_\mu A^\mu | B \rangle &= 2m_{K^*} (\epsilon^* p_B) A_0(s). \end{aligned} \tag{1.7.6}$$

The decay $B \to K^* \ell^+ \ell^-$ is described by the above semileptonic form factors and the following penguin form factors:

$$\begin{aligned} \langle K^* | \bar{s} \sigma_{\mu\nu} q^\nu (1+\gamma_5) b | B(p_B) \rangle &= i\epsilon_{\mu\nu\rho\sigma} \epsilon^{*\nu} p_B^\rho p^\sigma \, 2T_1(s) \\ &\quad + T_2(s) \left\{ \epsilon_\mu^* (m_B^2 - m_{K^*}^2) - (\epsilon^* p_B) (p_B + p)_\mu \right\} \\ &\quad + T_3(s) (\epsilon^* p_B) \cdot \\ &\quad \times \left\{ q_\mu - \frac{s}{m_B^2 - m_{K^*}^2} (p_B + p)_\mu \right\} \end{aligned} \tag{1.7.7}$$

with

$$T_1(0) = T_2(0). \tag{1.7.8}$$

All signs are defined in such a way as to have positive form factors. The physical range in s extends from $s_{\min} = 2m_l$ to $s_{\max} = (m_B - m_{K,K^*})^2$.

The above form factors are calculated by the QCD sum rules on the light-cone. A complete review of such calculation can be found in [21].

1.7.1 Branching Ratios

With the Wilson coefficients calculated at the $NNLO$ and form factors evaluated in QCD $LCSR$ approach, the Standard Model predictions for the exclusive branching ratios are reported in Table 1.2. A more complete review can be found in [21] and [1].

Mode	$\mathcal{B}$ (10^{-6})
$B \to K l^+ l^-$	0.35 ± 0.12
$B \to K^* e^+ e^-$	1.58 ± 0.49
$B \to K^* \mu^+ \mu^-$	1.19 ± 0.39

Table 1.2: *Standard Model prediction for the branching ratio following approach in [1].*

The dominant source of uncertainty comes from the form factor dependence.

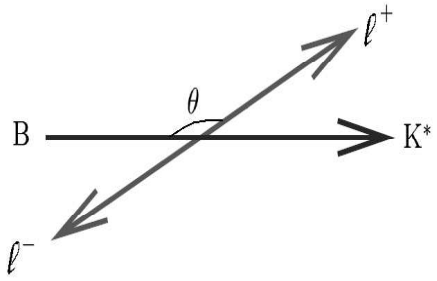

Figure 1.6: *Angle θ between the positive charge lepton and the B in the dilepton rest frame.*

1.7.2 Forward-Backward Asymmetry Distribution

Of particular interest is the differential forward-backward charge asymmetry. This asymmetry is defined as

$$\frac{\mathrm{d}\mathcal{A}_{\mathrm{FB}}}{\mathrm{d}\hat{s}} = -\int_0^{\hat{u}(\hat{s})} \mathrm{d}\hat{u}\frac{\mathrm{d}^2\Gamma}{\mathrm{d}\hat{u}\mathrm{d}\hat{s}} + \int_{-\hat{u}(\hat{s})}^0 \mathrm{d}\hat{u}\frac{\mathrm{d}^2\Gamma}{\mathrm{d}\hat{u}\mathrm{d}\hat{s}} \,. \tag{1.7.9}$$

with

$$\hat{u}(\hat{s}) = \sqrt{\lambda(1-4\frac{\hat{m}_\ell^2}{\hat{s}})} \,, \tag{1.7.10}$$

$$\lambda \equiv \lambda(1,\hat{m}_{K,K*}^2,\hat{s}) = 1+\hat{m}_{K,K*}^4+\hat{s}^2-2\hat{s}-2\hat{m}_{K,K*}^2(1+\hat{s}) \,. \tag{1.7.11}$$

Note that the variable $\hat{u}$ corresponds to θ, the angle between the momentum of the B-meson and the positively charged lepton ℓ^+ in the dilepton CMS frame, through the relation $\hat{u} = -\hat{u}(\hat{s})\cos\theta$. This angle is shown in Figure 1.6.

The theoretical expressions for the FBA can be found in [21]. The FBA vanishes in SM for $B \to K\ell^+\ell^-$ decays. For the $B \to K^*\ell^+\ell^-$ decay the FBA does not vanish. The FBA distribution as a function of the dilepton squared mass is shown in Figure 1.7 for $B \to K^*\mu^+\mu^-$ decay; ψ resonances are not shown.

1.8 Rare $B \to K^{(*)}l^+l^-$ Decays in Supersymmetric Models

Investigation of rare B-meson decays opens the possibility to probe at comparatively low energies, the structure of the electroweak theory at large scale, thanks to the contributions of virtual particles in the loops. Moreover, rare $b \to s$ transitions are expected to be sensitive to new interactions, such as those provided, e.g., by supersymmetric theories, two Higgs doublet, top-color

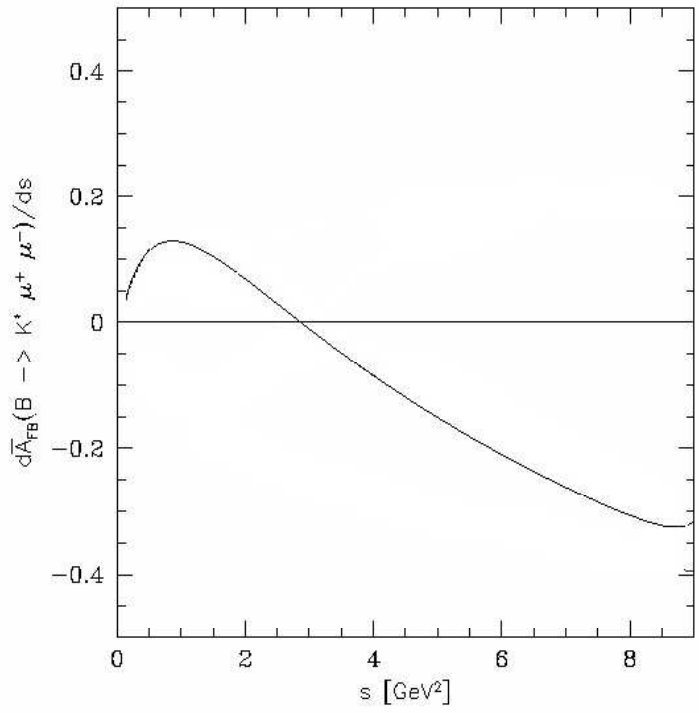

Figure 1.7: *The forward-backward asymmetry in* $B \to K^* \mu^+ \mu^-$ *decay ([21]).*

and left-right models. These interactions govern the structure of the operators and the corresponding Wilson coefficients which appear in the $\Delta B = 1$ effective electroweak Hamiltonian describing the $b \to s$ transitions. In many extensions of the Standard Model, loop graphs with new particles (such as charged Higgses or supersymmetric partners) contribute at the same order as the SM contribution, resulting in an enhancement of branching ratio, differential dilepton invariant mass and different prediction for forward-backward asymmetry. Precision measurements of these rare processes provide thus a complementary probe of New Physics to direct collider searches.

In this section a brief review of the most interesting New Physics model predictions about differential distributions of rare B-mesons decays is done.

Changes from New Physics in the values of the relevant Wilson coefficients can be taken into account by the (correlated) ratios, $(i = 7, 9, 10)$:

$$R_i(\mu) \equiv \frac{\mathcal{C}_i^{NP} + \mathcal{C}_i^{SM}}{\mathcal{C}_i^{SM}} = \frac{\mathcal{C}_i}{\mathcal{C}_i^{SM}} \ . \tag{1.8.1}$$

In $SUGRA$ model ([24]) the parameter space may be decomposed into two different regions characterized by $tan\beta$ values. For small $\tan\beta \sim 2$ the sign of C_7^{eff} is the same as in the SM. Here no signiticative deviations from the SM can be expected in the decay $B \to (K, K^*) l^+ l^-$. For large $\tan\beta$ the situation

is more interesting. Using

$$R_7 = -1.2, \quad R_9 = 1.03, \quad R_{10} = 1.0 \tag{1.8.2}$$

obtained for $\tan\beta = 30$ ([21]), an enhance by about 30% compared to the SM has been found in the low dimuon invariant mass region for the branching ratio distribution for $B \to K\mu^+\mu^-$, as shown in Figure 1.8.

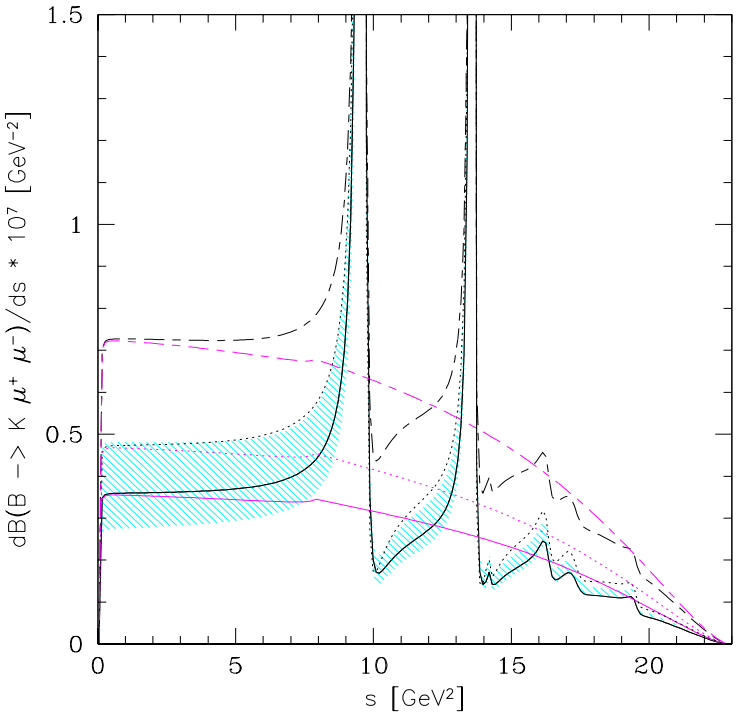

Figure 1.8: *The dilepton invariant mass distribution in $B \to K\mu^+\mu^-$ decays, using the form factors from LCSR as a function of dimuon invariant mass s. The solid line represents the SM and the shaded area depicts the form factor-related uncertainties. The dotted line corresponds to the SUGRA model with $R_7 = -1.2$, $R_9 = 1.03$ and $R_{10} = 1$. The long-short dashed lines correspond to an allowed point in the parameter space of the MIA-SUSY model, given by $R_7 = -0.83$, $R_9 = 0.92$ and $R_{10} = 1.61$. The corresponding pure SD spectra are shown in the lower part of the plot.*

This enhancement is difficult to disentangle from the non-perturbative uncertainties attendant with the SM distributions (shaded band in the figure).

The dilepton mass distribution for $B \to K^*\mu^+\mu^-$ is more promising, as in this case the enhancement is around the 100% as shown in Figure 1.9.

Also in forward-backward asymmetry distribution some significative variation with respect to the SM predictions are expected as shown in Figure 1.10 for $SUGRA$ model prediction at large $\tan\beta$.

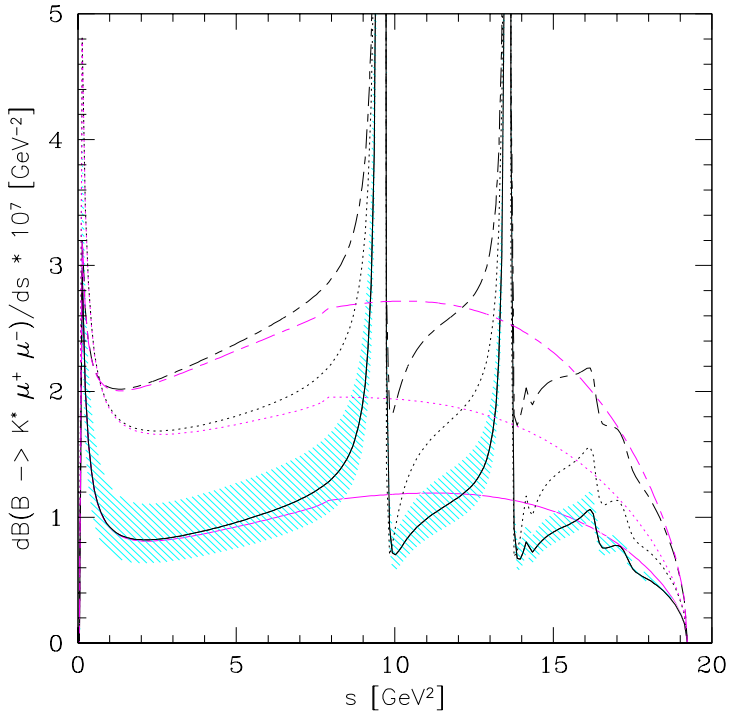

Figure 1.9: *The dilepton invariant mass distribution in $B \to K^* \mu^+ \mu^-$ decays, using the form factors from LCSR as a function of s. The legends are the same as in Figure 1.8.*

Figures 1.8, 1.9 and 1.10 shown also the MIA (Minimal Insertion Approximation) ([25]) model calculations. They have been obtained for the following values

$$R_7 = \pm 0.83, \quad R_9 = 0.92, \quad R_{10} = 1.61 \tag{1.8.3}$$

The characteristic difference in this case, as compared to the $SUGRA$ model, lies the significantly enhanced value of C_{10}. The sign of C_{10} (also in $SUGRA$ model) is opposite with respect to the SM calculation. This has no effect on the dilepton invariant mass distributions, as they depend quadratically on C_{10}, but it changes the sign of forward backward asymmetry in $B \to K^* l^+ l^-$. To illustrate this, the parameters of the so-called "best depression" scenario have been used corresponding to the following values ([21]):

$$R_7 = \pm 0.83, \quad R_9 = 0.79, \quad R_{10} = -0.38 \ , \tag{1.8.4}$$

and the normalized forward-backward asymmetry is shown in Figure 1.10.

The dilepton invariant mass spectrum and the forward-backward asymmetry for $B \to (K, K^*) l^+ l^-$ processes have been analyzed under supersymmetric context also in [26]. Special attention has been payed to the effects of the

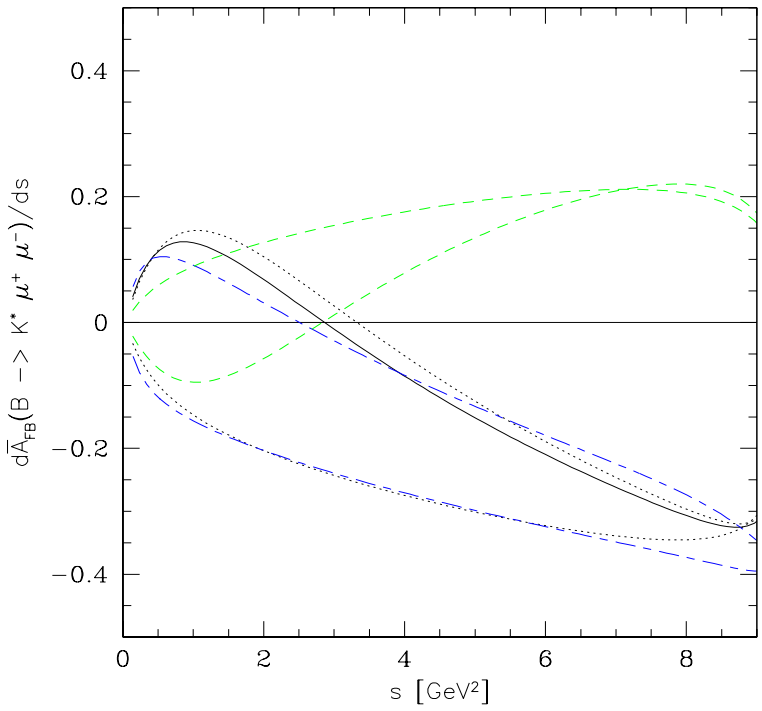

Figure 1.10: *The normalized forward-backward asymmetry in* $B \to K^*\mu^+\mu^-$ *decay as a function of* s*, using the form factors from the LCSR approach. The solid line denotes the SM prediction. The dotted (long-short dashed) lines correspond to the SUGRA (the MIA-SUSY) model, using the parameters given in Eq. (1.8.2) (Eq. (1.8.3)) with the upper and lower curves representing the* $C_7^{\text{eff}} < 0$ *and* $C_7^{\text{eff}} > 0$ *case, respectively. The dashed curves indicating a positive asymmetry for large* s *correspond to the MIA-SUSY models using the parameters given in Eq. (1.8.4), i.e. the "best depression scenario" with* $C_{10} > 0$*.*

Neutral Higgs Bosons ($NHBs$). The analysis shows that the branching ratio of the process $B \to K\mu^+\mu^-$ can be quite largely modified by the effects of Neutral Higgs Bosons and the forward-backward asymmetry would not vanish as in the SM, as shown in Figure 1.11. For the process $B \to K^*\mu^+\mu^-$, the dilepton invariant mass spectrum and the forward-backward asymmetry are not sensitive to the effect of the $NHBs$.

Wilson coefficient calculations in the context of the two Higgs doublet model ($2HDM$) and supersymmetry ($SUSY$) with minimal flavour violation, focusing on the case of large $\tan\beta$ can be found in [27]. Differential decay spectrum of $B \to Kl^+l^-$ together with the corresponding forward-backward asymmetry have been studied. Scalar and pseudoscalar new interactions can lead to effects in the decay distribution but these effects are much smaller. In view of the uncertainty of the predictions for exclusive B-decays due to

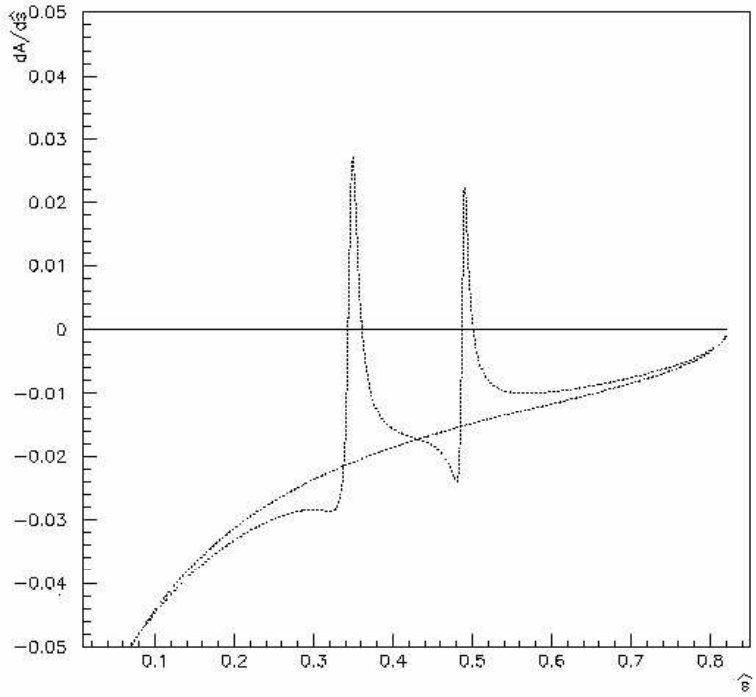

Figure 1.11: *The forward-backward asymmetry in* $B \to K\mu^+\mu^-$ *decay. The dotted line corresponds to calculation in the region with large* $\tan\beta$ *and masses of superpartners relatively small. Both the total (SD+LD) and the pure SD contributions are shown in order to compare*

the form factors, it seems extremely unlikely that a measurement of the decay spectrum alone can provide a clue to New Physics. But the observation of a nominal forward-backward asymmetry of 4% will might be feasible at the *LHC*.

1.9 Experimental Results from B-factories

In this section a review of the experimental results for $B \to K^{(*)}l^+l^-$ decays from Belle ([28],[29]) and Babar([30]) collaborations is done.

The more updated values of branching ratios for B-meson rare decays come from BaBar collaboration. The lepton-flavour averaged and B-charge averaged branching fractions are:

$$\mathcal{B}(B \to Kl^+l^-) = (0.34 \pm 0.07 \pm 0.02) \times 10^{-6},$$
$$\mathcal{B}(B \to K^*l^+l^-) = (0.78^{+0.19}_{-0.17} \pm 0.11) \times 10^{-6},$$

where the first error is statistical and the second is systematic. The results for the individual decay modes are shown in Table 1.3. The inclusive branching

ratios are in agreement with calculations reported in Table 1.2 ([1]) and consistent with Standard Model predictions. For exclusive decays, the statistical uncertainty is yet very high and more precise measurements are needed.

Mode	$\mathcal{B}$ (10^{-6})
$K^+e^+e^-$	$0.42^{+0.12}_{-0.11} \pm 0.02$
$K^+\mu^+\mu^-$	$0.31^{+0.15}_{-0.12} \pm 0.03$
$K^0e^+e^-$	$0.13^{+0.16}_{-0.11} \pm 0.02$
$K^0\mu^+\mu^-$	$0.59^{+0.33}_{-0.26} \pm 0.07$
$K^{0*}e^+e^-$	$1.04^{+0.33}_{-0.29} \pm 0.11$
$K^{0*}\mu^+\mu^-$	$0.87^{+0.38}_{-0.33} \pm 0.12$
$K^{*+}e^+e^-$	$0.75^{+0.76}_{-0.65} \pm 0.38$
$K^{*+}\mu^+\mu^-$	$0.97^{+0.94}_{-0.69} \pm 0.14$

Table 1.3: *BaBar results for the individual $K^{(*)}l^+l^-$ decay modes for the whole dimuon invariant mass range. The columns from left are: decay mode and the resulting branching fraction (with statistical and systematic errors).*

Babar collaboration also measured differential decay distributions. Figure 1.12 shows the branching ratio in bins of dilepton invariant mass $q^2 \equiv s$ for (a) $B \to Kl^+l^-$ and (b) $B \to K^*l^+l^-$ normalized to the total measured branching fraction. The results are generally consistent with the q^2 dependence predicted in Standard Model based form factor calculations. Forward-backward asymmetry measurements for $B \to K^*l^+l^-$ modes is shown in Figure 1.13. A large positive asymmetry in the high q^2 region, consistent with the SM expectations has been found. This disfavors New Physics scenarios in which the product of the C_9^{eff} and C_{10}^{eff} Wilson coefficients have the same magnitude but opposite relative sign as in the SM, which would result in a large negative asymmetry at high q^2. At low q^2 a positive value of A_{FB} is also favored, with a 95% CL lower limit that is slightly above the SM prediction and it do not seem to exclude New Physics contribution.

Figure 1.14 shows the Belle collaboration results for forward-backward asymmetry measurements for $B \to K^*l^+l^-$ decay. The Belle measurement are consistent with the BaBar ones in the high q^2 region. In the low q^2 area Belle measurement seems to exclude the New Physics scenarios shown by the dot-dashed and the dotted curves.

For $B \to Kl^+l^-$ decay, Figures 1.15 and 1.9 show the Belle Collaboration measurements for dimuon invariant mass spectrum and forward-backward asymmetry. The q^2 distribution seems to be in agreement with SM predictions, while the statistical errors on FBA distribution do not allow to draw significative conclusions.

More precise measurements are needed for differential distributions of rare semileptonic B-decays in order to discriminate between SM and New Physics

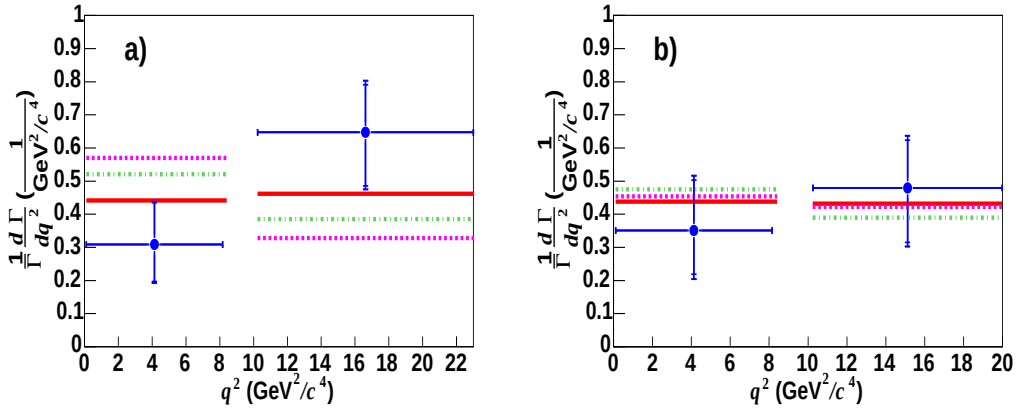

Figure 1.12: *BaBar: partial branching fractions in bins of q^2 for (a) $B \to Kl^+l^-$ and (b) $B \to K^*l^+l^-$, normalized to the total measured branching fraction. The points with error bars are data, the lines represent the central values of Standard Model predictions based on the form factor models QCD LCSR (solid lines), Relativistic Quark Model (dashed lines), and QDCSR (dot-dashed lines).*

predictions, to improve the knowledge of the CKM matrix elements and to study loop effects.

ATLAS can give and important contribution to rare semileptonic beauty decays measurements as demonstrated in [34]. The interest in the rare short-distance $FCNC$ contribution to the $B \to l^+l^-K$ decays demands that the mass of the dilepton system should not be compatible with the mass of any hadronic source of dileptons, in particular the J/ψ and the $\psi(2S)$. This out of resonance requirements call for a good mass resolution and thus a good momentum resolution of the two leptons. This cannot be fulfilled with electrons as the energy loss due to Bremsstrahlung is too high. Consequently only dimuon decays have been taken into account.

A major issue of this PhD thesis is the preparation of the strategy and software machinery for next physics analysis of rare B-decays in ATLAS, through simulation studies of $B^+ \to K^+\mu^+\mu^-$ and $B^+ \to K^{*+}\mu^+\mu^-$ decay channels, together with the signal characterization, the background rejection strategy and estimation of event yields and ATLAS sensitivity on physical observables.

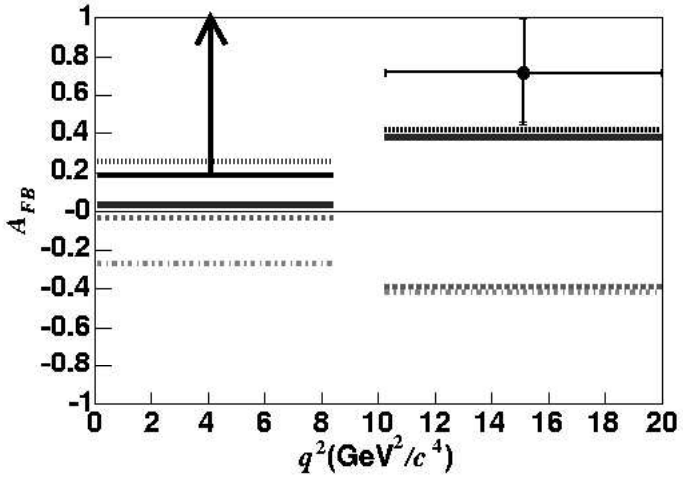

Figure 1.13: *BaBar:* $A_{FB}(q^2)$ *in* $B \to K^* l^+ l^-$. *The points with error bars are data, with the arrow at low* q^2 *in* A_{FB} *indicating the* 95% *CL allowed region. The lines represent the predictions of the SM (solid lines),* $C_7^{\rm eff} = -C_7(SM)$ *(dotted lines),* $C_9^{\rm eff} C_{10}^{\rm eff} = -C_9 C_{10}(SM)$ *(dashed lines), and* $C_7^{\rm eff}, C_9^{\rm eff} C_{10}^{\rm eff} = -C_7(SM), -C_9 C_{10}(SM)$ *(dot-dashed lines) with the form factor model in LCSR approach.*

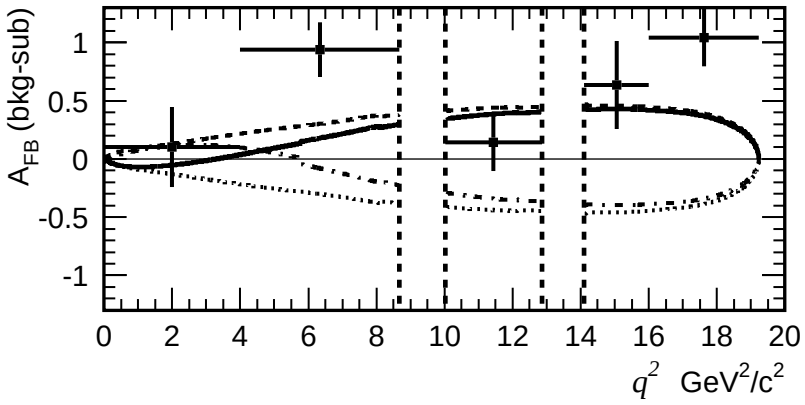

Figure 1.14: *Belle: fit result for the negative* C_7 *solution (solid) projected onto the background subtracted forward-backward asymmetry, and forward-backward asymmetry curves for several input parameters, including the effects of efficiency;* C_7 *positive case (dashed),* C_{10} *positive case (dot-dashed) and both* C_7 *and* C_{10} *positive case (dotted). The pairs of dashed lines are the boundaries of the* J/ψ *and* ψ' *veto regions.*

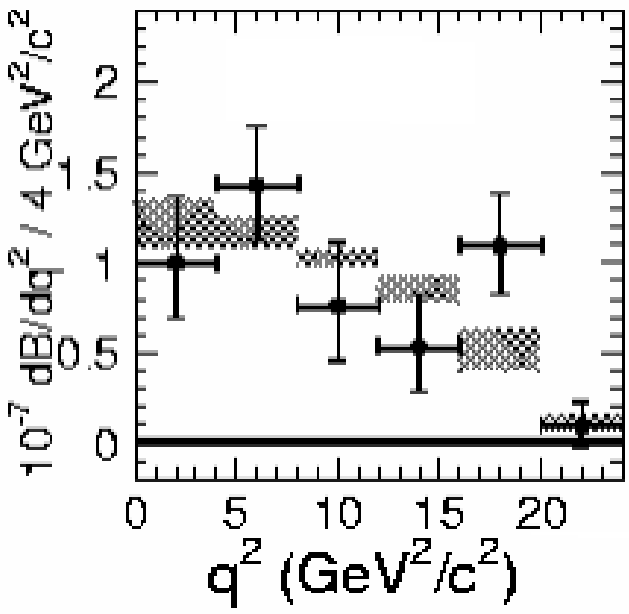

Figure 1.15: *Belle: the q^2 distribution of $B \to Kl^+l^-$. Points with error bars show the data, while the hatched bands show the range of the SM predictions.*

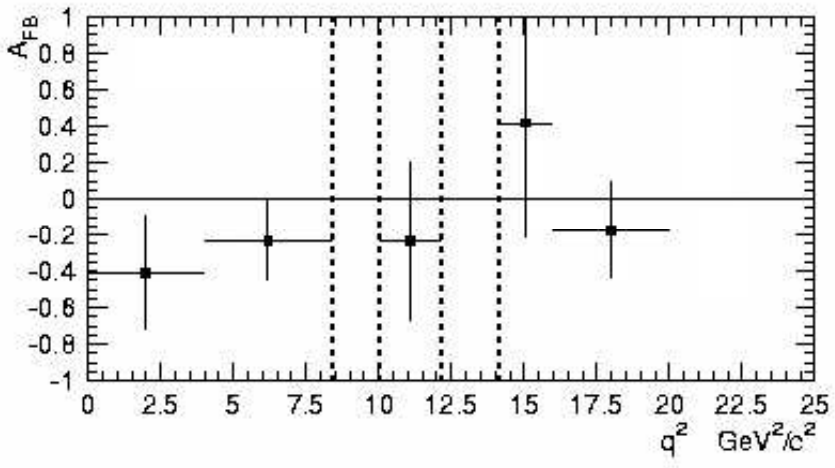

Figure 1.16: *Belle: the forward-backward asymmetry in $B \to Kl^+l^-$. Points with error bars show the data. The asymmetry vanishes in SM prediction. The pairs of dashed lines are the boundaries of the J/ψ and ψ' veto regions.*

Chapter 2

Atlas Experiment at LHC

2.1 The Large Hadron Collider (LHC)

The **L**arge **H**adron **C**ollider (LHC) is a proton-proton collider that will run at 14 TeV of center of mass energy ($\sqrt{s} = 14\ TeV$). This energy is not the real energy involved in the interaction, because of the proton structure. The effective energy is scaled down by the proton momentum fraction carried by the two colliding partons ($\sqrt{s'} = \sqrt{sx_a x_b}$) ([31]).

The CERN's existing accelerators (LINAC, BOOSTER, PS, SPS) will be used to accelerate protons up to 450 GeV. After the injection into the LHC, the two beams will reach the energy of 7 TeV. In addition to p-p collision, the LHC will be able to collide heavy nuclei (Pb-Pb) at the energy of $\sqrt{s}^{NN} = 5.5\ TeV$ per nucleon ([32]).

Along the 27 km there are eight linear sections (IP), each one 528 m long, and in four of these intersections there will be the following detectors:

- ATLAS, **A** **T**oroidal **L**HC **A**pparatu**S**
- CMS, **C**ompact **M**uon **S**olenoid
- ALICE, **A** **L**arge **I**on **C**ollider **E**xperiment
- LHCb, **L**arge **H**adron **C**ollider **b**physics

In Figure 2.1 is shown the LHC ring, there are the four experimental sections while the other sections contain collimation systems, RF systems and beam dump insertions.

The two proton beams will travel in separate beam pipes (separated by 194 mm) passing through oppositely directed magnetic field of 8.38 T. These fields are generated by dipole and quadrupole superconducting magnets operating at 1.9 K.

The protons will come in roughly cylindrical bunches, few centimeters long and few microns in radius. The distance between bunches is 7.5 m, in time 25 ns; they will collide in the 110 m long regions, without any magnetic field. At the high luminosity ($10^{34}\ cm^{-2}\ s^{-1}$), the two beams will be made of 2835

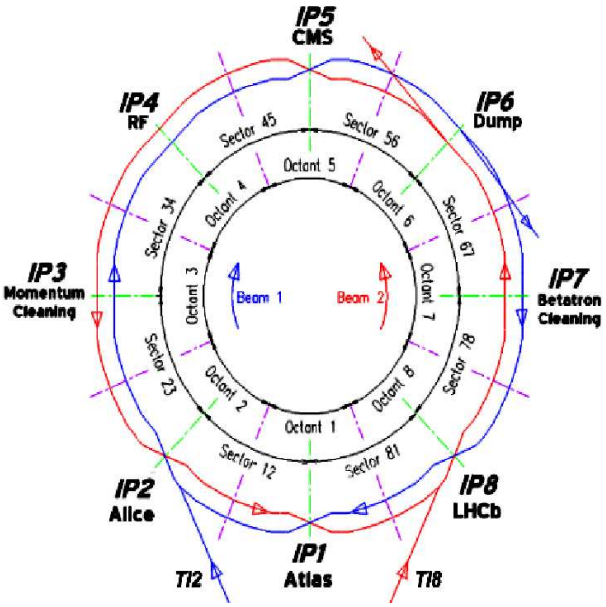

Figure 2.1: *LHC view with all the detectors installed.*

bunches. During the initial phase, LHC will run at the lower luminosity of $10^{33} cm^{-2} s^{-1}$ ([33]).

The luminosity $\mathcal{L}$ of a collider is a parameter depending on the machine that connects the interaction cross section (σ) with the number of events per second (rate, $\mathcal{R}$):

$$\mathcal{R} = \mathcal{L}\sigma_{int} \tag{2.1.1}$$

The luminosity is related to the machine parameter, through:

$$\mathcal{L} = F\frac{f n_1 n_2}{4\pi\sigma_x\sigma_y} \tag{2.1.2}$$

where f is the (particle bunch) collision frequency, n_1 and n_2 the number of particles per bunch, σ_x and σ_y are the parameters which characterize the beam profile in the orthogonal planes, respectively, and F, equal to 0.8, depends on the angle of the beams.

2.2 The ATLAS Detector

The ATLAS detector has been designed to maximize the physics discovery potential offered by the LHC accelerator. The detector design is therefore guided by physics issues among which the electroweak symmetry breaking, the search of super-symmetric particles with the possibility to study also New Physics and heavy flavour physics. To meet all these physics goals, the ATLAS detector must be able to measure the energy-momentum four-vector with great precision for all particles produced having a sufficiently long lifetime to be

detected. If possible, the particle identification should be done with high efficiency ([33]).

The goal to exploit the full physics potential of LHC leads to the following basic considerations:

- a good calorimetric system, composed by an Electromagnetic Calorimeter to identify electrons and photons, and a Hadronic Calorimeter to have accurate measurements of jets and missing energy;
- an efficient tracking system for high p_T lepton momentum measurements and full event reconstruction at low luminosity;
- an high precision muon system that guarantees accurate momentum measurements;
- a large η and ϕ coverage, where ϕ ,the azimuthal angle, is measured around the beam axis, while η the pseudorapidity, is related with the polar angle θ.

The ATLAS detector layout consists of different specialized sub-detectors, as shown in Figure 2.2.

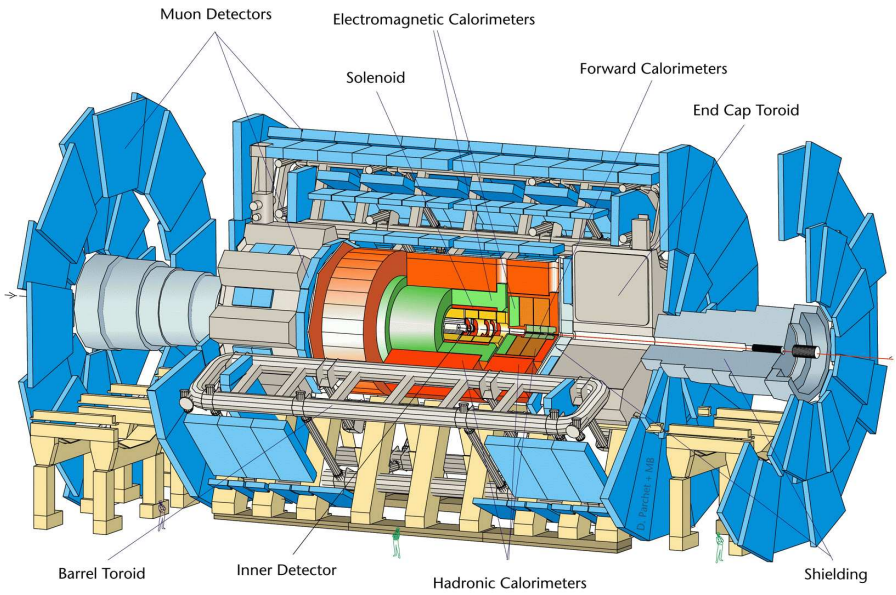

Figure 2.2: *Three dimensional view of the ATLAS detector.*

ATLAS is a cylindrical detector defined by the cylindrical coordinate system (z,R,ϕ), where z is the position in the direction along the beam axis, R the radius and ϕ the azimuthal angle. With these ones, the transverse momentum (the momentum of the particle in the R direction) and the pseudorapidity

$\eta = -\ln \tan \frac{\theta}{2}$ [1] where θ is the polar angle (between the particle trajectory and the beam axis) are variables much used to describe the trajectories of the particles.

The detector is composed by a barrel and two end-caps regions, where the barrel is the cylindrical region around the beam axis and the end-caps are wheels on the $R\phi$ plane perpendicular to the beam axis.

The innermost detector, around the interaction region is the Inner Detector. It is contained within a cylinder of length 7 m and radius of 1.15 m, in a solenoidal magnetic field of 2 T, generated by a thin superconducting solenoid surrounding its cavity. It provides pattern recognition and precise measurements of vertex and momentum, combining the measurements of the high-resolution semiconductor pixel and strip detectors (inner part of the tracking volume) with the straw-tube tracking detectors with transition radiation capability (outer part).

The Calorimeter system is located between the Inner Detector and the Muon Spectrometer. The first part is the Electromagnetic Calorimeter, a high granular liquid-argon (LAr) sampling calorimeter, that measures with great accuracy the energy of the shower produced by the photons, the electrons and the positrons that cross dense material. After that, there is the Hadronic Calorimeter, a scintillator-tile calorimeter in the barrel region $|\eta| < 1.7$ and a LAr calorimeter in the end-caps ($1.7 < |\eta| < 3.2$) and in the forward region ($3.2 < |\eta| < 4.9$), that provides an energy measurement of jets.

The Calorimeter is surrounded by a large superconducting air-core toroidal magnet consisting of independent coils arranged in an eight-fold symmetry, and generating a large magnetic field with a strong bending power within a light and open structure where the Muon Spectrometer is installed. The chambers of the Muon Spectrometer are mounted in three stations, minimizing the effect of multiple scattering and thereby achieving good momentum resolution, so muons with sufficient energy to cross all subdetectors are identified and their momentum measured.

The subdetectors and the trigger system are briefly introduced in the following sections.

2.3 Magnetic System

The ATLAS magnetic system consists of a central solenoid (CS) covering the Inner Detector, and three large air-core toroids, two in the end-caps (ECT) and one in the barrel (BT) that generate the magnetic field in the Spectrometer, see Figure 2.3 ([34]).

The CS provides a solenoidal field of 2 T with a peak of 2.6 T in the windings, this field is not uniform in Z nor in R direction, as shown in Figure 2.4. The position in front of the Electromagnetic Calorimeter requires

[1] The rapidity is defined as: $\ln \frac{(E+P_x)}{(E-P_y)}$, the pseudo-rapidity is the rapidity in the approximation of zero mass.

a careful minimization of matter in order to avoid showering from particles before entering the Calorimeter.

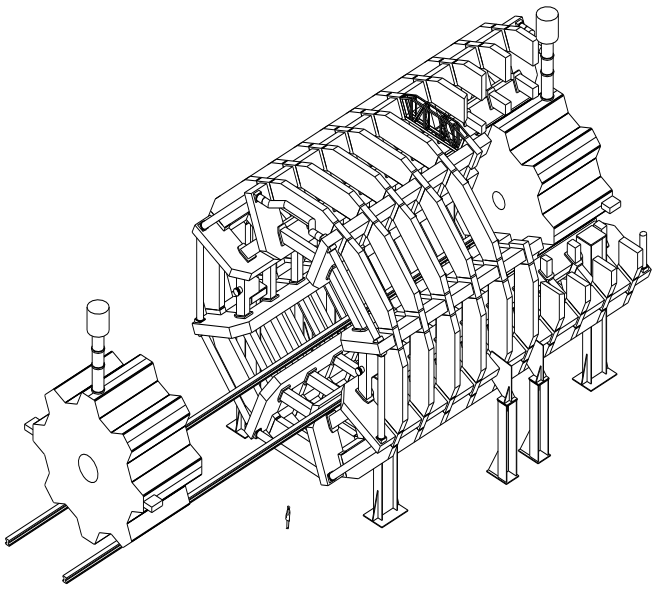

Figure 2.3: *View of the superconducting air-core toroid magnet system.*

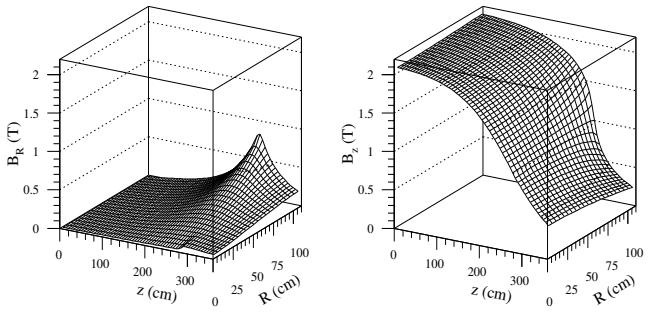

Figure 2.4: *The right plot shows the B_z field as a function of z and R. The left plot shows the B_R field as a function of z and R.*

Each of the three toroids, ECT and BT, consists of eight coils assembled radially and symmetrically around the beam axis in an open structure, providing a magnetic field peaked on 3.9 T (BT) and 4.1 T (ECT). Every coil of BT has its own cryostat, with the coils connected together by voussoirs and struts that provide mechanical stability. Each ECT, instead, is housed in a single large cryostat. All the magnets are indirectly cooled by a flow of helium at 4.5 K. The bending power of toroids is defined by the field integral $\int Bdl$, where B is the azimuthal field component, and the integral is taken on a straight line trajectory between the inner and the outer radius of the toroids. A scheme of the field line in the spectrometer is shown in Figure 2.5.

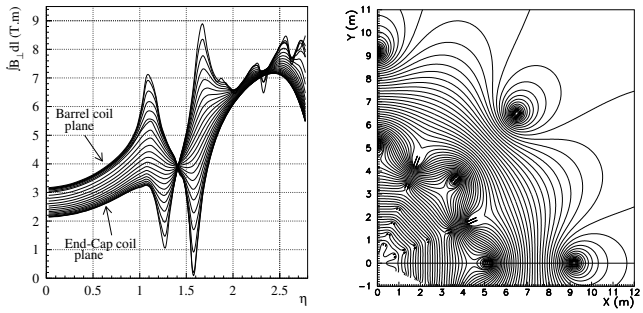

Figure 2.5: *Right picture: magnetic toroid field map in the transition region; lines are drawn in a plane perpendicular to the beam axis in the middle of an end-cap toroid. Left picture: toroid bending power* $\int Bdl$ *of the azimuthal field component, integrated between the first and the last muon chamber, as a function of the pseudorapidity.*

2.4 Inner Detector

The Inner Detector combines high resolution detectors at the inner radii, with continuous tracking elements at the outer radii covering the range of $|\eta| < 2.5$, see Figure 2.6 ([35]).

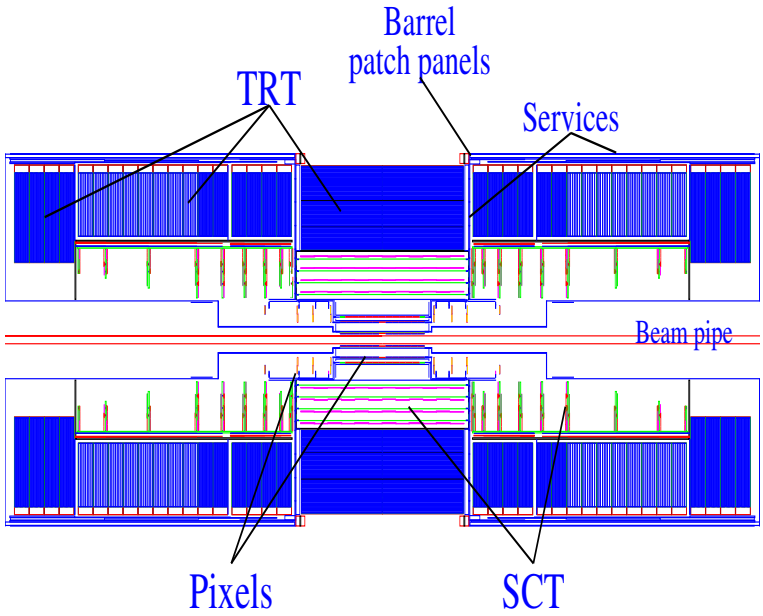

Figure 2.6: *RZ view of the Inner Detector with its subdetectors.*

The overall layout consists of three different technologies: pixel detectors at radii between 5 and 15 *cm* from the interaction region and micro-strip detectors at radii between 30 and 50 *cm* (SCT), then straw tube tracker at outer radii (TRT) (see Table 2.1).

The first two detectors have a very high granularity, to measure with very good resolution the momentum and the position of the vertex.

System	η coverage	Position in cm	Resolution in μm
Pixels	± 2.5	ΔR: 11.5-21.3	$\sigma_{R\phi}$=12 σ_z=66
	$1.5 - 2.7$	end-caps	$\sigma_{R\phi}$=12 σ_R=77
Silicon Strips(SCT)	± 1.4	R: 30, 40, 50, 60	$\sigma_{R\phi}$=16 σ_z=580
	$1.4 - 2.5$	end-caps	$\sigma_{R\phi}$=16 σ_z=580
TRT	± 2.5	ΔR: 56-107	$\sigma_{perstraw}$=170

Table 2.1: *Parameters of the Inner Detector.*

The detector was carefully designed to minimize dead material. An excess of material causes deterioration of the detector performance via loss of low momentum particles, multiple Coulomb scattering affecting resolution, electron bremsstrahlung and photon conversion $\gamma \rightarrow ee$ (this leads a reduction of the important $H \rightarrow \gamma\gamma$ signal).

Using the space-point measurements of the different inner tracker layers, the helicoidal trajectory of the track is reconstructed. The five helix fit parameters refer to the point of closest approach to the beam axis ($x = 0, y = 0$). In the x-y plane, the fitted parameters are:

$(1/p_T)$ the reciprocal of the transverse momentum ($p_T = \sqrt{p_x^2 + p_y^2}$);

ϕ defined by $tan\,(\phi) = p_y/p_x$;

d_0 the transverse distance to the beam axis.

In the R-z plane, the fitted parameters are:

$\cot\theta \; = tan\,(\lambda) \equiv p_z/p_T$

z_0 the z position of the track at this point.

Simulations of the inner tracker response to minimum-ionizing-particles (muons) yield the following parametrization, in terms of the track transverse momentum and polar angle θ, for the errors on the five helix parameters:

$$\begin{aligned}
\sigma\left(\frac{1}{p_T}\right) &\approx \left[0.36 \oplus \frac{13}{p_T\sqrt{\sin\theta}}\right](TeV^{-1}) \\
\sigma(\phi) &\approx \left[0.075 \oplus \frac{1.8}{p_T\sqrt{\sin\theta}}\right](mrad) \\
\sigma(\cot\theta) &\approx 0.70 \cdot 10^{-3} \oplus \frac{2.0 \cdot 10^{-3}}{p_T\sqrt{\sin^3\theta}}
\end{aligned}$$

$$\begin{aligned} \sigma(d_0) &\approx \left[11 \oplus \frac{73}{p_T\sqrt{\sin\theta}}\right](\mu m) \\ \sigma(z_0) &\approx \left[87 \oplus \frac{115}{p_T\sqrt{\sin^3\theta}}\right](\mu m) \end{aligned} \tag{2.4.1}$$

2.4.1 Pixel Detector

The pixel detector is designed to achieve high precision as close to the interaction region as possible; the system provides three precise measurements over full solid angle (typically three pixel layers are crossed), with the possibility to determine the impact parameter and to identify the short-life particles.

There are three layers of pixels where each pixel is 50 μm wide in $R\phi$ and 300 μm long. Thus the pixel detector yields good resolution in the bending plane of the solenoidal magnetic field, essential for transverse momentum measurement, see Figure 2.7. The position along the beam axis is measured with slightly less precision.

The inner layer (called the B-layer because of the important role in B-Physics) covers full rapidity range $|\eta| < 2.5$. The other two barrel layers cover the rapidity range $|\eta| < 1.7$. Three end-cap disks are used to provide additional space points in the forward regions $1.7 < |\eta| < 2.5$ ([35]).

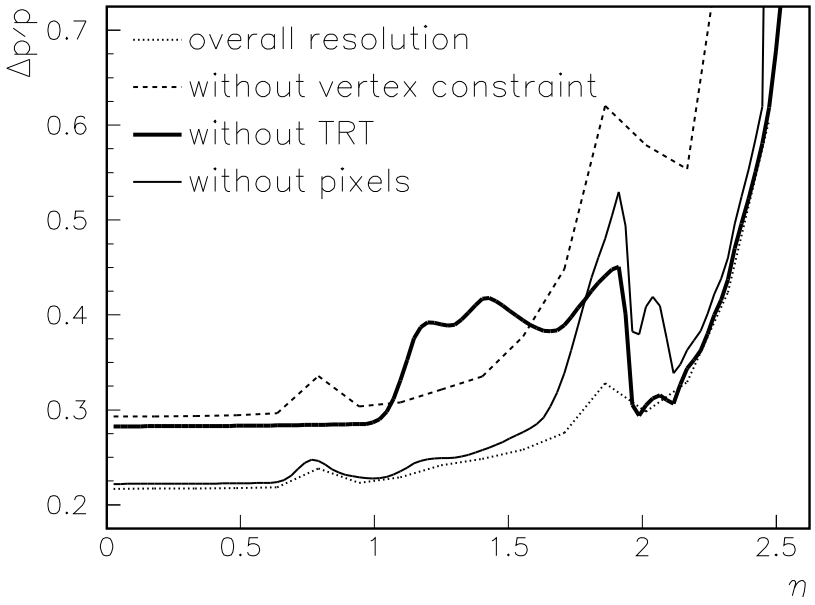

Figure 2.7: *Momentum resolution for single muons of p_T = 500 GeV.*

2.4.2 SCT

The semi-conductor tracker (SCT) is designed to obtain eight precision measurements per track at radii from 30 to 56 cm, contributing to the measure-

ments of momentum, impact parameter and vertex position.

It consists of four double layers of silicon strips, with each double layer composed by strips aligned in the azimuthal direction and strips rotated by 40 $mrad$ with respect to the first set. The combination of the two measurements allows the determination of a two-dimensional space point with a resolution in $R\phi$ plane of $\approx 17\mu m$ and in the z coordinate of $\sim 570\ \mu m$ to resolve ambiguities in the pattern recognition (assigning hits to track in the dense tracking environment). The strips have 80 μm pitch and are 12 cm long covering a large area (60 m^2) with a relatively small number of readout channels ($\sim$ 6 million) ([35]).

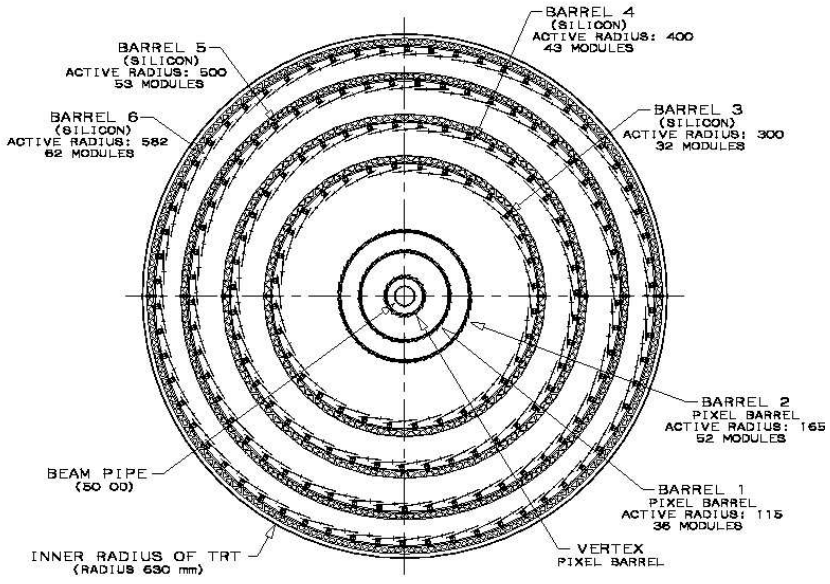

Figure 2.8: *Transverse section of the Inner Detector. The picture shows the position of the sub-detectors at different radii.*

2.4.3 TRT

The TRT is based on straw detectors; they are used at large radii where the track density is relatively low giving a number of 36 points per track. This insures good pattern recognition performance for a continuous tracking. It consists of 36 layers of 4 mm diameter straw tubes with a resolutions of $\sim 200\ \mu m$, inter-spaced with a radiator to emit transition radiation (TR) from electrons. There are two thresholds for recording hits, the high threshold being used to detect TR photons. The emission of TR photons is a phenomenon with a threshold which depends on the relativistic velocity p/m, at $\beta\gamma \geq 1000$. Charged particle that cross an inhomogeneous medium, with materials of different electrical properties, emits a transition radiation in the X-rays region.

In the TRT, multiple polyethylene foils act as radiators. Interleaved with the radiator are layers of straws filled with a gas mixture. These have a dual

functionality; the same straws measure the passage of charged particle through the gas ionization and the transition radiation X-rays absorbed by the gas molecules.

The number of transition radiation emissions along the track forms a powerful discriminant variable for electron/pion separation. This separation improves when the electron p_T increases from 0.5 GeV to $4 - 5$ GeV, while for greater p_T the separation decreases, because at higher energies the relativistic rise in dE/dx causes the pions to deposit more energy and the number of TR photons emitted to become comparable with the number of TR photons emitted by electrons ([33]).

2.5 Calorimeter System

The Calorimeter system consists of the Electromagnetic (EM) Calorimeter covering the pseudorapidity region $|\eta| < 3.2$, the Hadronic barrel Calorimeter covering $|\eta| < 1.7$, the Hadronic end-cap Calorimeters covering $1.5 < |\eta| < 3.2$, and the forward Calorimeters covering $3.1 < |\eta| < 4.9$ ([34]). See Figure 2.9 for more details.

Hadrons produce a cascade of hadron-nucleus interactions. The longitudinal development of the shower is determined by the interaction length of the material. Hadronic showers contain a variable electromagnetic component from π^0 decays. The shower shape of the hadronic showers is more irregular than the shape of the electromagnetic showers ([36]). The ratio between the response of the Calorimeter to purely hadronic and purely electromagnetic part of the shower is called the e/h ratio. For a good energy resolution the value of e/h should be as close as possible to one. The size of hadronic shower depends on the interaction length of the material which is always longer than the radiation length. The radiation and interaction length are material dependent. Generally, for dense materials, the interaction length is up to an order of magnitude longer than the radiation length. This property is used in the ATLAS Calorimeters to separate the electromagnetic and hadronic showers.

The identification of electrons and photons is the most important issue for the Calorimeters. Such a rejection can be achieved with a Calorimeter of fine granularity in both the EM and hadronic part to identify isolated energy depositions from electrons/photons and to veto on hadronic energy behind the cluster in the EM Calorimeter.

The hight density of the EM Calorimeter makes the difference between radiation and interaction length quite large, thus providing a good separation of the two types of showers and at the same time a compact EM Calorimeter.

The design of the Electromagnetic Calorimeter is driven by the requirements for energy and spatial resolution for the Higgs processes involving decays to electrons or photons. The $H \rightarrow \gamma\gamma$ decay of a standard model Higgs has a large background and a mass resolution around 1% is required. The dynamic range for the Calorimeter in transverse energy extends from around 1 GeV for electrons from B-meson decays to a few TeV for the decay of a heavy vector

boson.

The measurement of missing transverse energy is a way to measure particles escaping the detector without interactions. This can be either neutrinos or stable supersymmetric particles. To identify missing transverse energy the Calorimeter needs to be hermetic. This means that the rapidity coverage has to reach $|\eta| = 5$ and any crack in the detector for cables and cooling has to be minimized.

Also the Hadronic Calorimeter needs to be thick enough to avoid leakage of hadrons into the muon system which would reduce the resolution in missing transverse energy and give background in the muon system. A compromise between the total size of the ATLAS detector, the stopping power for low energetic muons, an acceptable rate of punch-through to the muon system and a good resolution in missing transverse energy, requires 11 absorption lengths of material in front of the muon system.

To minimize the fluctuations in the response of the Hadronic Calorimeter a low Z material with comparable interaction length and radiation length is a good choice. However, a compromise has to be made with the total size of the Calorimeter which favours high density materials.

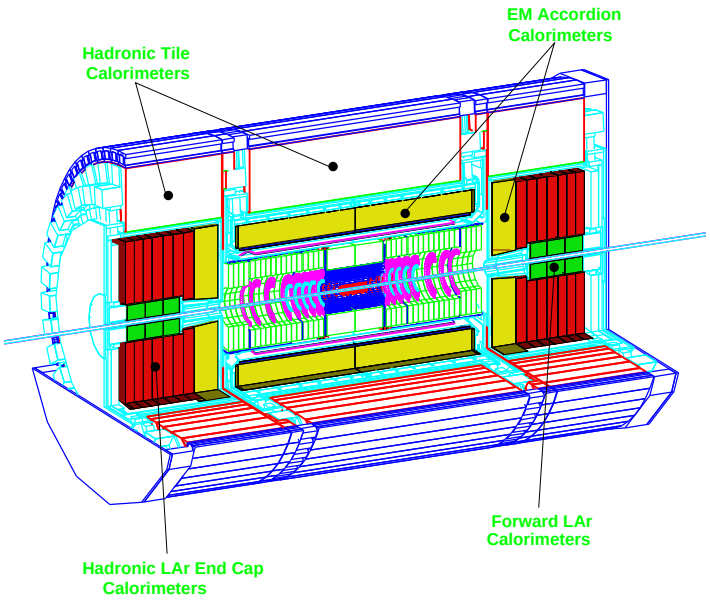

Figure 2.9: *Layout of the Calorimeter system.*

The energy resolution in the Calorimeters is given by:

$$\frac{\sigma(E)}{E} = \frac{a}{\sqrt{E}} \oplus \frac{b}{E} \oplus c \tag{2.5.1}$$

where a depends on the stochastic fluctuations, b on the electronic noise and c on the calibration ([37]).

2.5.1 Electromagnetic Calorimeter

The EM Calorimeter must be able to identify and accurately reconstruct electrons and photons over a wide energy range and must have ([38]):

Large Acceptance. Important in searching for rare processes at the LHC (e.g. $H \to \gamma\gamma$ and $H \to ZZ$). This requires a large rapidity coverage too.

High Segmentation. The optimization of the transverse and longitudinal segmentation of the EM Calorimeter involves balancing performance issues such as electron and photon identification, position resolution, and pile-up and electronic noise contributions against cost and technical constraints ([39], [40]).

The dominant backgrounds to electrons and photons arise from the production of hadronic jets. The most stringent physics requirement comes from the search for the $H \to \gamma\gamma$ decay, which needs a rejection factor of about 10^4 against single jets.

The longitudinal and transverse segmentation of the EM Calorimeter gives a measure of the shower shape and is therefore an essential tool in rejecting jet backgrounds.

Good Energy Resolution. The most demanding channels are again $H \to \gamma\gamma$ and $H \to ZZ$. In the energy domain of interest for these processes, typically $10-100\ GeV$, the sampling term and the constant term as well as the pile-up and electronic noise all contribute significantly to the energy resolution. A stochastic term of $\leq 10\%/\sqrt{E(GeV)}$ and a constant term of less than 1% are considered adequate to provide good sensitivity to these channels.

Calorimeter Thickness. Shower leakage behind the EM Calorimeter contributes to the constant term. A minimum depth of 26 X_0 in the barrel and 28 X_0 in the end-cap is adequate to achieve the desired constant term.

Good Angular Resolution. A measurement of the shower direction with a resolution of about $40\ mrad\ /\sqrt{E(\mathrm{GeV})}$ is needed to accurately reconstruct invariant masses of purely neutral states (e.g. $H \to \gamma\gamma$) at high luminosity.

The EM Calorimeter is a dense, high-granularity Liquid Argon Calorimeter, that allows to measure the energy of photons and electrons, see Figure 2.10. The electromagnetic shower develops in lead absorber plates. The thickness of the absorber plates is 1.5 mm in the barrel section and 1.7 mm and 2.2 mm in the first and second end-cap wheel. The absorbers are folded into an accordion shape and oriented along R (z in the end-caps) to provide complete ϕ symmetry without azimuthal cracks, as shown in Figure 2.11.

The energy measurements are based on the determination of the ionization energy loss by charged components of the shower (electrons and positrons) in thin ($2-6\ mm$) gaps between absorber plates: this gaps are filled with Liquid Argon and equipped with multiple electrodes.

The total EM Calorimeter presents 24 (26) radiation lengths in the barrel (end-caps) region to reduce the error in the energy resolution due to longitu-

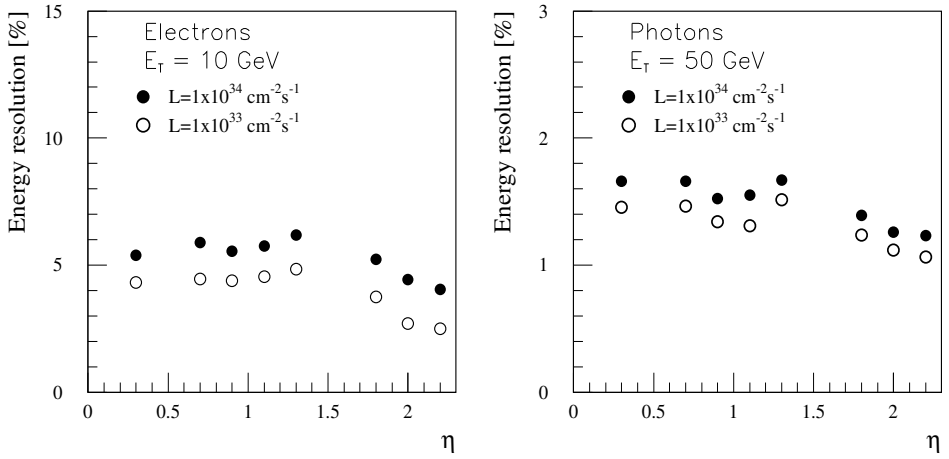

Figure 2.10: *Different energy resolutions for electrons (left plot) and photons (right plot) at high (black points) and low luminosity (empty circles). The comparison is for electrons with E_T = 10 GeV and photons with E_T = 50 GeV.*

dinal fluctuations of high energy showers.

The particle identification is achieved by a fine longitudinal and lateral segmentation. The EM Calorimeter is longitudinally segmented in three layers plus a pre-shower sampler that corrects the energy loss in the material in front of the EM.

2.5.2 Hadronic Calorimeter

The requirements for the Hadronic Calorimeter are: identify jets and measure their energy and direction, measure the total missing transverse energy (E_T^{miss}), and enhance the particle identification capability of the EM Calorimeter by measuring quantities such as leakage and isolation ([41]).

The reconstruction of both E_T^{miss} and jet energy are limited by intrinsic effects. The jet energy, estimated by measuring the energy deposited in a cone around the jet axis, is subject to several uncertainties. Among these are e.g. fragmentation and magnetic field sweeping of charged particles. Some energy is also lost in non interacting particles (neutrinos, muons). To obtain these effects, the hadron Calorimeter must have:

Good Energy Resolution and Linearity. Good jet energy resolution and also excellent control of systematic errors on the jet energy scale, the resolution functions is:

$$\frac{\Delta E}{E} = \frac{50\%}{\sqrt{E}} + 3\% \tag{2.5.2}$$

Fine Segmentation. A good efficiency and large background rejection is obtained by a well-segmented Hadronic Calorimeter.

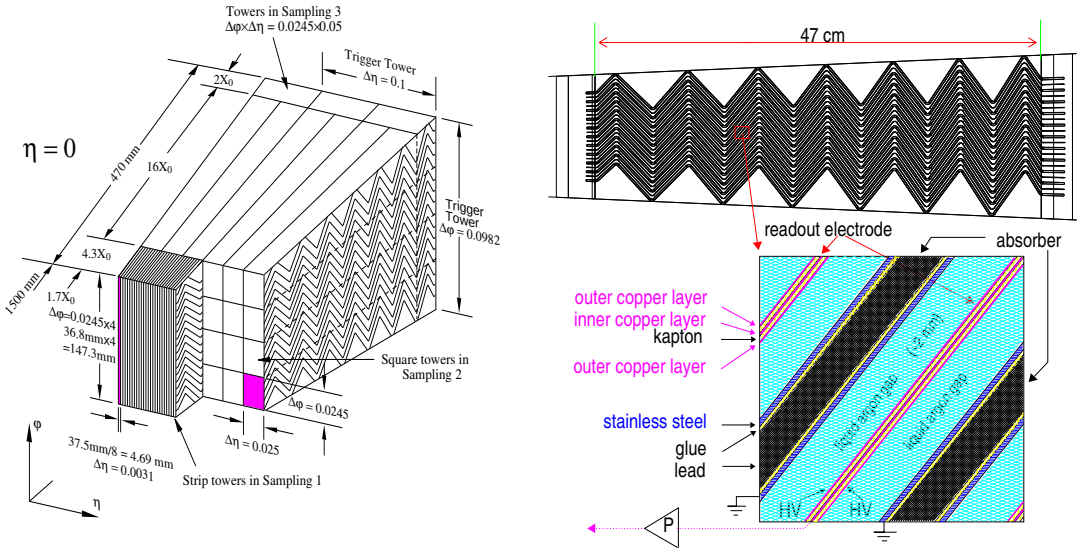

Figure 2.11: *Readout scheme of the EM Calorimeter, in evidence the accordion structure.*

Acceptance and Calorimeter Thickness. The measurement of E_T^{miss} is important for Higgs and SUSY particle searches and places demands on the rapidity coverage, the total Calorimeter thickness, and the tolerable energy loss in cracks. Energy loss in the cracks between the barrel and the end-caps, or between the end-caps and the forward Calorimeter, should be kept small. The invariant mass resolution depends strongly on the E_T^{miss} resolution.

The hadronic calorimetry in the barrel region uses iron absorbers with scintillator plates. This technique offers good performance combined with simple, low-cost construction. At larger rapidity, where higher radiation resistance is required, the hadronic calorimetry is based on the use of liquid argon.

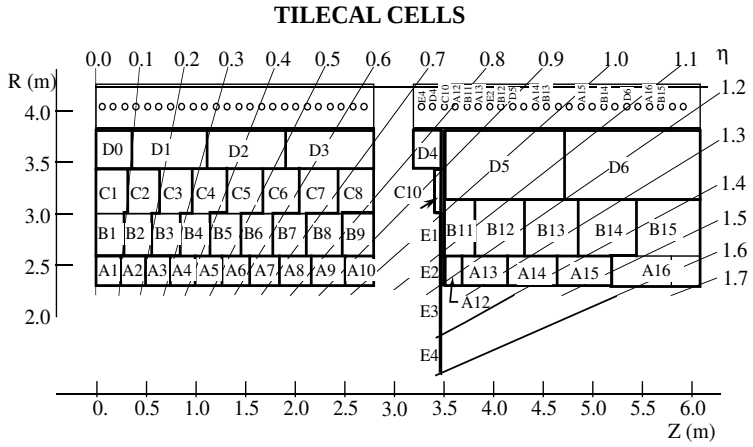

Figure 2.12: *Trigger tower scheme of the Tile Calorimeter.*

The barrel region is composed by one central barrel and two extended barrels yielding a total pseudorapidity coverage of $\eta < 1.7$. Three longitudinal

sections present 1.4, 3.9, and 1.8 interaction lengths to incoming hadronic particles. The total thickness, summing the 1.2 λ in the Electromagnetic Calorimeter and the extra material in the support structures, reaches 11 λ. The geometry adopted consists of scintillator and iron tiles staggered in planes perpendicular to the beam axis. The readout used for a tile is a wavelength-shifting fiber for both sides coupled radially to the scintillator and two photo-multiplier tubes; the cells are grouped in bundles to form readout cells of the desired segmentation($\delta\eta \times \delta\phi = 0.1 \times 0.1$), as shown in the drawings 2.12 and 2.13.

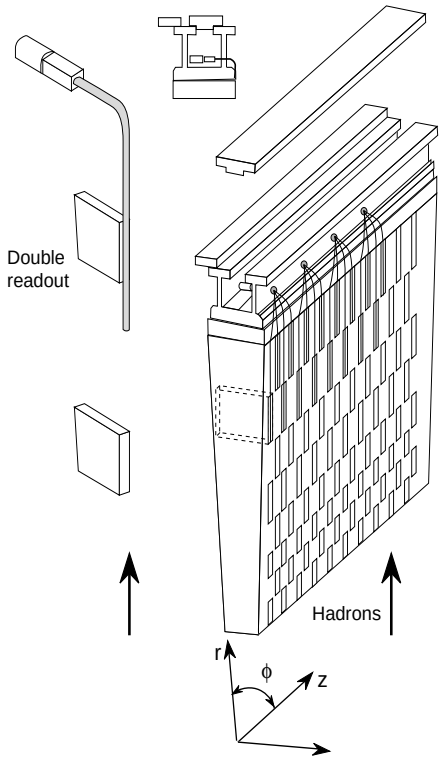

Figure 2.13: *View of a Tile module.*

2.6 Muon System

The Muon Spectrometer has been designed to measure transverse momentum, pseudorapidity and azimuthal angle of muons. Many physics processes of interest involve the production of muons. Therefore, the identification of muons provide an important signature for the event selection (trigger) of the experiment. Also, the accurate determination of the momenta of the muon pairs allows the precise reconstruction of the short-lived particles that decay into muons (for example the detection of a supersymmetric Higgs boson decay through muons in the final state).

The overall layout of the Spectrometer is reported in Figure 2.14, which shows the different technologies employed ([42]).

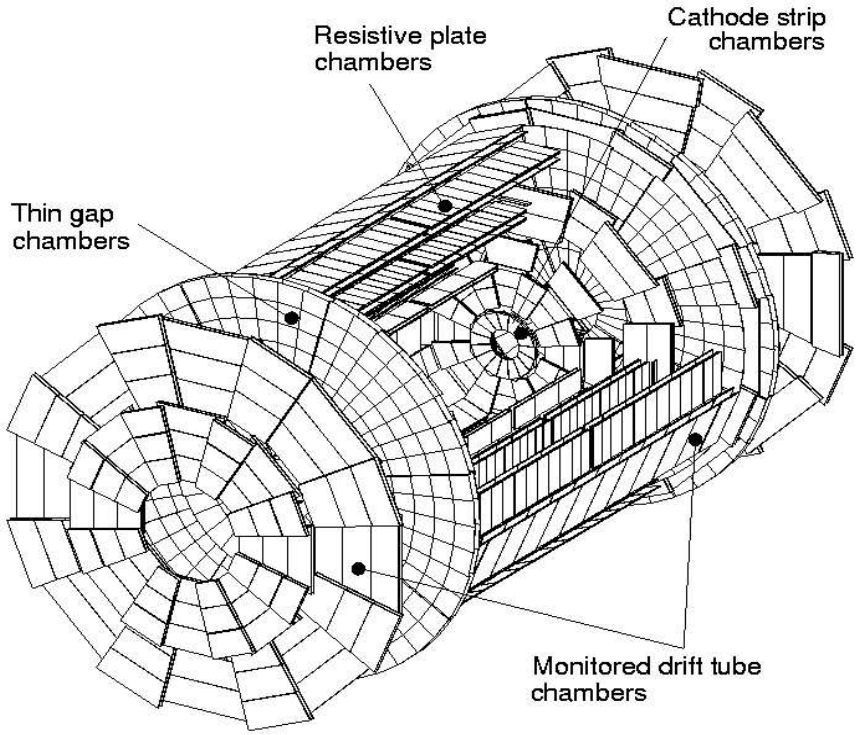

Figure 2.14: *View of the ATLAS Muon Spectrometer.*

The possibility to have an accurate measurement of the muon momentum, independently from the inner detector, is achieved by integrating three large subsystems:

- A toroidal magnetic field generated by a large air-core barrel toroid and two air-core end-caps toroids, that produce a magnetic field peaked on 3.9 T and 4.1 T respectively, minimizing the multiple scattering of the particle thanks to its air-structure.

- A muon first level trigger obtained by the fast signal of the dedicated chambers: Resistive Plate Chamber (RPC) in the barrel region and Thin Gap Chamber (TGC) in the end-cap region. These chambers determine the global reference time (bunch crossing identification) and the muon track coordinate in the non-bending direction.

- A system for precision momentum measurements via Monitored Drift Tube (MDT), and Cathode Strip Chambers (CSC) in the region $|\eta| > 2.7$.

The chambers are positioned in three stations along the muon trajectory. In the barrel, the three detector stations are mounted concentrically around the beam line at 5 m (inner), 7 m (middle) and 10 m (outer) radial distance. The chambers are arranged in projective towers (alignment rays monitor their position). In the end-caps, the disks are mounted perpendicularly to the beam line at 9 m (inner), 14 m (middle) and 20 m (outer) from the interaction region.

The precision measurements of the muon momentum in the barrel region are based on the sagitta of three stations in the magnetic field, where the sagitta is defined as the distance from the point measured in the middle station to the straight line connecting the points in the inner and outer stations.

In the end-caps, the situation is different; the magnetic field is present only between the inner and the middle stations, therefore the momentum is determined with a point-angle measurement: a point in the inner station and an angle in the combined middle-outer stations.

The ATLAS Muon Spectrometer has been designed to provide a good stand-alone momentum measurement, the transverse momentum should be measured with a resolution of $\Delta p_T/p_T = 10\%$ at $p_T = 1\ TeV$. Since the bending of the 1 TeV muon track is such that the track sagitta varies between 500 μm in the barrel and 1 mm in the end-cap, the error on the sagitta measurement must be at level of 50 μm. These requirements have been successfully achieved as the analysis, discussed in detail in Chapter 5 of this thesis, has demonstrated.

2.6.1 MDT Chambers

The MDT chambers perform the precision coordinate measurement in the bending direction of the air-core toroidal magnet and therefore provide the muon momentum measurement. They cover the barrel η range of $|\eta| < 2.7$.

The basic detector element is a cylindrical aluminum drift tube of 30 mm diameter and a anodic gold-plated W-Re central wire of 50 μm diameter at 3080 V high voltage. The tube is filled with a non flammable gas mixture of 93% Ar and 7% CO_2 at 3 bar absolute pressure. A muon crossing the drift tube ionize the gas along its track. The ionization electrons drift towards the wire in the electric field and are multiplied in an avalanche process close to the wire. The current inducted on the wire is read out by a low-impedance current sensitive preamplifier followed by a differential amplifier and a discriminator. The output of the shaping amplifier is connected to a Wilkinson ADC and TDC for charge-integrated signal and drift time measurements. The measured drift-time is converted to a distance using the $r(t)$ space-time relation typical of the gas mixture. The chosen mixture provides a non-liner space-time relation with a maximum drift-time of $\sim 700\ ns$, a small Lorentz angle and good ageing properties (see e.g. Chapter 6 of this thesis). The average spatial resolution of a single tube is expected $\sim 80\ \mu m$.

To improve the resolution of the chamber beyond the single-wire limit and to achieve adequate redundancy for pattern recognition, the MDT chambers

are made up of two multilayers each. Every multilayer consists of 4 layers of drift tubes, for the inner stations, or 3 layers, for the middle and outer stations. See Figure 2.15 ([34]). This structure provides an accurate positioning of the drift tubes and good mechanical integrity under effects of temperature and gravity. Wires and tubes have been assembled with a precision of 20 μm. Moreover, to achieve the desired high transverse momentum resolution, an excellent optical system is required both for checking the in-chamber deformations and the relative displacement between different chambers.

The transverse momentum resolution in the barrel section is shown in Figure 2.16.

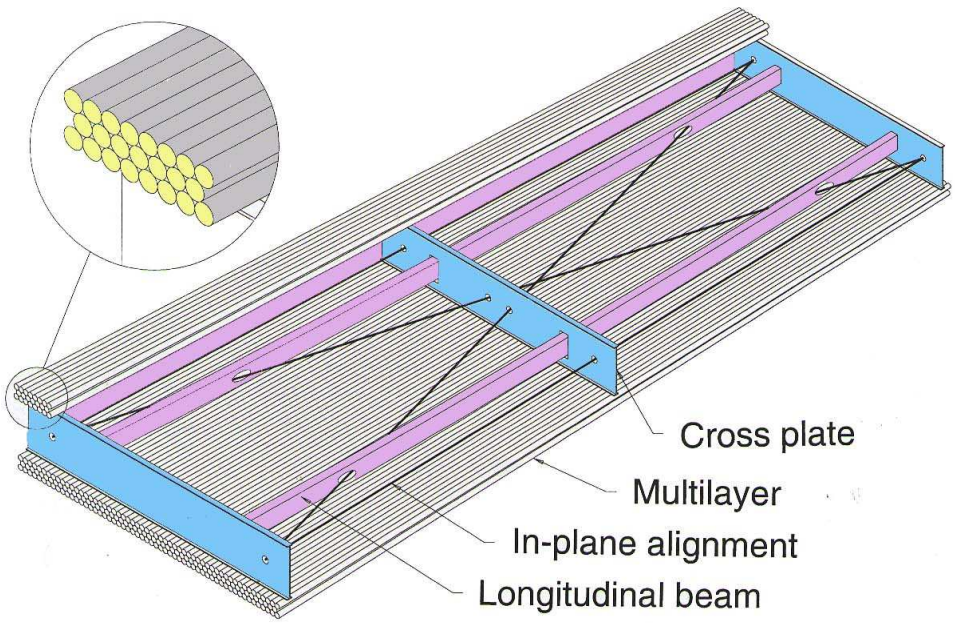

Figure 2.15: *Schematic drawing of an MDT chamber. All the structural elements are shown (2x3 layers of tubes).*

2.6.2 CSC Chambers

The Cathode Strip Chambers are multiwire proportional chambers with a cathode strip readout and with a symmetric cell where the anode-cathode spacing is equal to the anode wire pitch, see Figure 2.17, filled with a $Ar(30\%)$ $CO_2(50\%)$ $CF_4(20\%)$ gas mixture. The avalanche in the gas on the anode wire induces a signal on the segmented cathode.

The cathode strips are oriented orthogonally to the anode wire and are segmented, to obtain a position measurement with a resolution of ≈ 60 μm. Other important characteristics are: good time resolution (7 ns), good track reconstruction and small electron drift time ([34]).

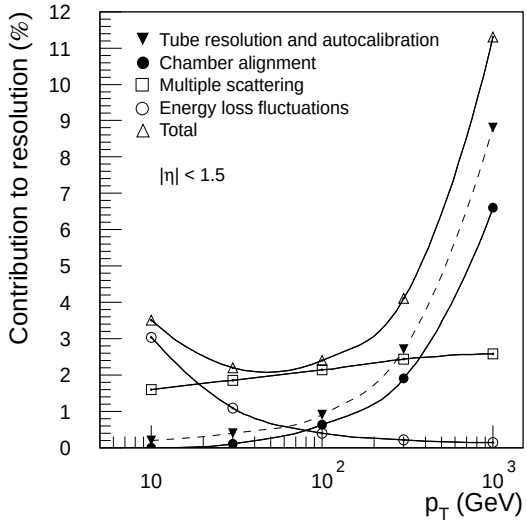

Figure 2.16: *$\Delta p_T/p_T$ as a function of p_T for muons reconstructed in the barrel region ($\eta \leq 1.5$).*

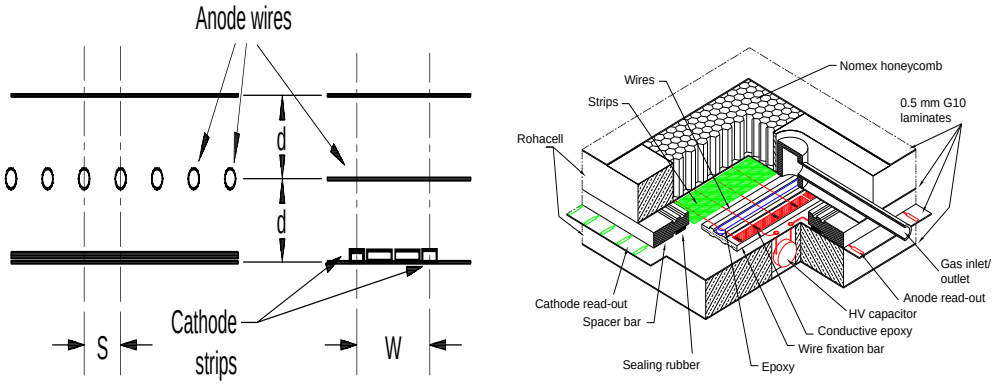

Figure 2.17: *Schematic drawing of the Cathode Strip Chamber.*

2.6.3 RPC Chambers

The Resistive Plate Chambers consist of a narrow gas ($C_2H_2F_4$) gap between resistive bakelite plates covered with readout strips at the pitch of $30-39$ mm, see Figure 2.18.

A trigger chamber is formed by two rectangular detector layers, each one read out by two orthogonal series of pick-up strips: the η strips are parallel to the MDT wires and provide the bending view of the trigger detector, the ϕ strips, orthogonal to the MDT wires, provide the second coordinate measurement which is also required for the offline pattern recognition.

The RPCs combine an adequate spatial resolution of 1 cm with an excellent time resolution of 1 ns. The use of the two perpendicular orientations allows the measurements of the η and ϕ coordinates.

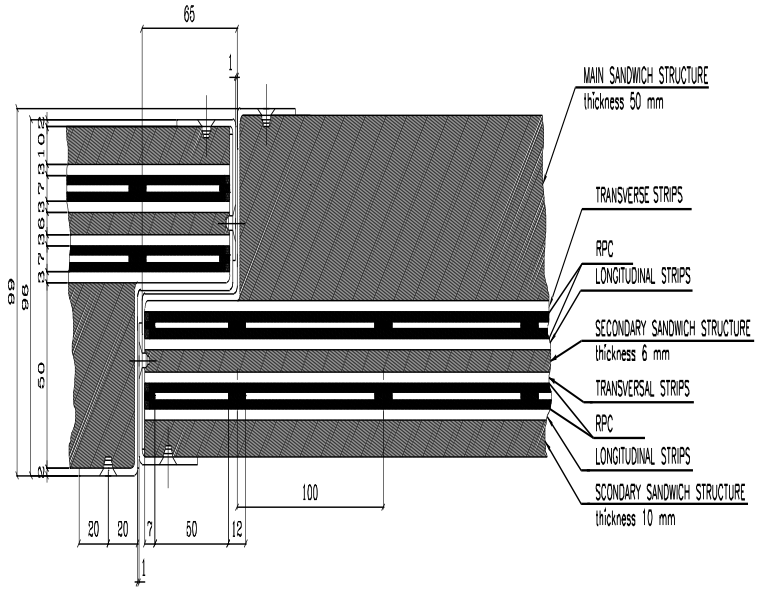

Figure 2.18: *Structure of an RPC chamber.*

2.6.4 TGC Chambers

The Thin Gap Chambers are multi-wire proportional chambers, with the important feature that the anode wire pitch is larger than the cathode-anode distance, filled with a highly quenching gas mixture of $CO_2(55\%)$ and $n-pentane(45\%)$, see schematic TGC drawing in Figure 2.19.

This allows operation of the chambers in the saturated mode, with the following advantages: small sensitivity to mechanical deformations, nearly Gaussian pulses, with small Landau tails and no streamer formation.

TGCs are constructed in doublets and triplets. The layers in the middle station are arranged in one triplet and two doublets while in the inner station there is only one doublet that measures the ϕ coordinate. The anode wire, parallel to the MDT wires, provide the trigger information together with the readout strips arranged orthogonally to the wires.

2.7 The Trigger System

The high design luminosity of $10^{34}cm^{-2}s^{-1}$ of LHC will lead to more than 20 interactions per bunch crossing. Thus, each second nearly 10^9 interactions will occur. Most of these interactions are minimum bias events that have a limited interest. Such a high data flux ($\approx 1.5\ MB$ every $25\ ns$) is far from the current data storage technology rate, that corresponds to a maximum trigger rate of $\approx 100Hz$ ([43]).

The trigger system is designed to bridge this gap, maintaining nearly all interesting physics events, while efficiently rejecting the minimum bias background. The system must be able to take a decision in a short time (latency time) without any loss of interesting physics events. The decision is achieved

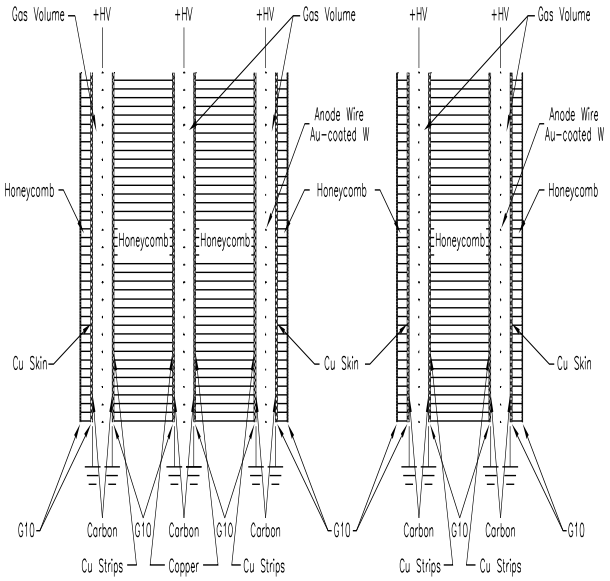

Figure 2.19: *Schematic cross-section of a triplet (left) and of a double of TGCs.*

into three different steps or trigger levels, see Figure 2.20.

The first level trigger (LVL1) is designed to operate at a maximum pass rate of 75 kHz. The LVL1 latency is 2 μs ([44]). The information of all detector channels must be stored in "pipeline" memories, because the LVL1 latency extends over many of the 25 ns spaced LHC bunch crossings. The LVL1 decision is based on information with a coarse granularity of two sub-detector systems: the muon trigger chambers and the Calorimeters. Quantities used in the LVL1 decision are: the estimated transverse momentum of muon candidates, the total energy deposited in the Calorimeters, the missing (transverse) energy in the Calorimeters and the occurrence of isolated energy depositions in the Calorimeters. For events accepted by the LVL1, the information of all sub-detector systems is pre-processed and stored in the so-called Read-Out Buffers (ROBs).

The second level trigger (LVL2) uses both the LVL1 output and the data stored in the ROBs to further reduce the data rate to a maximum of 1 kHz. Even if the LVL2 has access to the full data, the selection is generally restricted to so-called Regions of Interest as flagged by the output of the LVL1. For a LVL1 muon trigger, the LVL2 will use the information from the precision MDT chambers to improve the muon momentum estimate, which allows a tighter cut on this quantity. For a LVL1 Calorimeter trigger, the LVL2 has access to the full detector granularity, and has in addition the possibility to require a match with a track reconstructed in the Inner Detector. The LVL2 has an event dependent latency, which varies from 1 ms for simple events to about 10 ms for complicated events. For events accepted by the LVL2, the data fragments, stored in the ROBs, are collected by the Event Builder and written into the Full Event Buffers.

The third trigger stage, called Event Filter (EF), uses the information

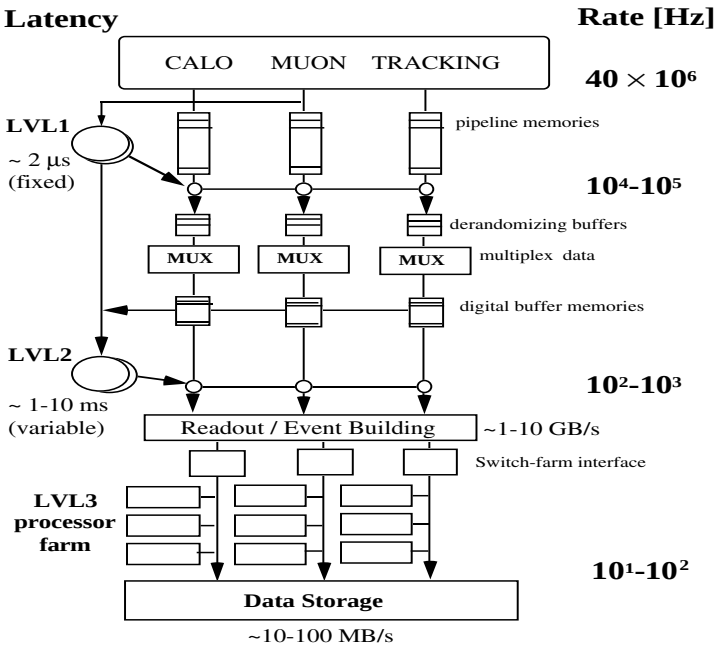

Figure 2.20: *Schematic view of the ATLAS trigger system. The three levels (LVL1, LVL2, LVL3) are indicated, including the latencies for the first two.*

stored in the event buffers to keep the rate of events sent to mass storage at a few hundreds Hz. The EF uses the best algorithms developed for offline reconstruction, like track reconstruction, vertex finding, etc., because it has access to the complete event. The stored data are reconstructed to compute quantities like tracks, energy clusters, jets, missing transverse energy, secondary decay vertexes, etc. These quantities are subject to various physics selection criteria in offline analysis too, for example to maximize the discovery potential for the Higgs particle. For the maximum trigger rate of 100 Hz, the data rate written to mass storage corresponds to 200 MB/s.

2.8 Trigger Requirements for B-Physics

At start up, the target peak luminosity for the LHC will be $2 \times 10^{33}\ cm^{-2}s^{-1}$, rising to the full design luminosity of $10^{34}\ cm^{-2}s^{-1}$ after a few years of running. There will be an average of 4.6 and 23 interactions per bunch crossing for initial and design luminosity respectively. About 1% of collisions produce a $b\bar{b}$ pair. The challenge for the trigger is to select those events of most interest for the ATLAS B-Physics program ([34]), within the limited trigger resources available. The ATLAS B-Physics trigger ([45],[46]) is based on a lepton signature at the first level, which can be accompanied by additional, lower transverse-energy signature of leptons and jets. These signatures are refined in the higher trigger levels where specific decays are reconstructed.

At the peak target luminosity in the initial running (and the target of $10^{34} cm^{-2} s^{-1}$), the B-Physics trigger will be limited to a dimuon trigger. This is based on the detection of two muons found in LVL1 with a p_T threshold of 6 GeV and 4 GeV respectively. At LVL2 and EF, the regions of interest will be confirmed by the precision muon chambers, the Tile Calorimeter, then extrapolated to the ID. The trigger selection is based on identifying candidates for specific exclusive or semi-inclusive decays, for example $J/\Psi \rightarrow \mu^+\mu^-$ and $B \rightarrow \mu^+\mu^-(X)$.

As the luminosity falls to around 10^{33} $cm^{-2} s^{-1}$, further B-trigger can be added based on a single muon trigger plus at least one additional trigger from the semi-inclusive reconstruction of specific decay candidates, for example $J/\Psi \rightarrow e^+e^-$, $B \rightarrow h^+h^-$ and $D_s \rightarrow \phi\pi^{\pm}$. Two strategies have been investigated for these additional triggers: RoI-guided and full-scan. In both cases the LVL1 muon is confirmed at LVL2 using the Calorimeter and Inner Detector.

In the baseline RoI-based strategy the LVL1 trigger provides information on low-E_T, EM and jet RoI in addition to the muon trigger. At LVL2, tracks are reconstructed in the Inner Detector within these RoI and the reconstructed track information is used to search for candidates in specific decays. Track reconstruction and B-decay candidate selection is repeated in the EF, using the LVL1 RoIs again or the LVL2 tracks as seeds. The EF selection is refined by fitting tracks to include secondary vertex information. This approach reduces the resources needed for the B-Physics trigger compared to the full-scan approach. In this second approach, the LVL2 track reconstruction is performed in the full acceptance of the SCT and pixels and the resulting tracks are used to form $B \rightarrow h^+h^-$ and $D_s \rightarrow \phi\pi^{\pm}$ candidates. The TRT can be scanned for tracks in order to identify $J/\Psi \rightarrow e^+e^-$ candidates. The EF can perform another full scan using the LVL2 tracks as seeds. This approach is expected to be more efficient than the RoI-based above, but with a significantly higher resource cost.

2.8.1 Muon Triggers

The LVL1 muon trigger has a logic designed for both low and high p_T thresholds; low p_T is the one used for B-Physics. It uses data from the two inner RPC stations (barrel) and the two outer TGC station (end-cap). The main single-muon background comes from π/K decays in flight. These can be rejected mostly at LVL2, by matching muon tracks to Inner Detector tracks and applying sharp p_T cuts. Figure 2.21 shows how the prompt muon cross section fails with the increasing muon p_T, which means that the trigger rate can be controlled by fine tuning of the threshold. Simulations predict that a p_T threshold of 6 GeV has a LVL1 rate of about 20 kHz at 10^{33} $cm^{-2} s^{-1}$.

For dimuon triggers, lower thresholds are possible if the rates are low enough: $p_T > 4$ GeV in the barrel and $p_T > 3$ GeV in the end-caps. At 10^{34} $cm^{-2} s^{-1}$ the dimuon trigger rate should be below 1 kHz for a 6 GeV threshold, only a small fraction of the total LVL1 rate. Dimuon trigger are

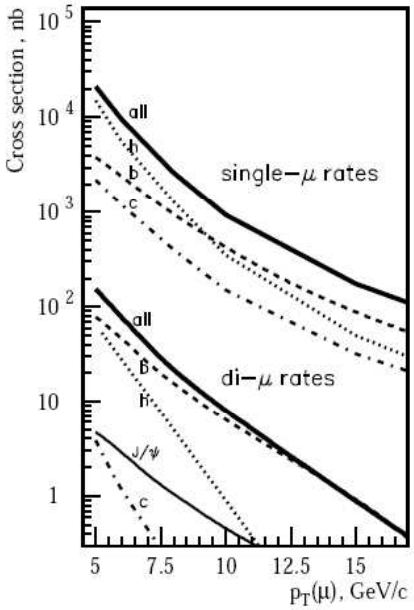

Figure 2.21: *Single and dimuon cross sections.*

used to select decays such as $B^0 \rightarrow J/\Psi(\mu^+\mu^-)K_s^0$ and rare semileptonic decay $B \rightarrow \mu^+\mu^-(X)$.

At LVL2, muon trigger are first confirmed using the precision chambers (MDT). Better track measurement gives a tighter threshold which significantly reduces the trigger rate. Further rejection is obtained by extrapolating tracks to the Inner Detector. Track matching helps to reject muons from π/K decays. At $10^{33}cm^{-2}s^{-1}$ luminosity the rate for a single muon trigger with a threshold of 6 GeV is estimated to be about 5 kHz.

The EF will perform near offline quality track reconstruction, vertex and mass cuts, to select specific decay channels.

2.8.2 LVL1 Jet and EM Cluster Trigger

The LVL1 Calorimeter trigger uses $\sim$ 7000 dedicated Calorimeters towers. The towers have two layers: the Electromagnetic and Hadronic Calorimeter. A window algorithm is used to find cluster which satisfy criteria for EM, tau/hadron and jet selections. A E_T threshold is applied, with isolation in both layers to provide powerful jet rejection. The average multiplicity of LVL1 EM and jet RoI in events with a muon trigger is important as it determines the fraction of the detector that must be read out in order to make the B-trigger decision. Simulation studies using a sample of $b\bar{b}$ events, containing a muon with $p_T > 6$ GeV, have shown that with a jet E_T threshold of 5 GeV there are an average of about 2 RoIs per event. An EM cluster threshold of 2 GeV yields on average about 1 RoI per event.

2.8.3 Hadronic Final States

Tracks found in the SCT and pixels are used to reconstruct the $B \rightarrow h^+h^-$ and $D_s \rightarrow \phi\pi^{\pm}$ decays. Studies show that the RoI-based method should be efficient for a B-hadron with $p_T > 15\ GeV$. At LVL2, kinematic and topological cuts are made to reduce combinatorial background. At EF there is more processing time so the resolutions of reconstructed track parameters are better and vertex fit is available. The rate can therefore be further reduced by tighter mass cuts and using decay length and vertex quality cuts.

2.8.4 Muon and Electron Final States

To select channels such as $B^0 \rightarrow J/\Psi K_s^0$ with $J/\Psi \rightarrow \mu^+\mu^-$ or $J/\Psi \rightarrow e^+e^-$ electron identification is required. ATLAS provides two options for this: use the RoI-based strategy to find silicon tracks guided by EM RoIs, or perform full track reconstruction in the TRT. The RoI-based method is much faster since typically only about 0.3% of the Inner Detector is reconstructed. The lowest nominal threshold possible in the Calorimeter with acceptable RoI multiplicity is 2 GeV and this is not efficient until a higher energy than the minimum threshold possible with a full scan of the TRT. The efficiency to find a separate RoI for both e^+ and e^- with $p_T > 3\ GeV$ is about 80%.

Chapter 3

Simulation and Reconstruction of B-Hadron Events

The MonteCarlo simulation of an high energy physics experiment can be outlined in three main steps:

- **generation**: particles emerging from the collision are generated using MonteCarlo generator codes based on physics theories and phenomenology;
- **simulation**, **digitization**: final state particles are transported through the detector, according to the physics laws of the passage of particles through the matter; interactions with the sensitive elements of the detector are converted into informations with the same format of the digital output from the real detector;
- **reconstruction**: events are reconstructed for physics analysis.

This chapter describes software and methods used to simulate b-quark production at the LHC and the simulation of B-hadron decays. The full simulation and reconstruction of the decays in the ATLAS detector are also described.

3.1 The LCG Project

When the Large Hadron Collider will begin operations in 2007, it will produce roughly 15 Petabytes (15 million Gigabytes) of data annually, which thousands of scientists around the world will access and analyze.

A specific project has been developed to meet the LHC experiment computing needs: the LHC Computing Grid Project (LCG) ([47],[48]), deploying a worldwide computational grid service, integrating the capacities of scientific computing centers spread across Europe, America and Asia into a virtual organization.

Data from the LHC experiments will be distributed around the globe, according to a four-tiered model. A primary backup will be recorded on tape at

CERN, the "Tier-0" center of LCG. After raw data storage and initial processing in quasi-real time, these data will be distributed to a series of Tier-1 centers, large computer centers with sufficient storage capacity for a large fraction of the data, computing resource for reprocessing, and with support for the Grid. The Tier-1 centers will make data available to Tier-2 centers, each consisting of one or several collaborating computing facilities, which can store sufficient data and provide adequate computing power for specific analysis tasks. Individual scientists will access these facilities through Tier-3 computing resources, which can consist of local clusters in a University Department or even individual PCs, and which may be allocated to LCG on a regular basis.

The discovery of new fundamental particles and the analysis of their properties is possible only through statistical analysis of the massive amounts of data gathered by the LHC detectors ATLAS, CMS, ALICE and LHCb, and detailed comparison with compute-intensive theoretical simulations.

LCG includes both the common libraries, tools and frameworks required to support the physics application software, and the development and deployment of the services needed for data storing and processing, providing batch and interactive job facilities. The software has to accept international standards, to seek common developments with other experiments.

A computing Grid was chosen because it provides several key benefits. In particular:

- The significant costs of maintaining and upgrading the necessary resources for such a computing challenge are more easily handled in a distributed environment, where individual institutes and participating national organizations can find local computing resources and retain responsibility for these, while still contributing to the global goal.

- Also, in a distributed system there are no single points of failure. Multiple copies of data and automatic reassigning of computational tasks to available resources ensures load balancing of resources and facilitates access to the data for all the scientists involved, independent of geographical location. Spanning all time zones also facilitates monitoring and support.

Of course, a distributed system also presents a number of significant challenges. These include ensuring adequate levels of network bandwidth between the contributing resources, maintaining coherence of software versions installed in various locations, coping with heterogeneous hardware, managing and protecting the data so that it is not lost or corrupted over the lifetime of the LHC, and providing accounting mechanisms so that different groups have fair access, based on their needs and contributions to the infrastructure. These are some of the challenges that the LCG project is addressing.

The ATLAS collaboration uses the LCG tools to produce simulation data needed to validate its computing model, software, data model and to perform simulation studies.

3.2 The ATLAS Software Framework

Computing is a major aspect of high energy physics experiments. The physical discoveries and results depend on an efficient triggering system, data acquisition, storing and effective analysis tools. Offline computing traditionally covers all processes from storing raw data up to the final analysis, as well as MonteCarlo generation, detector simulation and displaying events.

The basic goal of the ATLAS software is the creation of a framework able to host event generation, simulation, reconstruction, event filter, visualization, and, with a large flexibility, to allow the writing of analysis codes detaching the user from the typical implementation details. The official software framework is ATHENA (**AT**las realization of a **H**igh **E**nergy and **N**uclear physics data analysis **A**rchitecture) ([49]). It is a flexible object-oriented C++ based framework which represent a concrete implementation of an underlying architecture consisting of the specification of components and their interactions with each other. A component (a block of software) has a well specified interface and functionality. The main components of the ATHENA software architecture can be seen in the object diagram in the Figure 3.1. This object diagram represents a hypothetical snapshot of the system state, showing the component instances and their relationship; it does not illustrate the software structure.

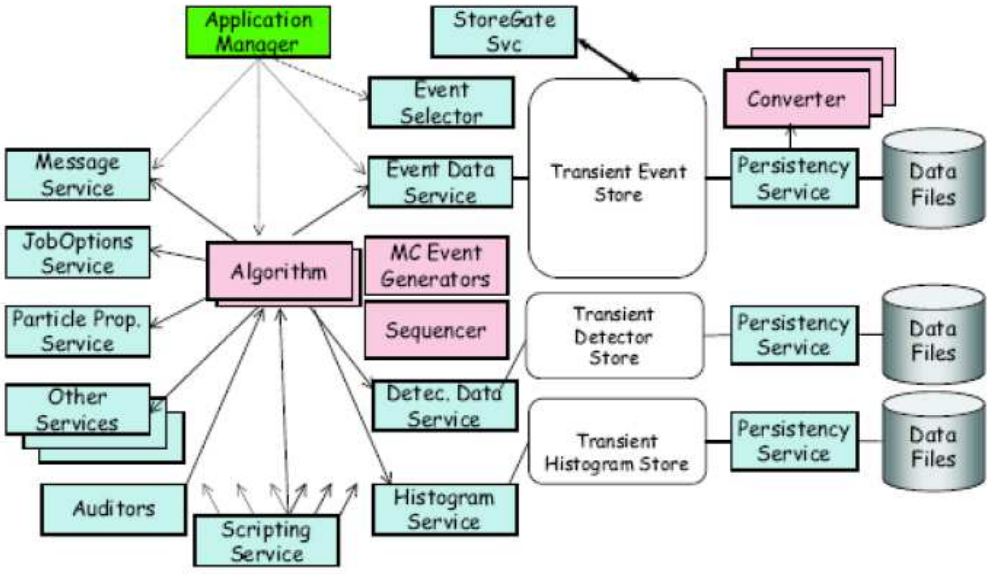

Figure 3.1: *ATHENA architecture object diagram.*

The framework provides basic services like I/O, histogramming, an event loop manager and allows to hook user algorithms in a flexible way. An ATHENA job is configured by so-called jobOption files that are written in the Python scripting language. These jobOptions define what modules have to be executed and allow to pass parameters to these modules. ATHENA will be also used in the ATLAS trigger system. Dedicated multi-threaded versions

of ATHENA are running Second Level Trigger and the Event Filter to provide fast reconstruction and monitoring.

The main components of ATHENA are:

Algorithms are typically used to process event data. They have an *initialize* and a *finalize* method that are executed at the beginning and at the end of a job, and an *execute* method that is executed for each event.

Services provide specific framework capabilities and, as their name implies, provide a service to their client. They are setup and initialized at the beginning of the job and are used by algorithms.

AlgTools are used for code that is shared between different algorithms. Like algorithms they have *initialize* and *finalize* methods but not *execute* method.

Data Objects Data object in ATHENA are objects in the sense of object-oriented programming, instances of C++ classes. They are what is moved between Algorithms, acting as their input and output.

Stores In ATHENA, data object are kept in Stores. In order to reduce the coupling between Algorithms, several so-called Transient Data Store (TDS) are available. They act as the temporary repository for informations. An algorithmic module creates a Data Object and post it to the TDS to allow other modules to access it. Once an object is located onto the store, the TDS takes the ownership of it and manages its lifetime. The coupling between TDS and the framework is the StoreGate service, that is basically a component which manages the memory of the instance of the Data Object. The different transient stores have different lifetime policies associated with them, particular stores being: the Event Data Store or Transient Event Store, the Detector Data Store, the Histogram Store.

Converters convert data between a transient and a persistent representation. For instance, the raw data is read in the byte stream converter and histograms are written by the histogram converter.

3.3 Data Challenges

In 2002 the production of a series of Data Challenges (DC's) was started, whose goals are the validation of the Computing Model, of the complete software suite, of the data model, and to ensure the correctness of the technical choices to be made.

The ATLAS Community is using DC's data also to prepare the analysis at LHC, leading to the validation of the software.

Four Data Challenges ([50],[51]) have been planned before the data taking: DC0, DC1, DC2 and DC3.

Data Challenge 0 (DC0) has been completed in March 2002 and it was used to test the continuity of the code chain. The aim was primarily to check the state of readiness for Data Challenge 1. Only modest sample were generated of "$Z + jets$" events or similar. In addition few samples of single particle data (electrons, muons, photons) were generated. They are finalized to study of the impact of the new detector layout. In parallel some of the existing TDR Data generated in 1997-1998 was converted and was run in new software framework.

Data Challenge 1 (DC1) production has been completed in December 2003. In the first phase the infrastructure was put in place and the tools to produce the bulk of simulated data required by the High Level Trigger studies for the Technical Design Report. In this phase, 10 million of physics events and 40 million of single particle events for a total of 30 TBytes were produced. In the second phase, about 34 TBytes of pile-up data were produced. In the third phase a large fraction of these data has been reconstructed.

Data Challenge 2 (DC2) production has begun in July 2004. For this production it was mandatory to use Grid systems. There was many changes respect to DC1. New versions of generator codes have been used. The detector simulation has been translated from a FORTRAN GEANT3 simulation code to a object-oriented GEANT4 simulation. The digitization is rewritten in ATHENA framework. The reconstruction is improved but without radical changes, it is more modular and a rearrangement of some algorithms has been performed.

Data Challenge 3 (DC3) foresees the production of about 10^8 events and is now ongoing until the end of 2006. It is the final prototype both for software and computing infrastructure before data taking. It includes the detector layout as-built ad some aspects missing in DC2 production: trigger reconstruction and selection algorithms both for LVL2 and EF; detector misalignment simulation, detector inefficiencies.

A bulk of events, in the Data Challenge 3 production environment, has been generated, simulated, reconstructed and analyzed with the ATLAS official software using LCG Grid facilities to produce the physics results reported in this thesis about rare semileptonic beauty decays.

3.4 B-Hadron Production at the LHC

In this section an overview of the B-hadron production at LHC, as implemented in MonteCarlo programs, is given

The jet production and fragmentation model for the B-hadron production which has been developed, comprises three distinct stages:

- the time and energy of the hard collision of two protons, involving par-

tons, quarks and/or gluons, is characterized by the squared momentum transfer Q^2;

- the partons develop into multi-parton showers along the direction of the primary parton over a time period $t < Q^2$;
- the hadronization process converts partons into the observed hadrons.

3.4.1 Cross Section

The b-quark is heavy: $m_b \sim 5\ GeV$. The heavy flavour production in hadronic collision can be described in the parton model approach ([52],[53]). The colliding hadrons are composed of partons, which may be quarks or gluons, the masses of which are all on the scale $m_q \gg \Lambda$, where Λ is the QCD mass scale. The cross section is calculable as a perturbation series in the QCD running coupling constant α_s, evaluated at the mass of the heavy quark. The experimental conditions usually imply kinematics cuts on transverse momentum; these are in the vicinity of the heavy quark mass. This guarantees that the hadron interaction be harder than the essential parameters of strong forces, i.e. the QCD parameter Λ and the inverse color confinement radius, and so the application of perturbative QCD methods is justified. The inclusive production of heavy quarks in a high energy hadron collision occurs via $A + B \rightarrow Q + X$, where A and B represent the two colliding hadrons and Q the produced quark. This is shown schematically in Figure 3.2.

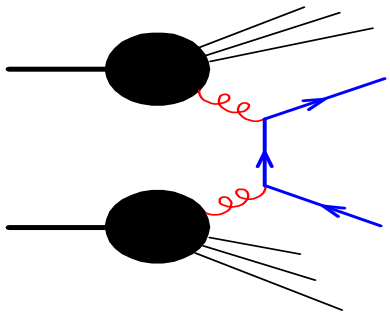

Figure 3.2: *Typical diagram for heavy quark production.*

The total cross section for the heavy quark pairs inclusive production in collisions between two hadrons, A and B, is given by

$$\sigma_{q\bar{q}}(S) = \sum_{i,j} \int dx_1 dx_2\ \hat{\sigma}_{ij}(x_1 x_2 S, m_R^2, \mu_R^2)\ F_i^A(x_1, \mu_F)\ F_j^B(x_2, \mu_F) \quad (3.4.1)$$

where:

- $x_1 x_2 S$ is the square of the partonic center of mass energy;

- μ_R and μ_F are the renormalization and factorization scales constant respectively;
- m_R is the mass of the produced heavy quark;
- $F_i^A(x_1, \mu_F)$ and $F_j^B(x_2, \mu_F)$ are the parton distribution functions;
- $\hat{\sigma}_{ij}$ is the short distance partonic cross section for the inclusive production of a heavy quark.

The renormalization scale μ_R removes the effects of physics at time scales $\Delta t \ll 1/\mu_R$ (soft processes). The effects of this small time scale physics is accounted by choosing the value of the strong coupling constant to be dependent upon the renormalization scale chosen, $\alpha_s = \alpha_s(\mu)$. The introduction of a factorization scales μ_F attends to arrange the contributions from short and long time scales such that contributions from short time scales appear as part of the hard scattering functions whereas those from long time scales appear in the parton distribution functions. Equation (3.4.1) can be interpreted as follows: $F_i^A(x_1, \mu_F)$ gives the probability of finding parton i in hadron A, $F_j^B(x_2, \mu_F)$ the probability of finding the parton j in hadron B and $\hat{\sigma}_{ij}$ the cross section that these partons produce the observed the $Q\bar{Q}$ pair.

The parton distribution functions are obtained from fits to experimental data. The distribution function $F_i^A(x_1, \mu_F)$, of parton flavour i, describes the distribution of the parton in a high momentum hadron A as a function of the fraction of the proton's momentum x, carried of by the parton, and the renormalization scale μ chosen to be of the same order as the momenta involved in the process.

The hard scattering cross section $\hat{\sigma}_{ij}$ can be calculated using perturbative QCD. $Q\bar{Q}$ pair production is a hard process, occurring at short distance scales at which quarks and gluons can be treated perturbatively. The total cross section for the inclusive production of a $Q\bar{Q}$ pair from parton i and j is given by ([54])

$$\hat{\sigma}_{ij}(s, m^2, \mu^2) \;=\; \frac{\alpha_s^2(\mu)}{m^2}\left[f_{ij}^{(0)}(\rho) + 4\pi\alpha_s\left(f_{ij}^{(1)}(\rho) \;+\; \bar{f}^{(1)}(\rho) log\frac{\mu^2}{m^2}\right)\right] \quad (3.4.2)$$

where m is the heavy quark mass, $s = x_1 x_2 S$ is the partonic center of mass energy squared, and $\rho = 4m^2/s$. The function $f_{ij}^{(0,1)}(\rho)$ describe the cross section contributions from the $q\bar{q}$ and $gluon - gluon$ subprocesses. They are evaluated as a perturbation series in order of $\alpha_s(\mu^2)$. The lowest order terms are processes of order α_s^2 (Leading Order, LO) due to quark-antiquark annihilation and gluon-gluon fusion as showed in Figure 3.3. Higher order, Next to Leading Order (NLO) correction of order α_s^3 describe the processes showed in Figure 3.4, which include radiative correction to the leading order processes and introduce the quark gluon scattering not present at leading order ([55],[34]). The current study include these higher order QCD processes.

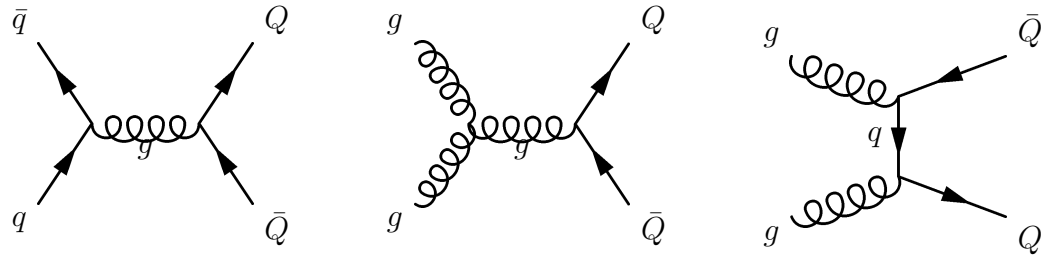

Figure 3.3: *Lowest order diagrams for heavy quark production.*

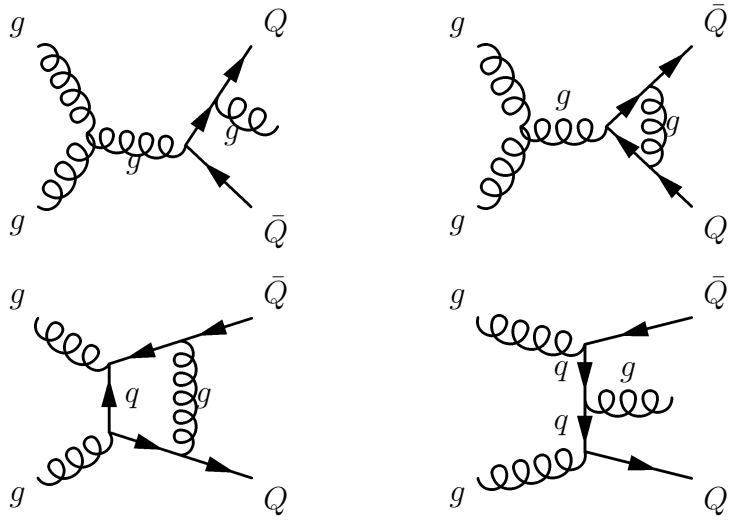

Figure 3.4: *NLO diagrams for heavy quark production.*

3.4.2 Hadronization

The partons produced in the hard scattering processes will form the final hadrons. The hadronization describes this process through the quark fragmentation. Perturbative QCD cannot be used due to the large distance between the partons, where the quark-quark interaction become strong.

Various model have been developed which attempt to describe the process of hadronization. The Lund string fragmentation model ([56]) has been used for this study.

In the string model, confinement is implemented by spanning strings between the outgoing partons. These strings correspond to a Lorentz-invariant description of a linear confinement potential with string tension $k \approx 1\,GeV/fm$. Each string piece has a color charge at one end and its anticolour at the other. The double color charge of the gluon corresponds to it being attached to two string pieces, while a quark is only attached to one. A diquark is considered as being in a color antitriplet representation, and thus behaves like an antiquark. Then each string contains a colour triplet endpoint, a number of intermediate gluons and a color antitriplet end. Consider e.g. the LO process $gg \rightarrow b\bar{b}$ where two distinct color topologies are possible. Representing the proton remnant by a u quark an a ud diquark (or alternatively d plus uu), one possibility is to have the strings $b - ud$, $\bar{b} - u$ and $u - ud$ (see Figure 3.5) and the other is identical except the b is instead connected to the ud diquark of the other

proton because the initial state is symmetric.

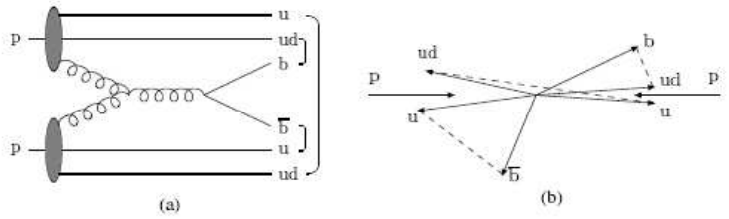

Figure 3.5: *Example of a string configuration in a pp collision. (a) Graph of the process, with brackets denoting the final color singlets. (b) Corresponding momentum space picture, with dashed lines denoting the strings.*

Once the string topology has been determined, the Lund string model can be applied to describe the non-perturbative hadronization. Depending on the invariant mass of a string, the Lund model distinguishes the following three hadronization mechanisms:

Normal string fragmentation If each string has a large invariant mass, then the standard iterative fragmentation scheme leads to an average multiplicity of hadrons produced from a string increasing logarithmically with the string mass.

Cluster decay If a string is produced with a small invariant mass (cluster) only a single two body final state is kinematically accessible. A $Q - \bar{q}$ cluster will decay into one heavy and one light hadron by the production of a light $q\bar{q}$ pair in the color force field between the two cluster endpoints.

Cluster collapse The string invariant mass is so small that the cluster cannot decay into two hadrons. It is assumed to collapse directly into a single hadron which inherits the flavour of the string endpoints.

In the ATLAS $B-$Physics simulation, the formation of hadrons containing b quarks is parametrized by the Peterson fragmentation function ([57]). Attaching a light quark $\bar{q}$ to a heavy quark Q (or a diquark qq for baryon production) decelerates the heavy quark in the fragmentation process only slightly. Thus Q and $Q\bar{q}$ or Qqq should carry almost the same energy. This behavior is described by the Peterson fragmentation function for b-quarks:

$$D_b(z) \;=\; \frac{1}{[1 - z^{-1} - e_b/(1-z)]^2} \tag{3.4.3}$$

The scaling variable z gives the fraction of the b-quark momentum which is taken by the final state B-hadron. The parameter e_b is the only free parameter. In the ATLAS simulation a value of 0.007 was used, motivated by the fact that the corresponding simulation results reproduce the b-quark production cross section at the Tevatron ([34]).

3.5 Event Generation in ATLAS

Event generation in ATLAS has been carried out in the ATHENA framework (see Section 3.2). ATHENA integrates the MonteCarlo software packages PYTHIA and EvtGen which have been used for this studies. The output for the MonteCarlo generators is placed in a persistent output file for downstream use by simulation. PYTHIA 6.203 has been used for the event generation and the hadronization steps while EvtGen for the decays of the unstable particles produced. The following subsections describe in more details the two packages.

3.5.1 Pythia MonteCarlo Event Generator

PYTHIA ([58]) is a program used for event generation in high energy physics. The emphasis is on multiparticle production in collision between elementary particles, hard collisions in e^+e^-, pp and ep colliders. The program is intended to generate complete events, in as much detail as experimentally observable ones, within the bounds of the current understanding of the underlying physics. For the description of a typical high energy event, an event generator has to contain a simulation of several physics aspects, to follow the evolution of an event. These are the main aspects of a pp collision reproduced in PYTHIA:

- Initially two beam particles are coming each towards other. Each hadron is characterized by a set of parton distributions, which defines the partonic substructure in terms of flavour composition and energy sharing.
- One shower initiator parton from each beam starts off a sequence of branchings, such as $q \rightarrow qg$, which build up an initial-state shower.
- One incoming parton from each of the two showers enters in the hard process, where a number of outgoing partons are produced: usually two. The nature of this process determines the main characteristics of the event.
- In addition to the hard process considered above, further semihard interactions may occur between the other partons of two incoming hadrons.
- When a shower initiator is taken out of a particle beam, remnant beam is left behind. This beam may have an internal structure, and a net color charge that relates it to the rest of the final state.
- The QCD confinement mechanism ensures that the outgoing quarks and gluons are not observable, but instead fragment to color neutral hadrons.
- Many of the produced hadrons are unstable and decay further.

For the beauty quark production and hadronization, PYTHIA follows the approach shown in the previous section.

PythiaB: Interface to Pythia6 for Beauty Events Generation

For the beauty event generation PythiaB ([59]) has been used. PythiaB provides an interface to PYTHIA6 allowing to:

- speed up B-events simulation.
- simulate only wanted decay channel;
- apply selection cuts organized in several levels: after parton showering, after hadronization, trigger-like cuts and offline type of cuts;
- define b-production parameters - optimal parameters are prepared as default and are tuned to beauty quark production at Tevatron ([60]).

In order to speed up simulation, PythiaB interrupts a simulation process after the parton development (just before hadronization) to check for the presence of $b\bar{b}$ quarks satisfying user's defined limits in p_T and η. The hadronization is repeated several times (MHAD times) using the same parton part of the event. The resulting cross section is then divided by the number of hadronizations. For the simulation of the wanted decay channel, PythiaB provides an interface allowing user to close and open channels without an intervention in the code.

3.5.2 EvtGen: a MonteCarlo Generator for B-Physics

EvtGen ([61]) is an event generator well suited for B-Physics, initially written for e^+e^- B-factories. EvtGen is tuned to BaBar, Belle, CLEO data and has been adopted to hadron colliders by CDF, LHCb, ATLAS and D0 experiments. It implements many detailed models that are important for the physics of B-mesons. In particular, it has detailed models for semileptonic decays, CP-violating decays and produces correct results for the angular distributions in sequential decays. The EvtGen package provides a framework in which new decays can be added as modules. These modules, which perform the simulation of the decays are called models in EvtGen. One of the novel ideas in the design of EvtGen is that spin algebra and decay amplitudes, instead of probabilities, are used for the simulation of decays, allowing interference effect, polarization, correct angular distributions, CP violation due to interference between mixing and $\Delta B = 1$ processes or between tree and higher order processes.

EvtDecay: ATLAS Interface to EvtGen

EvtGet has been used for simulation of weak decay channels in ATLAS B-Physics simulation. EvtDecay ([62]) provides an interface to EvtGen. EvtDecay can be concatenated with PythiaB algorithm in generation. At initialization EvtDecay activates re-writing of PYTHIA masses and widths of B-hadrons and charm hadrons by EvtGen. All weak B-decays are closed in PYTHIA and after PYTHIA generates an event and eventually performs

strong and electromagnetic decays, it writes the event into HepMC ([63]) transient store using StoreGate. EvtDecay then reads the HepMC event from StoreGate and sends all undecayed B-hadrons to be weakly decayed in EvtGen. New decay trees are added into the existing HepMC event in the transient store and then written into a persistent root file which serves as input for the detector simulation.

EvtGen has been used for the generation of $B^+ \to K^+\mu^+\mu^-$ and $B^+ \to K^{*+}\mu^+\mu^-$ events. A new decay model has been added to EvtGen to allow the decay description following the theoretical model described in Section 1.7.

BSignalFilter algorithm has been used to simulate the action of LVL1 and LVL2 triggers. BSignalFilter loops over all HepMC particles and test each one against the provided LVL1 criteria (particles must be a muon, kinematics as given by the user). If any one particle passes the cuts, a flag is set to indicate the LVL1 trigger has fired. If LVL1 is activated, the particles are iterated over once again to search for those triggering LVL2. If the particle is a muon, it is checked to ensure it is not the LVL1 muon. Again if any is found a flag is set. If both LVL1 and LVL2 are passed, the algorithm extracts the whole decay chain and write it into the permanent output file, if not, the whole event is rejected. After all event have been processed a summary report is printed.

Figure 3.6 shows a flow chart diagram of the production procedure for b-events in ATLAS.

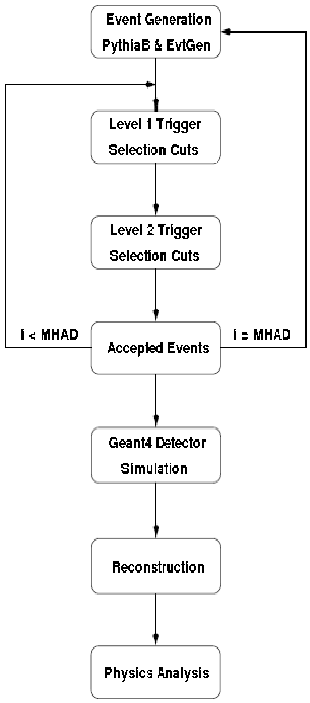

Figure 3.6: *Flow diagram of the production procedure for b-events in ATLAS.*

3.6 The ATLAS Detector Simulation

Figure 3.7 shows a simplified view of the processing stages in the simulation data flow. Input for simulation comes from event generators after a particle filtering stage. Data objects representing MonteCarlo truth information from the generators are read by simulation and processed. Hits produced by the simulation can be directly processed by the digitization algorithm and transformed into Raw Data Objects (RDOs). Alternatively they can be sent first to the pile-up algorithm and then passed to the digitization stage.

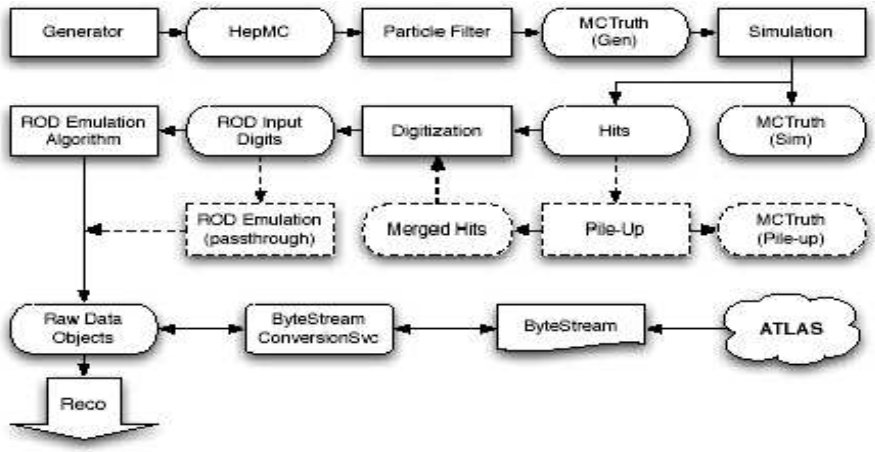

Figure 3.7: *Processing stages in the simulation data flow.*

RDOs produced by the simulation data-flow pipeline are used directly by the reconstruction processing pipeline described in Section 3.7 . Thus the simulation and reconstruction pipelines are coupled together by the RDOs which act as the output from the simulation pipeline and the input to the reconstruction pipeline. However, the ATLAS Data Acquisition system (TDAQ) produces byte-stream files and, in order to reproduce this, an optional final stage can be added to the simulation processing chain in order to generate these files from the RDO files. In this case, the initial stage in the reconstruction pipeline first converts the byte-stream information into RDO objects which are then used for subsequent reconstruction processing.

Any MonteCarlo truth information is removed in the conversion from RDOs to byte-stream format such that byte-stream files produced by the simulation pipeline are an accurate representation of the byte-stream files coming from the ATLAS TDAQ. In the context of the High-Level Trigger (HLT), the conversion from byte-stream representation to RDOs is in some cases replaced by a direct conversion to objects (PrepRawData) otherwise created by the next stage in the reconstruction pipeline, but this is a performance optimization only.

The full simulation framework is described below.

3.6.1 Full GEANT4 ATLAS Simulation

The ATLAS detector simulation programs have been heavily based on the Geant3 simulation package and infrastructure since the inception of the experiment.

With the development and implementation of the GEANT4 (G4) toolkit ([64],[65]), starting from the year 2000, ATLAS prepared for moving its simulation suite to the object-oriented paradigm. Geant3 and GEANT4 were run alongside each other for a while in order to validate the new suite against the previous one. The switch-over happened in 2003, in the early preparation phase of the second Data Challenge (DC2). Since then, GEANT4 has become the main simulation engine of ATLAS, and all new developments have been carried out in the new environment.

The GEANT4 toolkit provides both a framework and the necessary functionality for running detector simulation in particle physics and other applications. The functionalities provided include optimized solutions for geometry description and navigation through the geometry, the propagation of particles through detectors, the description of materials, the modeling of physics processes, visualization, and many more. A basic concept is that of Sensitive Detectors, which allow for the definition of active detector elements, perform corresponding actions within them, and write out hits. Development activities to make use of GEANT4 functionality within the ATLAS-specific set-up and software environment started in 2000, taking into account ATLAS-specific requirements. These provide tailored packages for handling geometry, kinematics, materials, physics, fields, sensitive detectors, run-specific issues and visualization, etc. These activities culminated in 2003 with the GEANT4 simulation being embedded in ATHENA framework. This migration to Athena was also done for the detector simulation packages which had been developed in detail in the stand-alone environment.

In general, GEANT4-based detector simulation programs ([66],[67]) are based on criteria like dynamic loading and action-on-demand, and all user-requested functionality has been added by means of plug-in modules. Since 2003, extended common functionality and new developments have been implemented only in the Athena-based version; examples are updates on physics processes (e.g. transition radiation process for TRT simulation), the implementation of MonteCarlo truth, simulation of the ATLAS combined test-beam set-up, etc. A particularly important new feature is the building of the GEANT4 geometry tree from the one implemented in the ATLAS Detector Description package GeoModel ([68]). This procedure has the clear advantage of avoiding duplication of efforts and extra work involved in maintaining and synchronizing two different detector geometry versions, one for the simulation, the other for reconstruction. Since 2001 a rather extensive physics validation program has been under way to test the physics models implemented in GEANT4, to ensure, through comparison with test-beam results where available (see for example Chapter 5 of this thesis), that GEANT4 simulation meets the expected precision targets, and to provide feedback to the GEANT4 development team.

In almost all cases comparison with experimental data from beam tests gives very good agreement.

G4ATLAS produces hits as output, which are a record of the real interactions of particles in the detector. At higher machine luminosities, however, multiple interactions can occur at each beam crossing (typically one signal event with multiple minimum-bias background events), and in addition other backgrounds (e.g. cavern background) need to be taken into account. As seen in Figure 3.7, pile-up (i.e. the overlaying of signal and background events) is an optional processing stage in the simulation processing pipeline.

3.6.2 Digitization

The hits produced either directly by GEANT4 ATLAS simulation, or from the merging of pile-up events, need to be translated into the output actually produced by the ATLAS detectors. The propagation of charges (as in the tracking detectors and the liquid argon Calorimeter) or light (as in the case of tile Calorimeter) into the active media has to be considered as well as the response of the readout electronics. Unlike the previous steps in the simulation chain, this is a very detector-specific task, and the expertise of people building and testing each of the sub-detectors is essential. The final output of the digitization step are Raw Data Objects (RDOs) that have the same format as the real detector data.

To implement the modular organization of digitization, a package is created for each of the detector subsystems and a single point of contact is available for each package. Design and operating conditions (like magnetic field or voltage) of the detectors are set using jobOption parameters or taken from the condition or detector description database. Digitization operates locally at the level of each sub-detector (e.g. a pixel module or a Calorimeter cell) and the same code can be used in the context of the full ATLAS simulation, or a test beam or any other test. It is of key importance that digitization is tuned by comparing the RDO output to real data in system tests to produce a realistic tuning of the detector response. RDOs produced by the simulation data-flow pipeline are used directly by the reconstruction processing.

3.7 Reconstruction

The ATLAS detector will produce approximately 3 *PByte* of raw data per year, a large amount of informations which prohibits the simple distribution to worldwide collaborators. To enable physicists to analyze the data at remote sites, several different types of datasets, corresponding to different stages of reconstruction, are produced. Thus the following datasets are available:

- Byte-stream Data which is a persistent presentation of the event data flowing from the HLT.
- Raw Data Object Data (RDO) which is a C++ object representation of the byte-stream information.

- Event Summary Data (ESD) ([69]) which contains the detailed output of the detector reconstruction and is produced from the raw data. It contains sufficient information to allow particle identification, track refitting, jet calibration etc. thus allowing for the rapid tuning of reconstruction algorithms and calibrations.

- Analysis Object Data (AOD)([69]) which is a summary of the reconstructed event, and contains sufficient information for common analyzes. Several tailor-made streams of AODs are foreseen for the different needs of the physics community. AODs can be produced from ESDs and thus makes it unnecessary in general to navigate back and process the raw data, adding significant cost and time benefits.

The reconstruction processing pipeline can be decomposed into several stages. Primary stages are:

- Detector and combined reconstruction (henceforth "Reconstruction"). This includes the reconstruction of the tracks and Calorimeter clusters and the first steps in particle identification. The output is stored and defines the content of the ESD.

- Analysis preparation. This step includes the reconstruction of complex objects, for example the b-tagging object JetTag, and reduces the information to an acceptable size for wide distribution. The output defines the AOD content. Furthermore the event tags are created from the AOD in an additional step.

The role of reconstruction is to derive from the stored raw data the relatively few particle parameters and auxiliary information necessary for physics analysis: photons, electrons, muons, tau-leptons, jets, missing transverse energy, primary vertex. Information from all detectors is combined so that the four-momentum reconstruction is optimal for the full momentum range, full rapidity range and any luminosity, and so that particles are identified with the least background, with the understanding that the optimum between efficiency and background rejection can be analysis-dependent. A typical reconstruction algorithm takes one or more collections as input, calls a set of modular tools, and outputs typically one collection of reconstructed objects. Common tools are shared between tracking detectors on one side (Inner Detector and Muon Spectrometer) and Calorimeters on the other side (liquid argon Electromagnetic Calorimeter, Hadronic endcap and forward Calorimeter, and tile hadronic detector). Reconstruction tools can share interfaces, for example for different types of Calorimeter cluster corrections, or track extrapolation. Abstract interfaces are used to reduce dependencies. A rich set of packages is available into the Athena framework. In the following subsections a brief description of the various aspects of the reconstruction is done. Major attention has been done to the reconstruction steps and the packages used for this work.

3.7.1 Inner Detector Tracking System Reconstruction

iPatRec is an ATHENA package that performs ATLAS Inner Detector track reconstruction ([72],[73]).

During its initialization phase, iPatRec reads a geometry database describing each module of the tracker and a simplified model of the inert support/service material. Track-finding, track-following and fitting procedures make extensive use of this database. In the initialization the magnetic field is parametrized.

Although it is possible to search for tracks starting from all of the hits in the Inner Detector, in general tracks will be looked for in roads produced from seeds. Typical seeds are electron/photon candidates from the Electromagnetic Calorimeter, jets from the Hadron Calorimeter and tracks found in the external muon detectors.

The program makes a loop over all seeds, finds all potential roads, and then resolves the ambiguities due to more than one seed per road. A list of roads is produced. A loop over the roads is made. For each road, the modules which intersect the road are obtained by using their geometrical parameters.

In the first step of event reconstruction, adjacent raw data channels are clustered, and space points are produced from these clusters. The space points are collected into seven partitions having a different distance from the beam intersection region. An eighth partition is needed to smoothly extend this model into the end-cap wheels.

The general procedure is to form track candidates using space point combinations from three different partitions, subject to criteria on maximum curvature and crude vertex region projectively. A local helix interpolation between the track-candidate space-points is used to associate the remaining hits.

Track-candidates are extrapolated into the TRT taking into account magnetic field inhomogeneities.

Extra parameters are included in the track fitting to follow multiple Coulomb scattering, and in the case of an Electromagnetic Calorimeter seed, to allow for electron bremsstrahlung. Quality cuts are made on the straw tube residuals and on the ratio of found to expected straw tubes, in order to limit high-luminosity occupancy effects.

The inner detector performances have been extensively studied in [73] using iPatRec reconstruction package. The response of the detector for single muons has been measured to obtain the track parameters resolution and quality, such as transverse impact parameter, longitudinal impact parameter and transverse momentum. The reconstruction efficiency for muons and for pions are shown as a function of p_T in Figure 3.8 and 3.9 separately for barrel region (left) and end-cap region (right).

The reconstruction efficiency for muons is a measure of the optimum single particle efficiency. Pion (and electrons) have their efficiency reduced by hadronic interactions (and bremsstrahlung). Muons have an overall efficiency of $\sim 99.5\%$ with losses due to the simulated detector inefficiency and a slight lack of hermeticity in the end-cap region. Pions efficiencies are about 5 to 10%

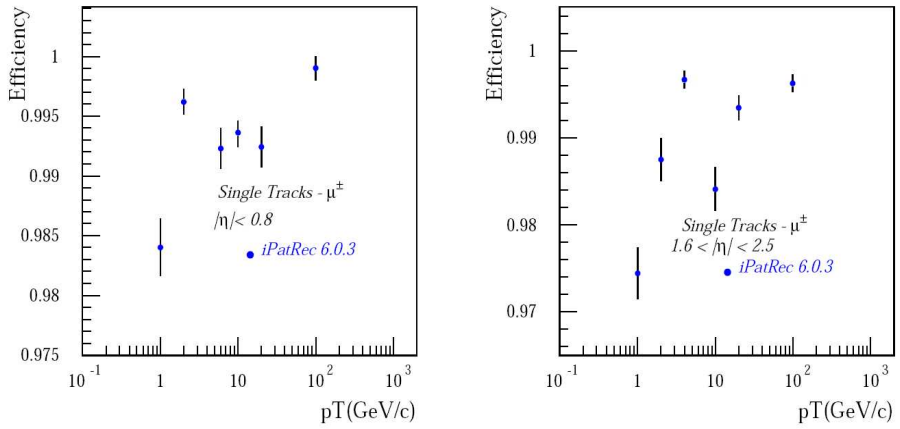

Figure 3.8: *Single muon track efficiency as a function of p_T in the barrel (left) and end-cap (right) regions.*

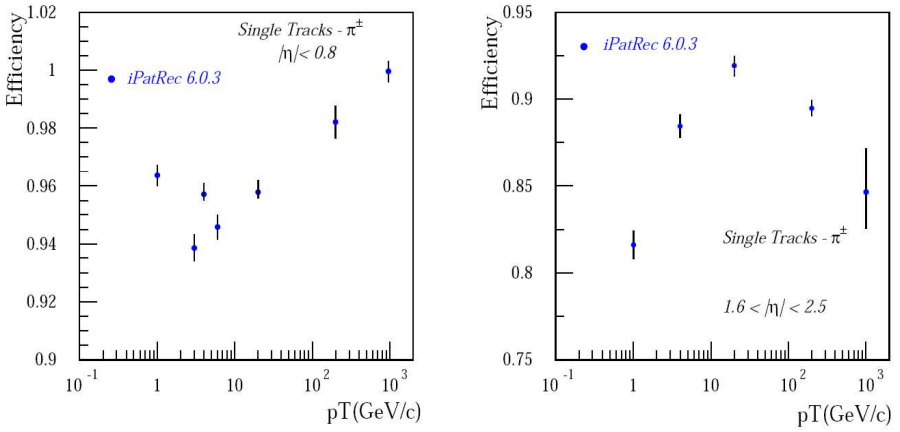

Figure 3.9: *Single pion track efficiency as a function of p_T in the barrel (left) and end-cap (right) regions.*

lower than muon efficiencies due to interactions.

3.7.2 Calorimeter Reconstruction

The Calorimeter reconstruction ([74]) algorithm collect the digit of a given calorimetric cell and convert the signal into energy. Calibration constant are applied, the total energy in the cell, the mean time of the energy deposition, and the quality of the measurement are computed. Outputs of the Calorimeter reconstruction are objects derived from the class `CaloCellContainer`, available to the other reconstruction algorithms in the Transient Event Store. The energy deposited in the Calorimeters around the muon track is necessary to perform isolation studies. The energy and its transverse component deposited in the cells of each Calorimeter sub-system in a cone ($\Delta R =$

$\sqrt{\Delta\phi^2 + \Delta\eta^2}$) around the reconstructed track are computed using the class `CaloCellContainer`, which contains the energy measurement in the Calorimeter cells. The reconstructed tracks of all the packages are considered. Eight cone dimensions are evaluated, from $\Delta R = 0.05$ to $\Delta R = 0.5$.

3.7.3 Muon Spectrometer Track Reconstruction

MOORE (Muon Object Oriented REconstruction) is a software package developed for track reconstruction in Muon Spectrometer in the ATHENA framework ([70]). In MOORE during the initialization phase, the magnetic field map and the information concerning the description of the detectors (both geometry and the materials) are loaded. The hit informations of the trigger chambers are used to guide the reconstruction in the precision chambers. The pattern recognition starts building the track in the $x-y$ plane using the RPC and TGC digits (contained in `RpcDigitContainer` and `TgcDigitContainer`). The bending power of the toroidal magnetic field in this plane is negligible almost everywhere in the detector, so a track can be approximated as a straight line. Starting from the RPC/TGC/CSC ϕ strips MOORE (by `MooMakePhiSegments`) builds `PhiSegments` (which are essentially vector of digits measuring ϕ-coordinate). A ϕ-histogram is filled with all the measured coordinates. Measurements from a muon track populate the same ϕ-bin, so a `PhiSegment` is built by collecting digits from a bin which has a number of entries above a defined threshold.

Tracks which cross the Muon Spectrometer bend on the $R-z$ plane. In this plane it is not possible to apply a histogramming method to the whole detector. Nevertheless, locally in every detector module (MDT or CSC) a crude pattern recognition is applied assuming tracks to be straight lines. For an example, with MDT's hits a histogram is filled with the ϑ-coordinate of the fired tube centers in an event.Digits, belonging to bins with number of entries above a given threshold, are grouped into a "crude" `RZ-segment`. These segments are expected to be refined by the later phases of the pattern recognition (by `MooMakeCrudeRZSegments`).

The next step in the pattern recognition is the reconstruction of the tracks in the Spectrometer stations. `MooMakeRoads` performs the pattern recognition process, for each `PhiSegment` and for each crude `RZ-segment` which is in the vicinity of the chambers producing the `PhiSegment`. `MooMdtDigitToHitSvc` converts time measurement into a drift distance applying corrections for the propagation time along the wire, the time of flight and the Lorentz angle. `MooMdtSegmentMaker` contains the algorithm to perform pattern recognition locally in one MDT module. For each pair of MDT circles (one in each multilayer), the four tangential lines are found. For each straight line, residuals of the others drift circles are computed, the straight line with the larger number of hits with residuals lower than a fixed threshold is selected. The straight line is defined "fine" `RZ-segment` only if the χ^2 is below a cut selected by the user. `RZSegmentCombinationMaker` combines the MDT segments. Two segments are combined if their directions are close. After combinations, the

hits forming the `PhiSegment` under investigation, and those forming the fine `RZ-segment` are combined to a road, which is a `MooiPatTrack`. If a road contains hits from at least two muon stations it is fitted with `MooiPatFitter` and is accepted if the fit is successful.[1] The last phase of the pattern recognition and reconstruction procedure is performed by the algorithm `MooMakeTracks`, which produces the final reconstruction tracks to be used for analysis. The parameters of the tracks produced by MOORE are expressed at the entry of Muon Spectrometer. `MooMakeTracks` loops over all the roads, produced at the previous stage by `MooMakeRoads`, and, by following a procedure very similar to `MooMakeRoads`, assigns to each road the hits from stations without trigger chambers. After having assigned hits from all the muon stations and having fitted the track, an algorithm is applied in order to allocate scattering centers along each track, thus allowing the track fit to take into account energy loss and Coulomb scattering effects. In the last step, hits with high residuals, if any, are rejected from the track. The rejection of the hits contributing to the χ^2 above a given threshold allows to purge the track of hits that are either incorrectly assigned in the pattern recognition procedure, or are affected by a large uncertainty in the measured drift distance, leading to a spoiled local spatial resolution.

MOORE has been used in this work also to analyze the data collected during the 2004 Muon Test Beam in the H8 area. The results are shown in Chapter 5. A specific ATHENA package, `MuonTestBeam`, exists to process the test beam data with MOORE. The package consists of a conversion service to decode H8 data format, of a set of services providing access to condition data base (e.g. electronic mapping, calibrations, etc.), and of a set of algorithms for the data analysis, including the possibility of filling ROOT[2] trees.

3.7.4 Combined Reconstruction

The combined reconstruction step combines information from the different detectors in an optimal way.

Photon/Electron Identification

Electron reconstruction is performed in two ways. High p_T electrons are searched for by associating tracks to sliding-window clusters, and computing shower-shape variables, track-to-cluster association variables, and TR hits variables. Dedicated track-fitting procedures for electrons are being developed. High-p_T photons are identified in a similar way, with the main difference being that a track veto is performed, except for reconstructed conversions.

[1] A road containing hits from only one station is accepted without fitting it. One-station roads are merged if near in ϕ and ϑ, otherwise the two one-station roads are kept for further processing.

[2] ROOT is an object-oriented data analysis framework developed at CERN ([71]).

Soft-electron reconstruction proceeds by extrapolating a charged track to the Calorimeter, and building a cluster around the charged-track impact point. This procedure has a better efficiency for electrons with p_T less than 10 GeV, and for electrons inside jets, which is pertinent for b-tagging.

Muon Identification

Muon measurement and identification is optimized according to the p_T regimes. High-p_T muons ($>$ 100 GeV) are measured by extrapolating the Muon Spectrometer track parameters inward through the Calorimeters and Inner Detector to the interaction point. The extrapolation of the muon trajectory to the Inner Detector track allows computation of the energy loss through the intervening material. Energy-loss parameterizations can be applied to correct the track momentum, as determined at the Muon Spectrometer entrance, to the final state muon momentum at the interaction point. Furthermore, direct measurement of energy loss (important at high p_T) can be used to correct the muon momentum.

For muons in the $6 - 100$ GeV p_T range, momentum determination is performed by both systems. The Muon Spectrometer provides a flag that uniquely identifies the muon. For momenta below 30 GeV, the measurement resolution derives mostly from the Inner Detector as the Muon Spectrometer resolution is dominated by multiple Coulomb scattering.

For p_T between 3 and 6 GeV, muons lose a large fraction of their energy in the Calorimeters, and do not cross the full Muon Spectrometer. In this case, muon tracks are found in the inner Detector and extrapolated to hit segments in the Spectrometer. Algorithms that extrapolate inner tracks and associate them with a minimal signal in the inner muon station can also be enhanced via signatures in the tile Calorimeter.

For the present work, MuonIdentification (MUID) package ([75]) has been used.

The procedure is driven by three ATHENA algorithms: `MuidInit`, `Muid StandAlone` and `MuidComb`.

`MuidInit` is just an interface between the MOORE output and MuonIdentification, it converts the MOORE tracks in `MooTrackContainer` to `MuidTracks`.

The next step is the extrapolation of tracks from the Muon Spectrometer to the vertex region, in order to have a set of track parameters comparable to those from the Inner Detector reconstruction. In this step, MUID accesses to `MuidTracks` and propagates it through the magnetic field in order to obtain the track parameters and their associated covariance matrix at the point of closest approach to the beam intersection. The multiple scattering in the Calorimeters is parametrized with a set of scattering planes; the muon energy loss is evaluated either from the Calorimeters measurements or from a parametrization as a function of η and of the muon momentum. This step allows to use MOORE plus MUID as a standalone package for the muon reconstruction. It is referred as **MuidStandAlone** algorithm. In Figure 3.10 the track reconstruction efficiency for single muons as a function on the muon p_T is shown. The efficiency

has been evaluated in the barrel region using MOORE and MuidStandAlone packages ([76]).

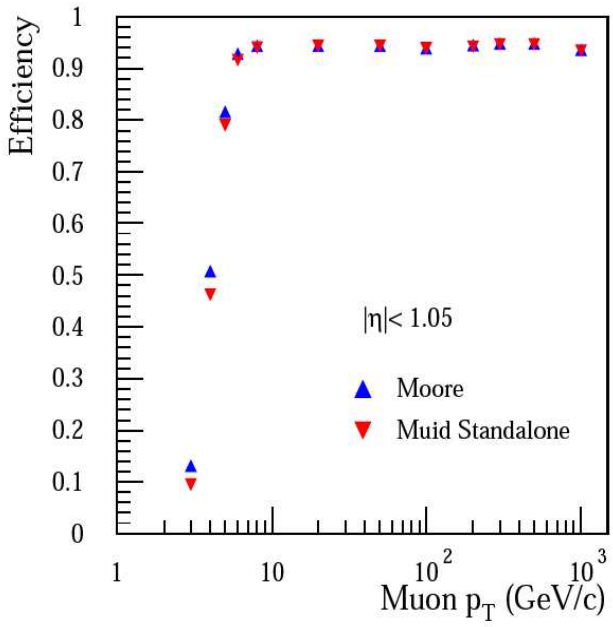

Figure 3.10: *Efficiency of single muon reconstruction as a function of the p_T obtained with MOORE and with MUID standalone. The efficiency is evaluated in the barrel region.*

In the next step, Inner Detector and Muon Spectrometer tracks are matched. A χ^2 is computed with the parameter differences and summed covariance. A combined fit is performed for all combinations with a χ^2 probability above a given cut. When no match satisfies this criterion a combined fit is attempted for the best match within a cone around the track reconstructed in the Muon Spectrometer. Tracks are combined using hits from the two subdetectors which were found and used separately by the standalone reconstruction programs. All the matches to the Inner Detector giving a satisfactory combined fit are retained as identified muons. This is the **MuidComb** method. The reconstruction performance has been tested with single muon samples in a range of transverse momentum from 3 GeV to 1 TeV. The full reconstruction chain has been executed, namely: the reconstruction in the Muon Spectrometer alone (MOORE), the track extrapolation to the vertex (MUID standalone), the reconstruction in the Inner Detector (iPatRec) and the combination of the track found in Muon Spectrometer and in the Inner Detector (MUID combined). The global efficiency and the p_T resolution as a function of p_T are shown in Figure 3.11 ([77]).

The low p_T muons, especially those from J/ψ decays, are an important signature for B-Physics. These muons lose a significant part of their energy in the Calorimeter, and thus some of them cannot be reconstructed in the Muon

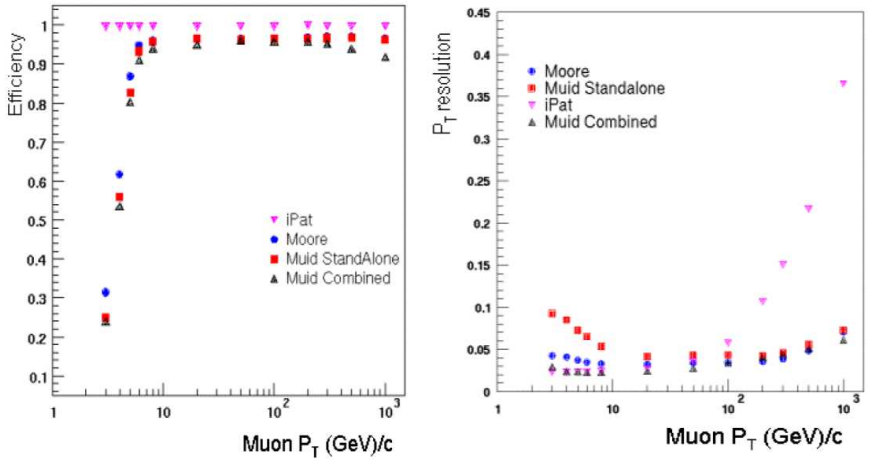

Figure 3.11: *Efficiency (left) and p_T resolution (right) as a function of p_T for MOORE, MUID standalone, iPatRec, MUID combined.*

Spectrometer. Up to 70% of J/ψ decays may be lost after passing the single muon trigger, because one of muons has low p_T and it is not reconstructed in the Muon Spectrometer. The low p_T muon identification starts after the MOORE and MUID reconstructions were performed. Inner Detector tracks are extrapolated to the Muon Spectrometer subdetectors, and there the hits of the muon subdetectors are associated with them according to their proximity in η and ϕ. Hits from the MDT inner stations, the CSC, the RPC middle stations, and TGC have to be used. Also η hits of the trigger chambers, which are not used in MOORE, are included. Then a new container is created which contains candidates that have been identified by MUID and by the above procedure. The user can ask tracks with his requirements in this new container. This method was found to be efficient and provide good purity for identifying a second low p_T muon resulting from J/ψ or rare B semileptonic decays, when one muon from the decay was reconstructed in the Muon Spectrometer. Figure 3.12 shows the muon identification efficiency of the MUID algorithm (left) as a function of muon p_T and the efficiency of the algorithm for low p_T muons identification (right). The study was performed on a signal dataset $\Lambda_b \rightarrow \Lambda J/\psi$ with $J/\psi \rightarrow \mu(p_T > 2.5\ GeV)\mu(p_T > 4\ GeV)$. The MUID algorithm identifies 30% of J/ψ (purity 52%) to be compared with the 74% (purity 39%) of the low p_T algorithm ([78]).

Tau Identification

Taus are identified in a similar way to electrons. The preliminary clustering is done with a sliding-window algorithm applied on all Calorimeters. A tau appears as a very narrow jet in the Calorimeter, associated to a small number of charged tracks. The tau reconstruction can be seeded by a Calorimeter

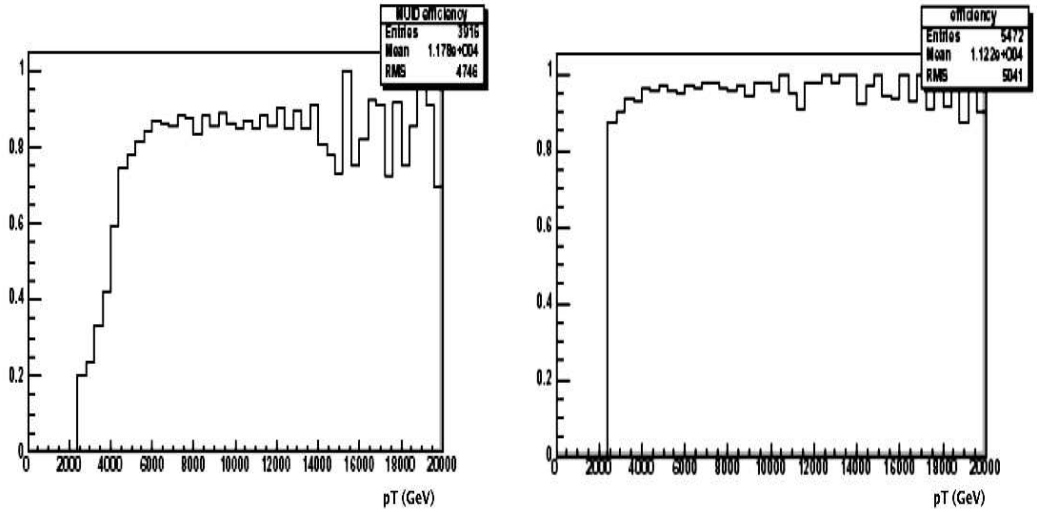

Figure 3.12: *Muon identification efficiency of the MUID algorithm (left) and low p_T algorithm (right) as a function of p_T.*

cluster or by a charged track depending on the p_T range of interest.

Tau identification is based on Calorimeter quantities such as the electromagnetic radius, the isolation in Calorimeters, the width in the strips and on quantities given by the tracker such as the number of associated tracks, the charge and the impact parameter. Likelihood and multi-variate analysis techniques are used to discriminate taus from normal jets. Taus are calibrated using the same cell-weighting scheme as jets.

Jet Reconstruction

Jets can be reconstructed from detector signals, and for MonteCarlo data, from the generated particles. The algorithms available are the seeded and the seedless cone and the k_t algorithm ([79]). The k_t implementation is provided in an external package. In the implementation there is only one jet algorithm skeleton, which can be configured externally as a sequence of tools to implement a given jet-finder strategy. This algorithm and most of the tools are designed such that they are not dependent on any specific feature of the input data objects, thus allowing their use in exactly the same way for different inputs. The only requirements on the input objects are that they implement the general four-vector and navigation interfaces. The Calorimeter system is the principal detector for jet reconstruction. The typically large number of CaloCell objects in an event prohibits using these directly as input to the jet finding, especially in the case of the k_t algorithm. The input multiplicity to the jet finding can be reduced by the Calorimeter reconstruction, where cells are grouped into CaloTower and CaloCluster objects. The CaloTower objects represent a tower of cells on a fixed grid in pseudo-rapidity and azimuth, typically with a bin size of $\Delta\phi \times \Delta\eta = 0.1 \times 0.1$ for input to the jet

finding. CaloCluster objects, on the other hand, represent groups of cells with correlated signals with their location depending only on the cell signals and locations. Both CaloTower and CaloCluster implement the four-momentum and navigation interfaces, as required by the jet algorithms. All jet algorithms combine the input object into a Jet object following their specific strategies. The total jet kinematics is represented by a four-vector, which is updated when constituents are added or removed. This four-momentum recombination requires all constituents to have meaningful four-vectors themselves, especially a positive signal amplitude (energy). On the other hand, CaloTower objects can have negative signals, indicating a major noise contribution from the cells in this tower. These negative-signal towers are combined with neighboring towers until the newly created combined tower has a small positive signal, thus canceling the negative signals before applying the actual jet finder.

Calorimeter jets can be calibrated in various ways. The standard calibration for jets from towers is based on a cell-signal weighting scheme, where weights are applied to the signal contribution from each cell. These weights have been computed such that the response to jets is flat over a large energy range, and using the constraint of an optimized energy resolution. Other approaches apply weights to Calorimeter-sampling layer sums in jets, for example.

Missing E_T Reconstruction

Missing E_T is reconstructed from the energy deposed in all Calorimeter cells and from the reconstructed muons. A correction is applied for the energy lost in the cryostat between the Electromagnetic and Hadronic Calorimeters. The Calorimeter cell energy is weighted using the same H1-style weights, depending on cell energy density (E/V) and on the Calorimeter region, used for jets. For muons the reconstructed energy from the muon chambers only is used, to avoid double energy-counting in the Calorimeters. The correction for the energy lost in the cryostat is calculated from the energy deposited in the cryostat by jets. To suppress the effect of noise in Calorimeters, a cell energy threshold in terms of number of sigma noise is applied. Missing E_T can alternatively be reconstructed from the energy measured in the topologically clustered Calorimeter cells. In this case the noise suppression is given by the thresholds applied in the topological clustering reconstruction.

Chapter 4

$B^+ \to K^{(*)+}\mu^+\mu^-$ decay channels: analysis and results

The analysis results on $B^+ \to K^{(*)+}\mu^+\mu^-$ decay simulated data are presented. In particular the signal reconstruction and characterization, the background rejection, the expected event estimation, and the ATLAS sensitivity to branching ratio measurements are discussed in great detail.

4.1 Signal Reconstruction

4.1.1 Data Samples

The theoretical model for the description of the $B^+ \to K^{(*)+}\mu^+\mu^-$ decays used in MonteCarlo generators follows the approach in Chapter 1. In particular the vector meson K^{*+}, has been considered decaying into $K_s^0 + \pi^+$ with K_s^0 decaying into two charged pions. K^{*+} decays containing π^0 ($K^{*+} \to K^+\pi^0$ and $K^{*+} \to K_s^0 + \pi^+$ with $K_s^0 \to \pi^0\pi^0$) cannot be used because the reconstruction efficiency of π^0 is very low and the background very high. It does not appear possible to reach an acceptable signal-to-background ratio for final states involving a π^0. Table 4.1 summarize the current branching ratio measurements for the two generated decay channels ([6],[30]).

Decay	$\mathcal{BR}$
$B \to K^+\mu^+\mu^-$	$(0.34^{+0.19}_{-0.14}) \times 10^{-6}$
$B \to K^{*+}\mu^+\mu^-$	$(0.97^{+0.94}_{-0.69}) \times 10^{-6}$
$K^{*+} \to K_s^0 + \pi^+$	0.66 ± 0.01
$K_s^0 \to \pi^+\pi^-$	0.6920 ± 0.0005

Table 4.1: *Branching ratios for $B^+ \to K^{(*)+}\mu^+\mu^-$ decays.*

The software machinery for the generation, simulation-digitization and reconstruction of the data has been illustrated in Chapter 3. Two data samples have been fully simulated and reconstructed. The LVL1 trigger cuts on muons

($p_T(\mu_1) > 6\ GeV$, $p_T(\mu_2) > 4\ GeV$ and $|\eta(\mu_1, \mu_2)| < 2.5$) have been applied at the generation level (see Section 2.8 and Section 3.5.1). All numbers used to compute the signal yields are summarized in Table 4.2.

Quantity	Symbol	Value
Nominal luminosity	$\mathcal{L}$	$10^{33}\ cm^{-2}s^{-1}$
Standard year	t	$10^7\ s$
Annual integrated luminosity	$\mathcal{L} \cdot t$	$10\ fb^{-1}$
$b\bar{b}$ cross section	$\sigma_{b\bar{b}}$	$0.5\ mb$
LVL1 trigger fraction	T	0.01
Probability of $\bar{b} \to B^+$	P	0.39
Symmetry factor	S	2
$\mathcal{BR}(B \to K^+\mu^+\mu^-)$	$\mathcal{BR}_1$	0.34×10^{-6}
$\mathcal{BR}(B \to K^{*+}\mu^+\mu^-,\ K^{*+} \to K^0_s + \pi^+,$ $K^0_s \to \pi^+\pi^-)$	$\mathcal{BR}_2$	0.44×10^{-6}

Table 4.2: *Relevant assumption for the calculation of the signal yields.*

The standard year of running has been assumed $10^7\ s$ at an average luminosity of $\mathcal{L} = 10^{33}\ cm^{-2}s^{-1}$ which corresponds to an integrated luminosity of $10\ fb^{-1}$. The $b\bar{b}$ cross section is considered as an initial assumption which will be revisited after the start of the LHC. The $0.5\ mb$ value ([55]) is a renormalization constant and is thus not affected by errors. The hadronization fraction of the b-quark is taken from the PDG ([6]) and the fraction of events satisfying the LVL1 trigger cuts from the PythiaB output. The symmetry factor take into account the charge conjugate decays.

The number of triggerable (and hence reconstructible) events expected in 3 years of LHC operation at $\mathcal{L} = 10^{33}\ cm^{-2}s^{-1}$ ($30\ fb^{-1}$ integrated luminosity) has been found ~ 40000 and ~ 51000 for $B \to K^+\mu^+\mu^-$ and $B \to K^{*+}\mu^+\mu^-$ respectively, and it has been calculated as

$$N_i = \mathcal{L} \cdot t \cdot T \cdot S \cdot \sigma_{b\bar{b}} \cdot P \cdot \mathcal{BR}_i \tag{4.1.1}$$

Table 4.3 summarize the number of simulated events and the number of events expected in $30\ fb^{-1}$ integrated luminosity after LVL1 trigger cuts for each decay channel.

A C++ code has been written in the ATHENA framework (see Section 3.2) for both the decay channels, in order to analyze the AOD reconstruction files ([80]).

4.1.2 Selection Strategy

The key signature of $B \to \mu\mu K$ events is the presence of the opposite charge muon pair. Due to long B lifetime, this dimuon pair is likely to form a secondary vertex which is detached from the primary vertex. The identification

Decay	Triggerable events in 30 fb^{-1}	Simulated events
$B \to K^+\mu^+\mu^-$	∼40000	30000
$B \to K^{*+}\mu^+\mu^-$	∼51000	50000

Table 4.3: *Summary table for the $B^+ \to K^+\mu^+\mu^-$ and $B^+ \to K^{*+}\mu^+\mu^-$ (followed by $K^{*+} \to K^0_s\pi^+, K^0_s \to \pi^+\pi^-$) decays. From left, columns contain the decay channel, the number of expected events after LVL1 trigger cuts in 30 fb^{-1} and the number of simulated events.*

of this vertex, if particularly close to the interaction point, requires leptons which are well reconstructed.

The event selection is done in the following order:

- primary vertex reconstruction; if more than one primary vertex has been reconstructed in the same event, only the one closer to $(0, 0, 0)$ is taken into account.
- muon and dimuon selection;
- kaon reconstruction and selection;
- B-meson reconstruction and selection.

Thus the selection has to rely on topological variables as vertex quality and vertex separation requirements. The vertex fitting routine used for this analysis is the CDF vertex fit routine ([81]).

Common requirements for the two decay channels are explained in the following.

- The primary vertex reconstruction is done automatically from the offline reconstruction program.
- The muon track candidates must fulfill the selection criteria of the muon identification MUID algorithm described in detail in Section 3.7.4.
- The charged track selection for kaon reconstruction is done inside the Inner Detector: the p_T of the track must be above 0.5 GeV and the pseudorapidity $|\eta| < 2.5$. ATLAS cannot identify pions and kaons, therefore all charged particles in the Inner Detector, not identified as muons or electrons, are taken into account.
- Dimuons are formed by two opposite charge muon tracks satisfying the LVL1 trigger ($p_T(\mu_1) > 6$ GeV, $p_T(\mu_2) > 4$ GeV and $|\eta(\mu_1, \mu_2)| < 2.5$) request. They must fulfill the following requirements:
  - the dimuon vertex momentum must not point to primary vertex;
  - the dimuon vertex χ^2/NDF must be lower than 10;

- the dimuon invariant mass must be in the kinematic allowed window: $2m_\mu < m_{\mu\mu} < m_{B^+} - m_{K^+}$ and $2m_\mu < m_{\mu\mu} < m_{B^+} - m_{K^{*+}}$ respectively for the two decay channels.

4.1.3 $B^+ \to K^+\mu^+\mu^-$

The $B^+ \to K^+\mu^+\mu^-$ decay is topologically very simple. After the dimuon selection, a positive charge particle is then searched in the Inner Detector satisfying the charged track selection criteria. For each found dimuon, B^+ candidates are formed using preselected positive charge track. The following final selection criteria are required for the B^+ meson reconstruction:

- the B^+ system must be made of one dimuon and one positive charge track;
- the B^+ vertex χ^2/NDF must be lower than 5;
- the B^+ mass must be in a $\pm 3\sigma$ window around PDG value;
- the B^+ proper time larger than 0.5 ps;
- if more than one B^+ has been reconstructed in the same event, only the one with better χ^2/NDF is taken into account.

The B^+ mass and the B^+ proper time resolution distributions of these accepted events (respectively without cut on B^+ mass and proper time) are shown in Figure 4.1.

The width of the Gaussian fit for the mass distribution is $\sigma = 42\ MeV$ and 80 fs for the proper time distribution. The B^+ candidate requirements are based on the knowledge of these value.

The most interesting distributions for the rare decay channel are the dimuon invariant mass spectrum and the forward-backward asymmetry. Experimentally the FBA is defined as ([82])

$$A_{FB} = \frac{N_F[s_1, s_2] - N_B[s_1, s_2]}{N_F[s_1, s_2] + N_B[s_1, s_2]} \tag{4.1.2}$$

where $N_F[s_1, s_2]$ and $N_B[s_1, s_2]$ are the number of positive muons (including the background ones) moving in the forward and backward directions of the B-meson, respectively, in the range of the squared dimuon mass $s\epsilon[s_1, s_2]$.

These two distributions are shown in Figure 4.2 for true events and reconstructed events. The LVL1 trigger and the analysis cuts do not brought significant changes.

4.1.4 $B^+ \to K^{*+}\mu^+\mu^-$

The $B^+ \to K^{*+}\mu^+\mu^-$ ($K^{*+} \to K^0_s + \pi^+$, $K^0_s \to \pi^+\pi^-$) decay require a more complex analysis strategy with respect to the $B^+ \to K^+\mu^+\mu^-$ channel due to the reconstruction of the two intermediate particles, K^{*+} and K^0_s.

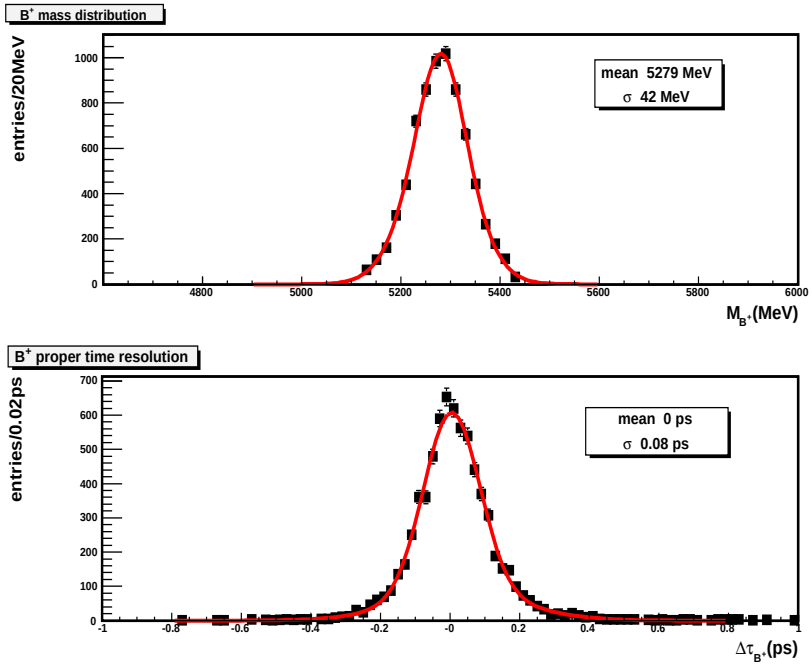

Figure 4.1: *B^+ mass and proper time resolution distributions: the mean value and the width of the distribution, resulting from a Gaussian fit, are shown.*

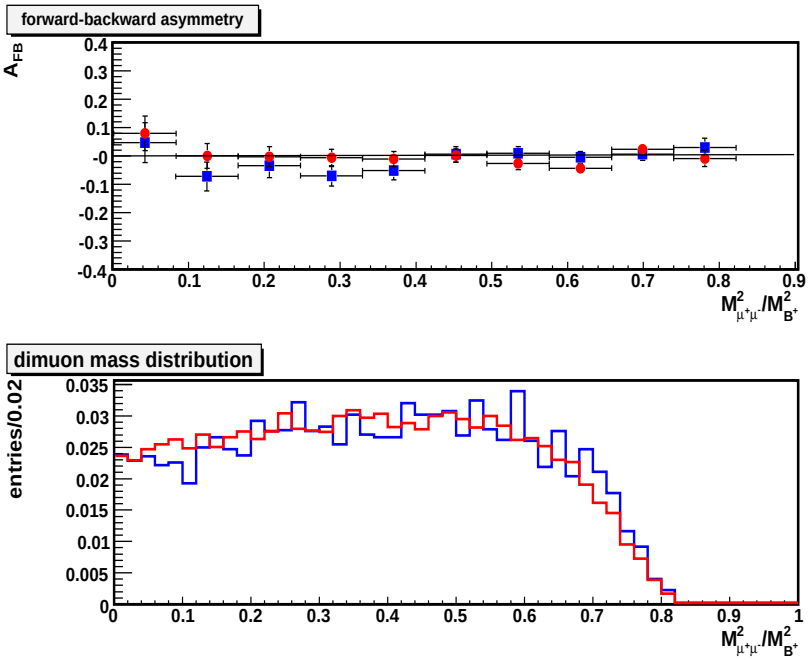

Figure 4.2: *$B^+ \to K^+\mu^+\mu^-$ normalized dimuon invariant mass and differential FBA distributions for true (red) and reconstructed (blue) events. The horizontal bars in FBA differential distribution represent the dimuon invariant mass bins and the vertical error bars are the statistical errors on FBA.*

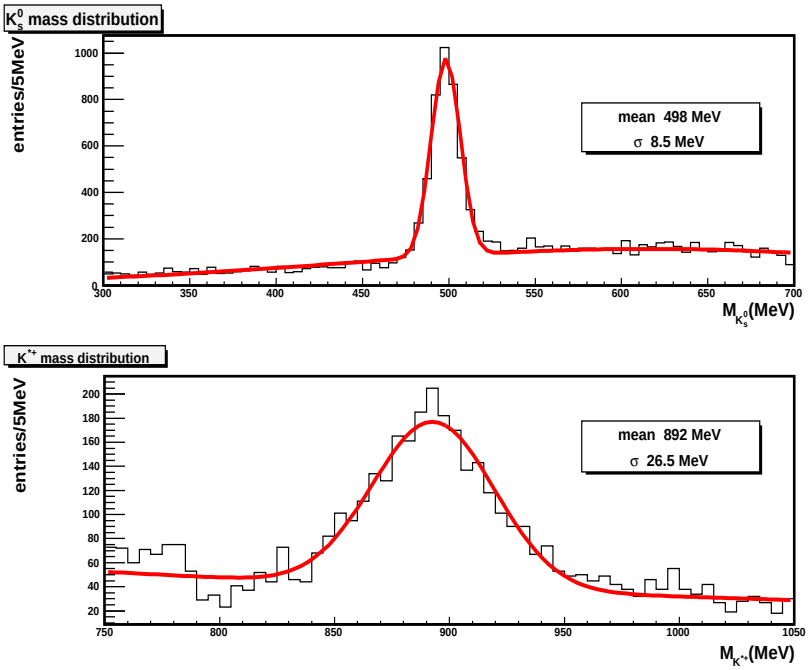

Figure 4.3: *Mass distribution for K^0_s and K^{*+} reconstruction: the mean value and the width of the distribution, resulting from a Gaussian fit, are shown.*

To reconstruct the K^0_s two opposite charge hadronic tracks are searched in the Inner Detector to be passed at the vertex fit routine. The K^0_s candidates have to fulfill the following requirements:

- the K^0_s momentum have to point to the dimuon vertex;
- the reconstructed K^0_s mass must be in a 3σ mass window around the PDG value;
- the K^0_s vertex χ^2/NDF lower than 10.

The K^0_s mass distribution of events passing these selection criteria (without mass cut) is shown in Figure 4.3 (top). A Gaussian fit leads to a sigma of 8.5 MeV.

The K^0_s with a third positive charge track coming from dimuon vertex have to form the K^{*+}. The K^{*+} candidates must fulfill the following requirements:

- the K^{*+} vertex χ^2/NDF lower than 5;
- the reconstructed K^{*+} mass must be in a 3σ mass window around the PDG value.

The K^{*+} mass distribution of events passing these selection criteria (without mass cut) is shown in Figure 4.3 (bottom). A Gaussian fit leads to a sigma of 26.5 MeV.

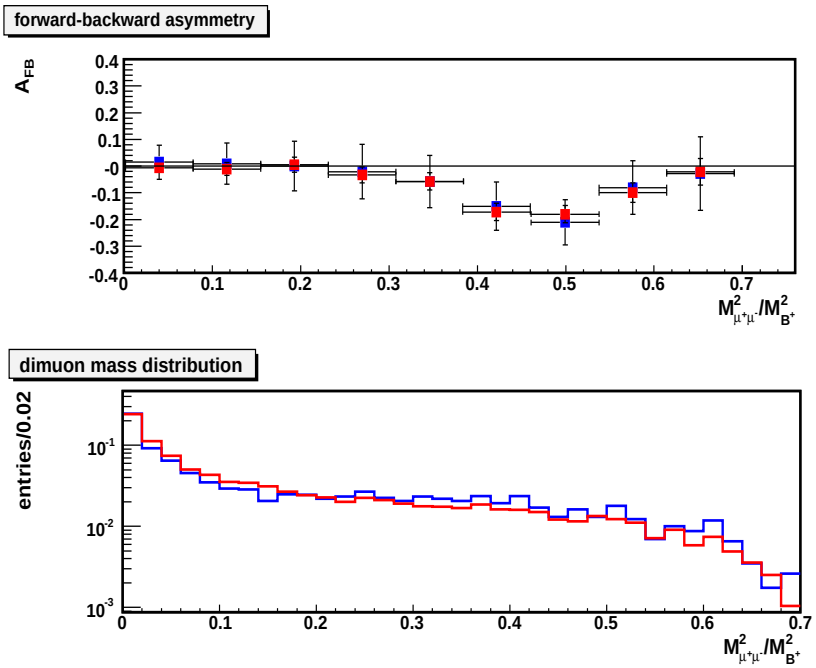

Figure 4.4: $B^+ \to K^{*+}\mu^+\mu^-$ *normalized dimuon invariant mass and differential FBA distributions for true (red) and reconstructed (blue) events. The horizontal bars in FBA differential distribution represent the dimuon invariant mass bins and the vertical error bars are the statistical errors on FBA.*

For every dimuon, B candidates are formed using preselected kaons. The final selection criteria required for B^+ are the same as those in Subsection 4.1.3. For this decay the B^+ mass width has been found to be 44 MeV.

The dimuon invariant mass and the FBA distributions are shown in Figure 4.4 both for true data and reconstructed ones. The LVL1 trigger and the reconstruction analysis cuts do not change these two distributions.

4.2 Background Sources

All events containing two muons are a potential source of background for rare dimuonic beauty decays. Of course, the most dangerous are muons originating from B-decays, as they have the same p_T and the same impact parameter spectrum as muons from rare decays.

The most dangerous background sources have been found to be the following ([83]):

- $B \to \psi X$ decays followed by $\psi \to \mu^+\mu^-$ have the same topology but fixed dimuon masses. These decays can occur at tree level or they are driven by the decay of the Z, W boson or γ in the box and penguin diagrams into a resonant $c\bar{c}$ pair. Their branching ratio is about 10^2 times larger than the branching ratio of rare decays. Only a cut in dimuon invariant mass can

remove this background source.$\psi \to \mu^+\mu^-\gamma$ decays are a second order correction to the $\psi \to \mu^+\mu^-$ decays, but they can move out the muons from the ψ window and therefore they have to be take into account as possible background source.

- The $b \to \mu^-\bar{\nu}_\mu c(c \to \mu^+\nu_\mu q)$ semileptonic decay chain, like $B^+ \to \bar{D}^0\mu^+\nu_\mu$ followed by the decay $\bar{D}^0 \to K^+\mu^-\bar{\nu}_\mu$. The two muons seem to come from the same vertex when D does not have a long proper time or when the muon is emitted in the D direction. If the missed mass due to neutrinos is not large, these decays are a very dangerous background source. Vertex requirements and cuts around B-meson mass are the basic tools to reduce this background.

- $b \to \mu\nu_\mu X$ semileptonic decays of both b and $\bar{b}$ quarks. These events have a lower probability than the previous ones to represent a background source as the two muons are not correlated in position.

Table 4.4 summarize the different background sources. Also their branching ratios have been reported.

Other rare semileptonic decays driven by $b \to s\mu^+\mu^-$ transition can be in principle background sources for $B^+ \to K^{(*)+}\mu^+\mu^-$ decays. Their branching ratio is of the same order of magnitude as the two signal channels and their contribute to background is very poor. Same argumentation for the rare decays given by $b \to d\mu^+\mu^-$ transitions: due to CKM matrix element V_{td} the branching ratios of these channels are approximately 10 times smaller than $\mathcal{B}(B^+ \to K^{(*)+}\mu^+\mu^-)$.

Decay	$\mathcal{BR}$
$B \to J/\psi X$ $(J/\psi \to \mu\mu\ (\gamma))$	1.16% (5.88%)
$B \to \psi(2S)X$ $(\psi(2S) \to \mu\mu\ (\gamma))$	4.8×10^{-3} (7.3×10^{-3})
$b \to \mu^-\bar{\nu}_\mu c$ $(c \to \mu^+\nu_\mu q)$	$\sim 1\%$
$b(\bar{b}) \to \mu\nu_\mu X$	$\sim 1.1\%$

Table 4.4: *Background sources for $B^+ \to K^{(*)+}\mu^+\mu^-$ decays and their branching ratios.*

4.2.1 Background Data Samples

The $B \to \psi X$ $(\psi \to \mu\mu\ (\gamma))$, $b \to \mu^-\bar{\nu}_\mu c$ $(c \to \mu^+\nu_\mu q)$ and $b(\bar{b}) \to \mu\nu_\mu X$ decays have been generated together in a so-called $b\bar{b} \to \mu(6GeV)\mu(4GeV)X$ samples. All b and $\bar{b}$ decay channels are left open and accessible in Pythia, but only events containing two muons satisfying the LVL1 trigger cuts are written into a permanent output file. Of course, also rare decays are contained in this sample.

Two samples of $B^+ \to J/\psi\ K^+$ and $B^+ \to \psi(2S)\ K^+$ with $\psi \to \mu^+\mu^-$ events have been produced including also radiative corrections on ψ decays and LVL1 cuts on muons, in order to evaluate the $c\bar{c}$ resonance width to perform cuts on dimuon invariant mass.

The background sample production is summarized Table 4.5. Also the number of expected events in 30 fb^{-1} after LVL1 trigger cuts is shown. This number for $b\bar{b} \to \mu(6GeV)\mu(4GeV)X$ events can be computed as

$$N_{b\bar{b}\to\mu(6)\mu(4)X} = \mathcal{L} \cdot t \cdot \sigma_{b\bar{b}\ trig} \tag{4.2.1}$$

where $\sigma_{b\bar{b}\ trig} = 3.6 \times 10^{-5} mb$ is the cross section of $b\bar{b}$ events have the first level trigger as the PythiaB output.

Decay	Triggerable events in 30 fb^{-1}	Simulated events
$B^+ \to J/\psi K^+\ (J/\psi \to \mu^+\mu^-)$	6.2×10^6	50000
$B^+ \to \psi(2S)K^+\ (\psi(2S) \to \mu^+\mu^-)$	8×10^5	50000
$bb \to \mu(6GeV)\mu(4GeV)X$	1.08×10^9	2.5×10^5

Table 4.5: *Background sample production with relative expected number of events in* 30 fb^{-1} *after LVL1 trigger cuts on muons.*

4.2.2 $c\bar{c}$ Resonances

The same analysis strategy for signal reconstruction described in Section 4.1.3 has been applied on $B^+ \to J/\psi K^+$ and $B^+ \to \psi(2S)K^+$ samples. The goal was to reconstruct the J/ψ and $\psi(2S)$ resonances in order to evaluate their mass width. In Figure 4.5 the J/ψ and $\psi(2S)$ mass distributions are shown.

Requiring a good dimuon vertex reconstruction ($\chi^2/NDF < 3$), a cut on dimuon invariant mass 3σ around J/ψ and $\psi(2S)$ PDG mass values allows to cut off almost all the events coming from $c\bar{c}$ resonant channels. This is of fundamental importance for the background rejection discussed in the next section.

4.3 Background Rejection

The background rejection has been performed using the same analysis code and strategy as the signal reconstruction on $b\bar{b} \to \mu(6GeV)\mu(4GeV)X$ reconstructed data samples. Cuts on the quantities already identified in the signal reconstruction step have been tuned in order to reduce background efficiency and obtain a signal/background ratio as high as possible. The following two subsections show the background rejection criteria for the two decays. Cuts are applied consequently.

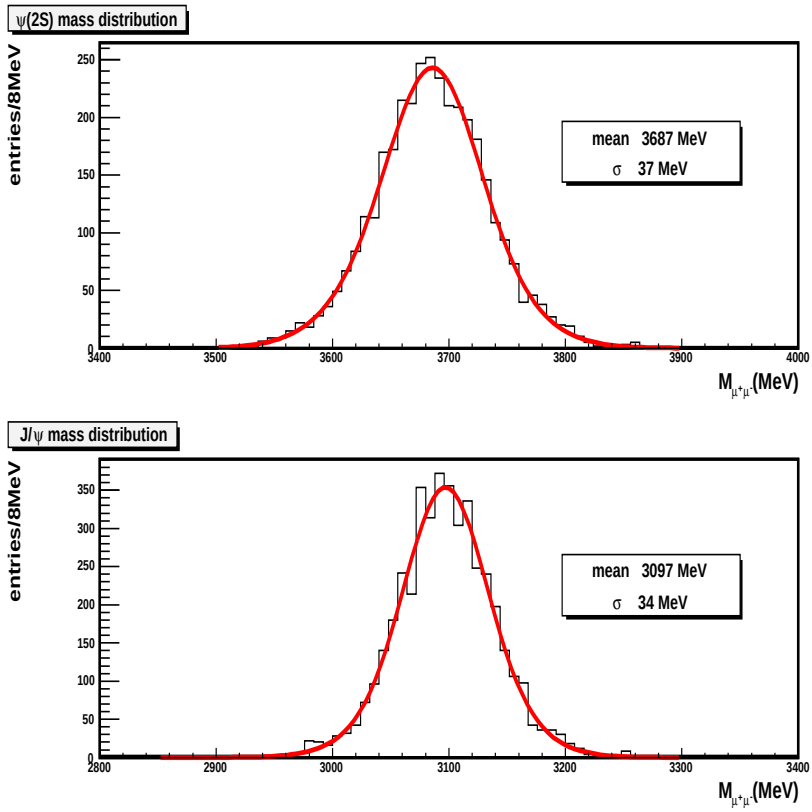

Figure 4.5: *J/ψ and $\psi(2S)$ mass distributions: the mean value and the width of the distributions, resulting from a Gaussian fit, are shown.*

4.3.1 $B^+ \to K^+\mu^+\mu^-$

Dimuon Selection Cuts

Figure 4.6 shows the transverse momentum distribution normalized[1] to 1 for the two muons in the final state for signal and background. As anticipated in Section 6.1, the muon p_T spectra for background and signal events are similar and no cuts can be applied. Analog motivations have been adopted for the muon transverse impact parameter which is shown in Figure 4.7 for signal and background.

The dimuon vertex have to be well reconstructed for the ψ resonances rejection: it has been required to have a χ^2/NDF lower than 3. The χ^2/NDF for dimuon vertex is shown in Figure 4.8.

Figure 4.9 shows the effect on signal and background dimuon invariant mass distributions after the cut $\pm 3\sigma$ around ψ resonance nominal mass values.

[1] In the following normalized distribution is intended normalized to 1.

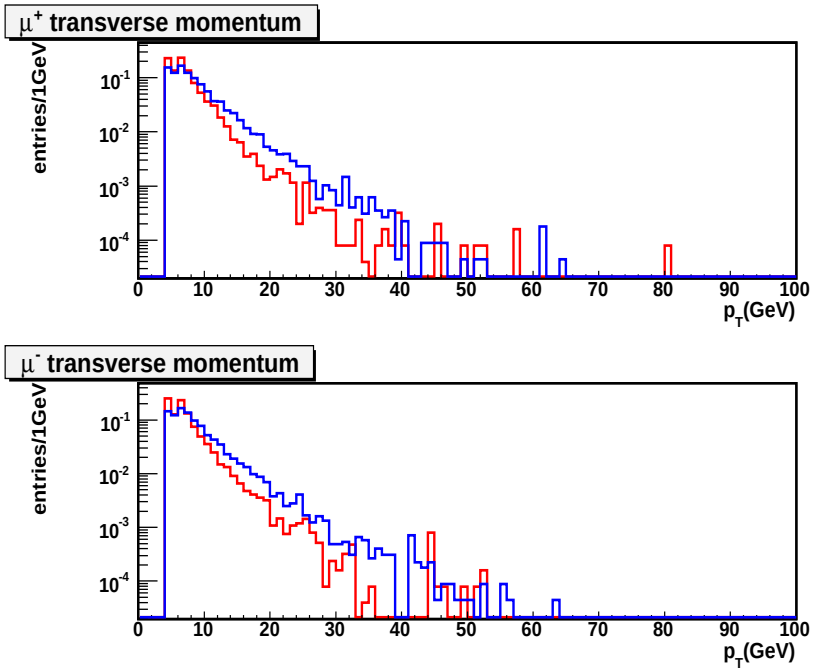

Figure 4.6: *Muon p_T normalized distributions for signal (blue) and background (red).*

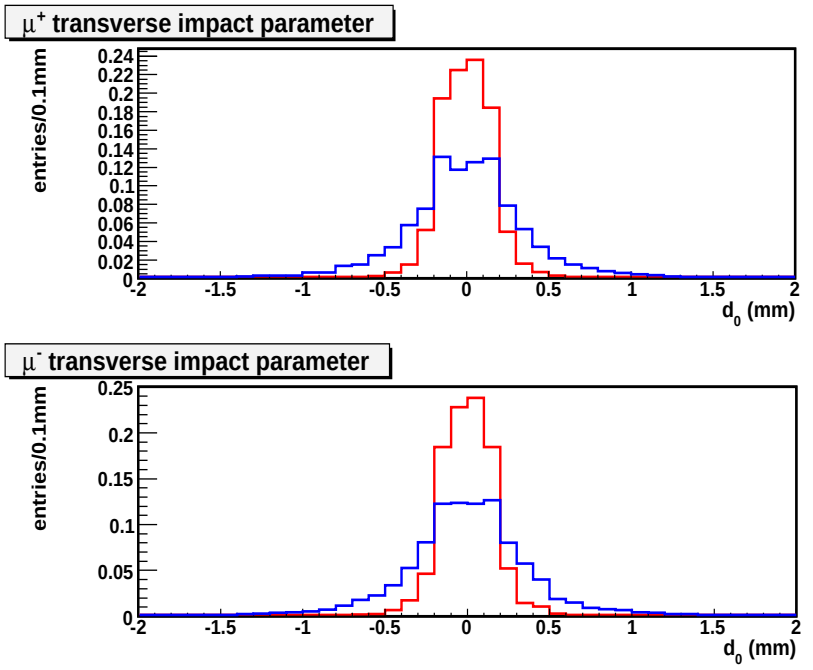

Figure 4.7: *Muon d_0 normalized distributions for signal (blue) and background (red).*

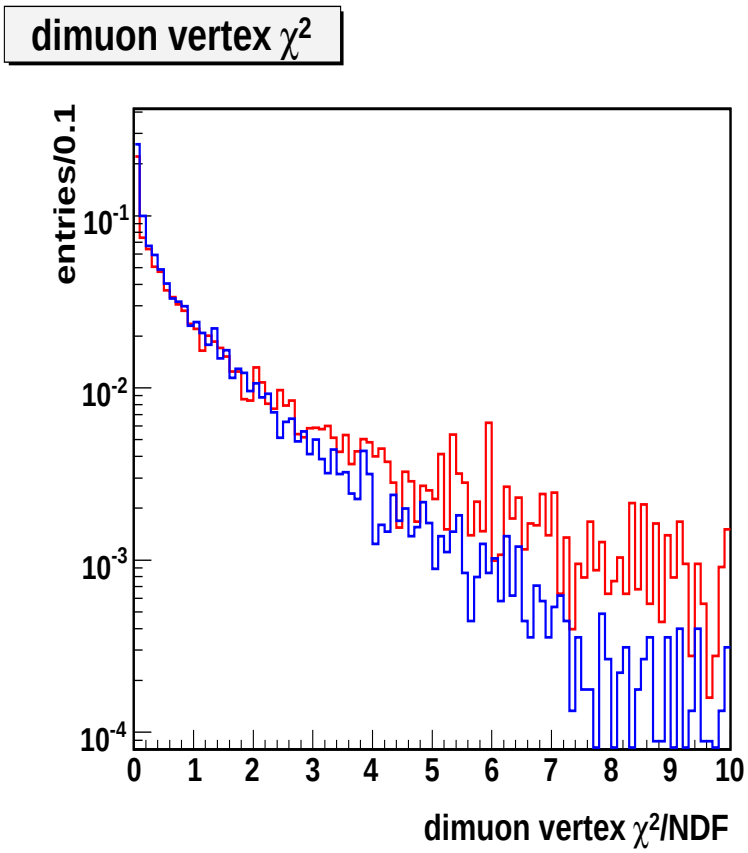

Figure 4.8: *Dimuon vertex χ^2/NDF for signal (blue) and background (red).*

Kaon Selection Cuts

In Figure 4.10 the kaon candidate transverse momentum distributions for signal and background are shown. A cut on kaon $p_T > 1\ GeV$ remove $\sim 90\%$ of the background yield keeping $\sim 40\%$ of signal events. It has been found the most incisive cut for background rejection.

B^+ Selection Cuts

In Figure 4.11 the B^+ vertex χ^2/NDF, mass and proper time distributions are shown. Cuts on these quantities are $\chi^2/NDF < 1.2$, mass in $\pm 3\sigma$ around PDG value and $\tau_{B^+} > 1ps$. They allow to eliminate completely background events.

Final Signal and Background efficiencies

A detailed cut description has been reported in Table 4.6. The final efficiency for signal has been found $\varepsilon = 10\%$. The number of expected events after

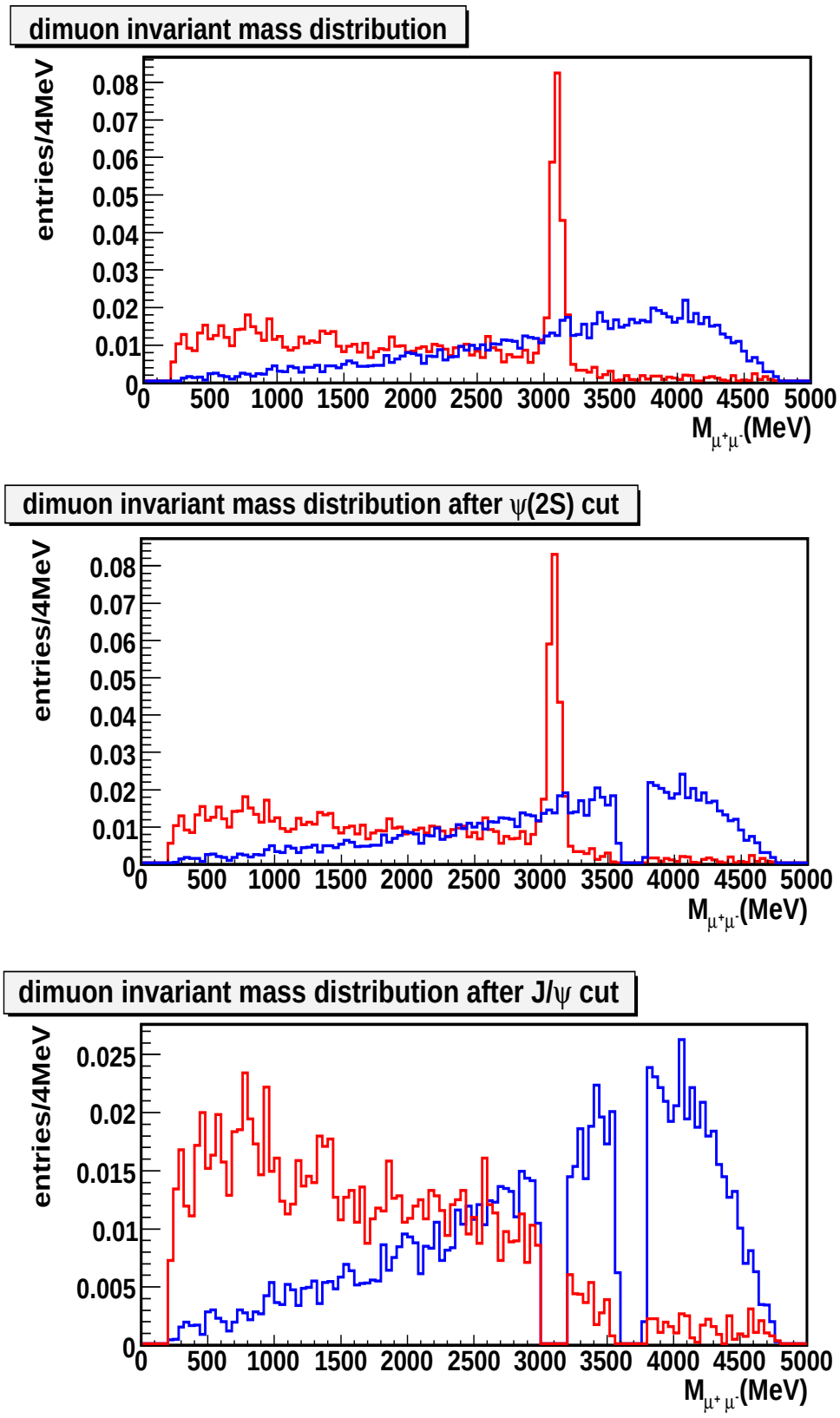

Figure 4.9: *Dimuon invariant mass normalized distribution after cuts on ψ resonances for signal (blue) and background (red).*

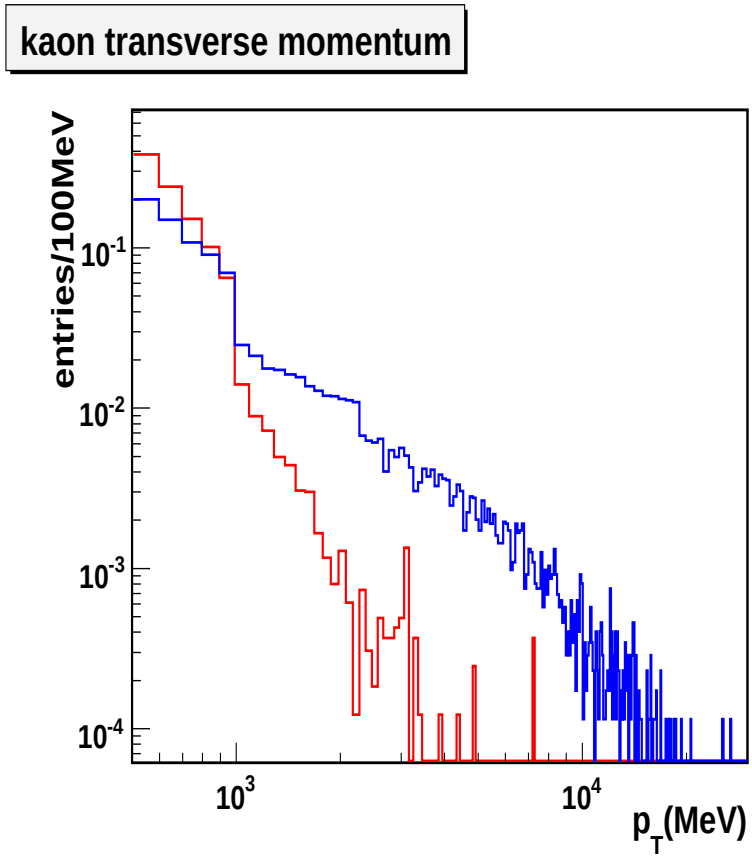

Figure 4.10: *K^+ p_T normalized distribution for signal (blue) and background (red).*

30 fb^{-1} integrated luminosity is thus

$$N = \mathcal{L} \cdot t \cdot T \cdot S \cdot \sigma_{b\bar{b}} \cdot P \cdot \mathcal{BR} \cdot \varepsilon \tag{4.3.1}$$

and hence 4000 expected events. Due to limited background MonteCarlo statistic, the efficiency for background has been found zero. An upper limit of $\sim$ 13000 events at 95% CL can be given for expected background events. This upper limit can be assessed assuming that background events follow a Poisson distribution with large mean $N_{BG} = \mathcal{L} \cdot t \cdot \sigma$ (σ is the cross section) and no events are observed after cuts. The upper limit on the mean value can be found by the Neyman procedure ([6]), giving $N_{BG}^{up} = 3$ at 95% CL to be normalized to the 30 fb^{-1} integrated luminosity.

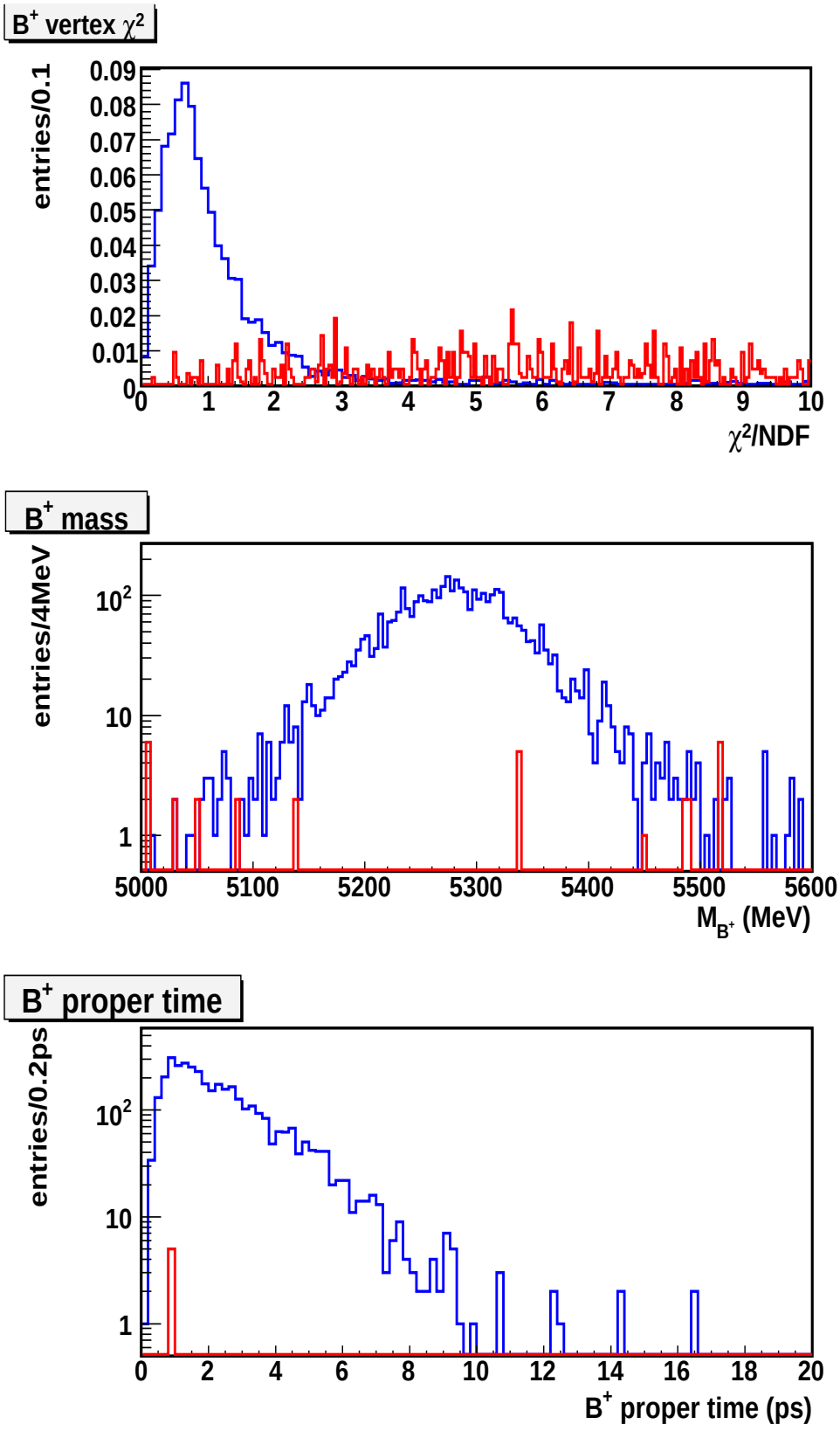

Figure 4.11: *B^+ reconstruction χ^2/NDF (normalized), mass and proper time distributions for signal (blue) and background (red).*

Cut Description	Cut	Signal eff.	$bb \to \mu(4GeV)\mu(6GeV)X$ eff.
basic cuts	vertex fits, kin. cuts on tracks and dimuon mass	0.73	0.104
dimuon vertex	$\chi^2/NDF < 3$	0.92	0.84
$\psi(2S)$ mass cut	$m_{\mu\mu} \notin [m_{\psi(2S)} \pm 3\sigma]$, $\sigma = 37MeV$, $m_{\psi(2S)} = 3686MeV$	0.91	0.99
J/ψ mass cut	$m_{\mu\mu} \notin [m_{J/\psi} \pm 3\sigma]$, $\sigma = 34MeV$, $m_{J/\psi} = 3096MeV$	0.92	0.77
kaon p_T and η	$p_T(K^+) > 1GeV$, $\lvert\eta\rvert < 2.5$	0.37	0.05
B^+ vertex	$\chi^2/NDF < 1.2$	0.61	0.036
B^+ mass	$m_{B^+} \in [m_{B^+} \pm 3\sigma]$, $\sigma = 42MeV$, $m_{B^+} = 5279MeV$	0.92	0.17
B^+ proper time	$\tau_{B^+} > 1ps$	0.81	0
Efficiency(ε)		0.10	0
Event in 30 fb^{-1}		4000	< 13000 *at* 95% CL

Table 4.6: *Cut description for* $B^+ \to K^+\mu^+\mu^-$*, efficiency for background rejection and expected events in* 30 fb^{-1} *of integrated luminosity. The so-called "basic cuts" summarize the vertex fit requests, the cuts on muon and hadron tracks and dimuon mass in the kinematic allowed window. The cuts were applied in sequence, and the efficiency of the* n^{th} *cut is given relative to the remaining sample (*$n^{th} - 1$ *cuts applied). The original sample was the sample passing the LVL1 trigger requirements.*

4.3.2 $B^+ \to K^{*+}\mu^+\mu^-$

Dimuon Selection Cuts

Cut on dimuon candidates are the same as those applied for $B^+ \to K^+\mu^+\mu^-$ background rejection (see Section 4.3.1).

K_s^0 Selection Cuts

A cut on K_s^0 candidate transverse momentum has been added to the cuts on vertex quality and invariant mass. Figure 4.12 shows the K_s^0 vertex χ^2/NDF, mass and p_T distributions. The cuts on these quantities are $\chi^2/NDF < 10$, mass in $\pm 3\sigma$ around the PDG value and $p_T > 2\ GeV$

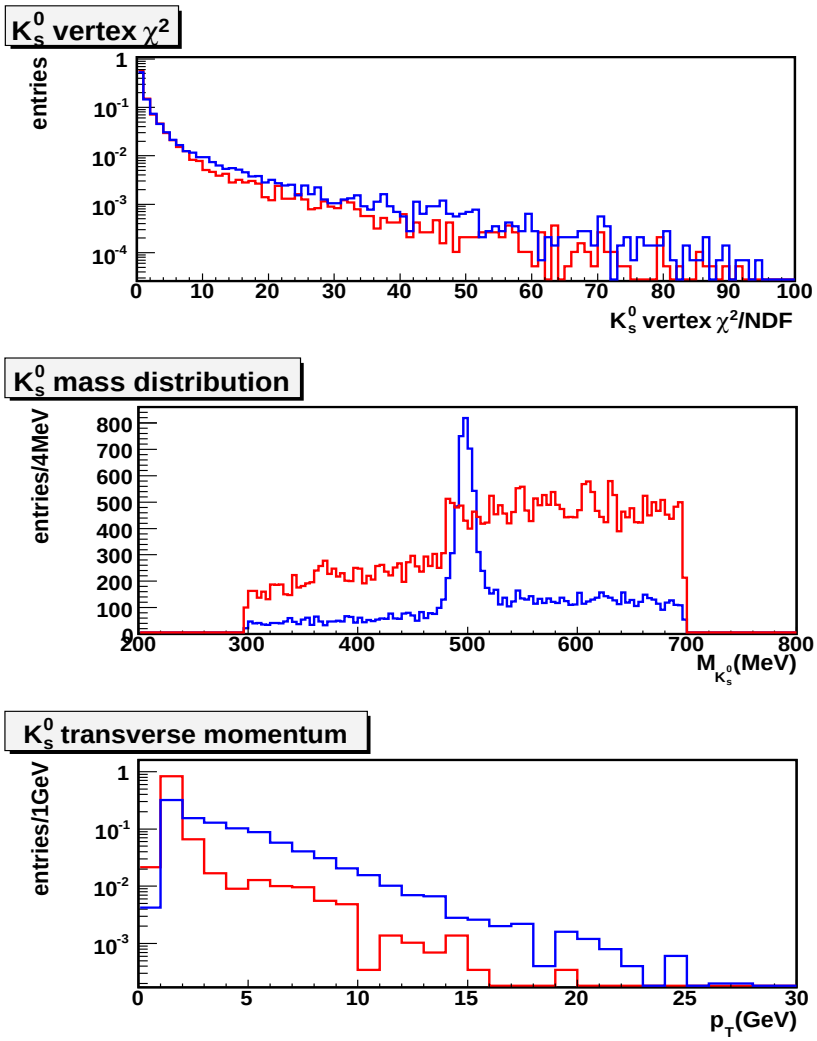

Figure 4.12: *K_s^0 χ^2/NDF (normalized), mass and p_T (normalized) distributions for signal (blue) and background (red).*

K^{*+} Selection Cuts

Figure 4.13 shows the K^{*+} vertex χ^2/NDF, mass and p_T distributions: the cuts are $\chi^2/NDF < 5$, mass in $\pm 3\sigma$ around the PDG value and $p_T > 3\ GeV$

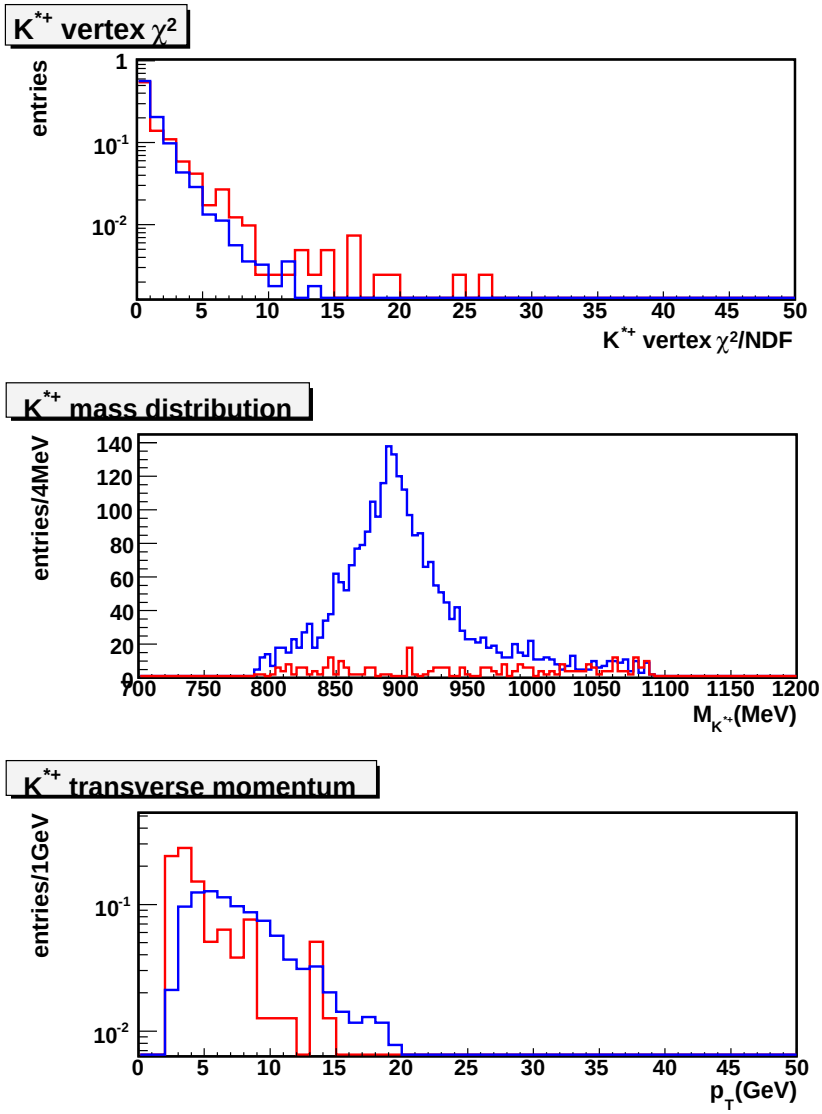

Figure 4.13: *K^{*+} χ^2/NDF (normalized), mass and p_T (normalized) distributions for signal (blue) and background (red).*

B^+ Selection Cuts

In Figure 4.14 the B^+ vertex χ^2/NDF, mass and proper time distributions are shown. The cuts on these quantities are $\chi^2/NDF < 2$, mass in $\pm 3\sigma$ around the PDG value and $\tau_{B^+} > 1\ ps$. They allow to eliminate completely background events.

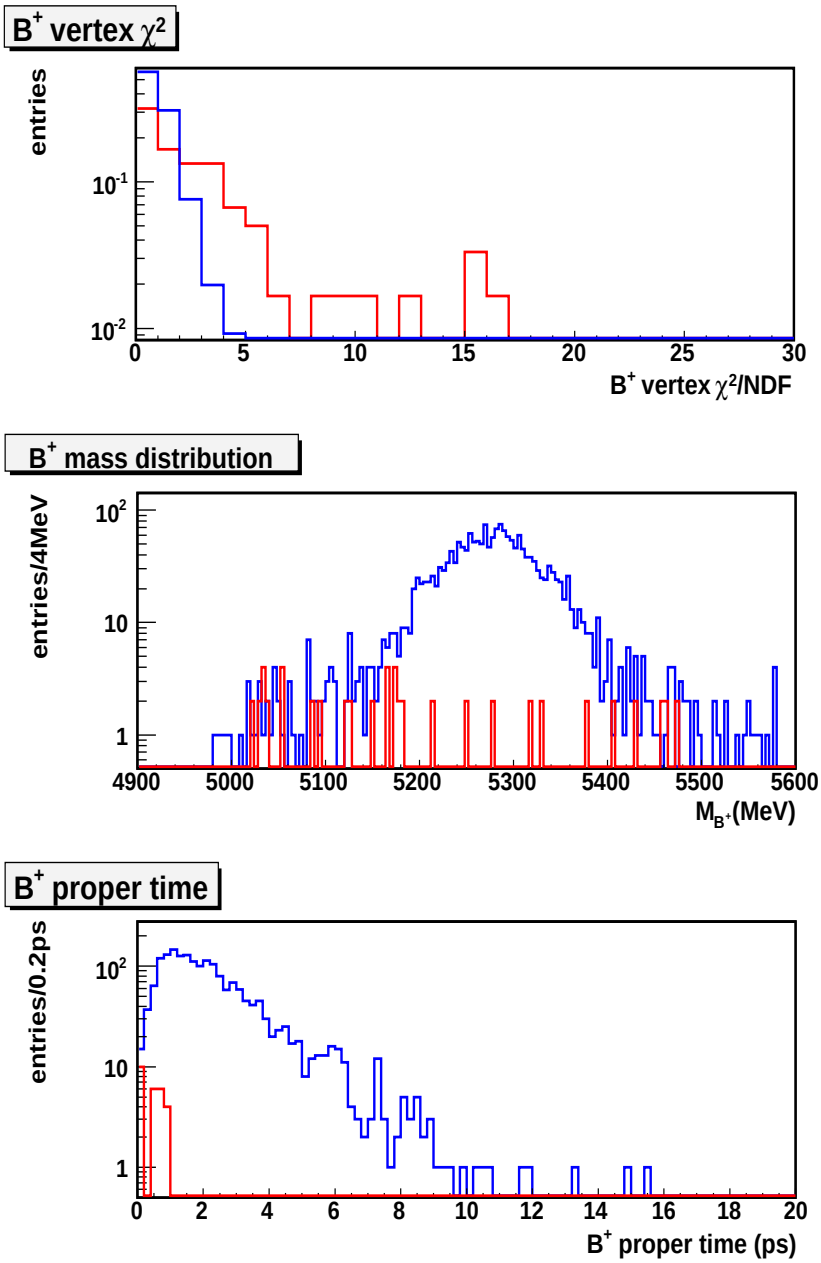

Figure 4.14: *B^+ χ^2/NDF (normalized), mass and proper time distributions for signal (blue) and background (red).*

Final Signal and Background efficiencies

A detailed cut description has been reported in Table 4.7. Also final efficiencies and expected events in 30 fb^{-1} have been tabulated. The final efficiency for signal has been found $\sim$ 4.5% and this lead to an expected number of event after 30 fb^{-1} integrated luminosity of 2300. As for the $B^+ \to K^+\mu^+\mu^-$ decay, an upper limit of $\sim$ 13000 events at 95% CL can be given for expected background events after 30 fb^{-1} of integrated luminosity.

Cut Description	Cut	Signal eff.	$b\bar{b} \to \mu(4GeV)\mu(6GeV)X$ eff.
basic cuts	vertex fits, kin. cuts on tracks and dimuon mass	0.47	0.25
dimuon vertex	$\chi^2/NDF < 3$	0.92	0.84
$\psi(2S)$ mass cut	$m_{\mu\mu} \notin [m_{\psi(2S)} \pm 3\sigma]$, $\sigma = 37MeV$, $m_{\psi(2S)} = 3686MeV$	0.94	0.99
J/ψ mass cut	$m_{\mu\mu} \notin [m_{J/\psi} \pm 3\sigma]$, $\sigma = 34MeV$, $m_{J/\psi} = 3096MeV$	0.92	0.73
K^0_s vertex	$\chi^2/NDF < 89$	0.34	0.94
K^0_s mass	$m_{K^0_s} \in [m_{K^0_s} \pm 3\sigma]$, $\sigma = 9MeV$, $m_{K^0_s} = 497.6MeV$	0.39	0.16
K^0_s p_T	$p_T > 2GeV$	0.68	0.14
K^{*+} vertex	$\chi^2/NDF < 5$	0.94	0.90
K^{*+} mass	$m_{K^{*+}} \in [m_{K^{*+}} \pm 3\sigma]$, $\sigma = 26MeV$, $m_{K^{*+}} = 892MeV$	0.87	0.49
K^{*+} p_T	$p_T > 3GeV$	0.98	0.76
B^+ vertex	$\chi^2/NDF < 2$	0.87	0.48
B^+ mass	$m_{B^+} \in [m_{B^+} \pm 3\sigma]$, $\sigma = 49MeV$, $m_{B^+} = 5279MeV$	0.95	0.28
B^+ proper time	$\tau_{B^+} > 1ps$	0.80	0
Efficiency(ε)		0.045	0
Event in 30 fb^{-1}		2300	< 13000 *at* 95% *CL*

Table 4.7: *Cut description for* $B^+ \to K^{*+}\mu^+\mu^-$ *and efficiency for background rejection. The so-called "basic cuts" summarize the vertex fit requests, the cuts on muon and hadron tracks and dimuon mass in the kinematic allowed window. The cuts were applied in sequence, and the efficiency of the* n^{th} *cut is given relative to the remaining sample (*$n^{th} - 1$ *cuts applied). The original sample was the sample passing the LVL1 trigger requirements.*

4.4 Expected Events and Background Estimation

As showed in the previous section, imposing smart cuts allows to remove all the background events coming from beauty decays.

Compatibly whit the current MonteCarlo statistics, an estimate of the background produced in 30 fb^{-1} can be achieved by the following method. The procedure will be explained in detail for $B^+ \to K^+\mu^+\mu^-$ decay, and then applied also to $B^+ \to K^{*+}\mu^+\mu^-$ channel.

Without applying the cut on B^+ mass, the mass distribution in the range $5000 - 5600\ GeV$ is computed. Counting the events in the mass region, one can obtain the number of background events

$$N_{BG} = 7\ events \tag{4.4.1}$$

Looking at the same mass window as the signal i.e. $250\ MeV$, one can compute the number of background events as

$$N_B = rN_{BG} \tag{4.4.2}$$

where r is the ratio of the window sizes:

$$r = \frac{250\ MeV}{600\ MeV} \sim 0.42 \tag{4.4.3}$$

Clearly the windows sizes and N_{BG} have to be determined using much larger background samples than have been available for this study. With the current statistic, this calculation leads to 2.9 background events within $250\ MeV$. The number of generated events that fulfills the LVL1 trigger is 250000, and it leads to a fake reconstruction efficiency of

$$\varepsilon_{fake} = 1.2 \times 10^{-5} \tag{4.4.4}$$

The result leads to a total of $B = \mathcal{L} \cdot t \cdot \sigma_{b\bar{b}\ trig} \cdot \varepsilon_{fake} \sim 12000$ background events in 30 fb^{-1}. In Figure 4.15 the mass spectrum for background events added to signal events is plotted in the mass range $5000 - 5600\ GeV$. The background is fluctuating around 2400 and on top of it the signal peak is clearly visible.

To test whether the seen peak is a peak and not statistical fluctuation the statistical significance is computed as

$$\mathcal{S}_{stat} = \frac{Signal}{\sqrt{Background}} = \frac{S}{\sqrt{B}} \tag{4.4.5}$$

If significance is greater than 5, then the signal is observable. In the analysis with a signal of ~ 4000 events and a background of ~ 12000 events in the signal mass window $m_{B^+} \pm 3\sigma$, a statistical significance of 35 is computed.

For $B^+ \to K^{*+}\mu^+\mu^-$ decay, the same procedure leads to ~ 14000 background events in 30 fb^{-1} in the signal mass window. In Figure 4.16 the mass

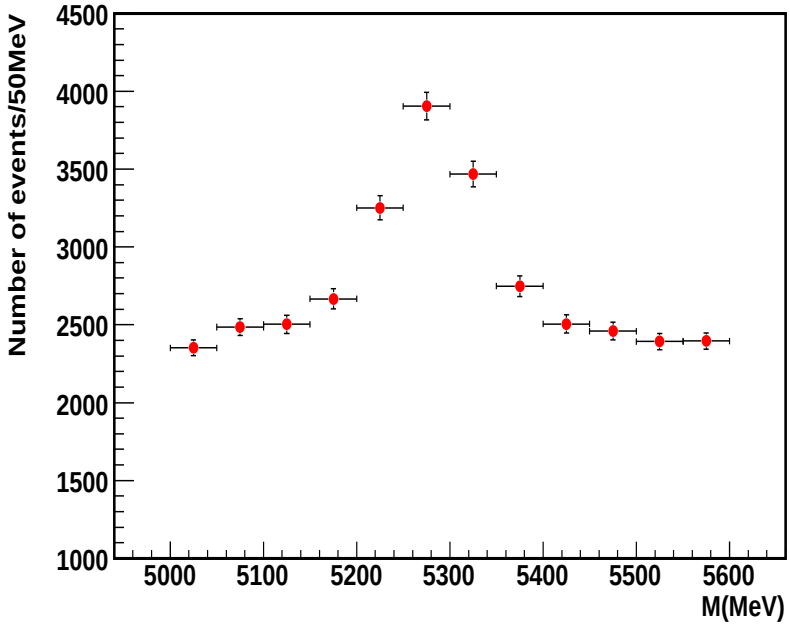

Figure 4.15: *The B^+ signal of $B^+ \to K^+\mu^+\mu^-$ decay after 30 fb^{-1} integrated luminosity. The background estimation is done on the available MonteCarlo statistic.*

spectrum for background events added to signal events is plotted in the mass range $5000 - 5600\ GeV$. The background is fluctuating around 2800 and on top of it the signal peak is visible. The statistical significance has been found $\mathcal{S}_{stat} = 19$.

These results are summarized in Table 4.8.

Decay	ε_i	S_i	B_i
$B^+ \to K^{*+}\mu^+\mu^-$	0.045	2300	14000
$B^+ \to K^+\mu^+\mu^-$	0.10	4000	12000

Table 4.8: *Expected events for $B^+ \to K^{(*)+}\mu^+\mu^-$ (S_i) and background (B_i) in 30 fb^{-1}. Also the signal efficiency ε_i has been reported.*

4.5 Branching Ratio Measurements

To estimate the statistical error on an exclusive branching ratio measurement, it has been assumed that in 30 fb^{-1} integrated luminosity $\bar{N}_i$ events are observed in the B^+ mass window, of which $\bar{B}_i$ are background and $\bar{S}_i$ signal

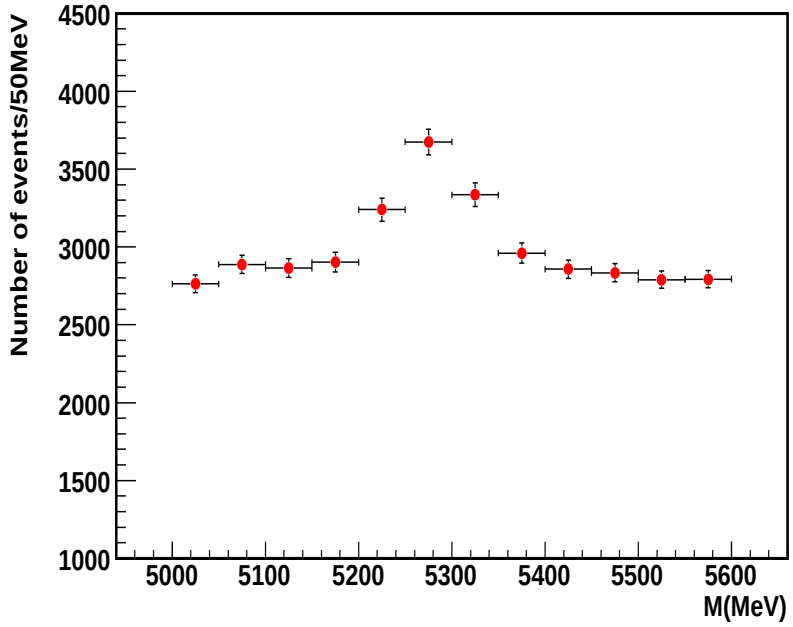

Figure 4.16: *The B^+ signal of $B^+ \to K^{*+}\mu^+\mu^-$ decay after 30 fb^{-1} integrated luminosity. The background estimation is done on the available MonteCarlo statistic.*

events[2]:

$$\bar{N}_i = \bar{S}_i + \bar{B}_i \tag{4.5.1}$$

The estimates of the signal and background yields are given in table 4.8.

N_i events are observed in a narrow B mass window and P_i events in a wider window. The background in the narrow mass window is

$$\bar{B}_i = r\bar{P}_i \tag{4.5.2}$$

where r is defined as in Eq. (4.4.3).

$\bar{S}_i$ will be determined as

$$\bar{S}_i = \bar{N}_i - \bar{B}_i = \bar{N}_i - r\bar{P}_i \tag{4.5.3}$$

The numbers of events N_i and P_i observed after 30 fb^{-1} are random realizations of $\bar{N}_i$ and $\bar{P}_i$

$$N_i = \bar{N}_i \pm \sigma(N_i) \qquad \sigma^2(N_i) \sim \bar{N}_i \sim N_i \tag{4.5.4}$$

[2] Throughout this section X denote the random realization of a variable with mean $\bar{X}$ and following a Poissonian distribution with a large mean, thus $\sigma^2(X) = \bar{X}$.

$$P_i = \bar{P}_i \pm \sigma(P_i) \qquad \sigma^2(P_i) \sim \bar{P}_i \sim P_i \tag{4.5.5}$$

The statistical error on the number of events S_i is thus given by

$$\sigma^2(S_i) = \sigma^2(N_i) + r^2\sigma^2(P_i) \sim N_i + r^2 P_i \tag{4.5.6}$$

In the present case, S_i and B_i are know form the previous section. Using Eq. (4.5.1) and (4.5.2), Eq. (4.5.6) can be rewritten as

$$\sigma^2(S_i) \sim S_i + (1+r)B_i \tag{4.5.7}$$

The yield S_i has to be re-weighted by the corresponding selection efficiency ε_i, the LVL1 trigger fraction T and the isospin weight ω_i

$$R_i = \frac{\omega_i}{\varepsilon_i T} S_i = f_i S_i \tag{4.5.8}$$

Few worlds have to be spent about isospin weight. Isospin invariance in strong decays allows to recover invisible isospin-conjugated decay channels. For instance, the decay $B^+ \to K^{*+}\mu^+\mu^-$ is only visible via $K^{*+} \to K^0_s\pi^+$ final state which accounts for 2/3 of the total branching ratio. Every reconstructed $K^0_s\pi^+$ final state has to be weighted by a factor 3/2 in the analysis. The same kind of arguments are also valid for the K^0_s which is only visible via $K^0_s \to \pi^+\pi^-$. This final state has to be weighted by $1/(0.5 \cdot 0.69) = 2.9$. Obviously, for the $B^+ \to K^+\mu^+\mu^-$ decays the isospin weight is equal to 1.

The branching ratio is proportional to R_i, and thus the error is

$$\frac{\sigma(\mathcal{BR}_i)}{\mathcal{BR}_i} = \frac{\sigma(R_i)}{R_i} \tag{4.5.9}$$

where $\sigma(R_i) = f_i\sigma(S_i)$. The second term of the uncertainty depending on $\sigma(f_i)$ is not taken into account as it enters the systematic uncertainty.

The statistical error on branching ratio for the two decays, is then

$$\frac{\sigma(\mathcal{BR}_i)}{\mathcal{BR}_i}(B^\pm \to \mu\mu K^\pm) \sim 3.5\% \tag{4.5.10}$$

$$\frac{\sigma(\mathcal{BR}_i)}{\mathcal{BR}_i}(B^\pm \to \mu\mu K^{*\pm}) \sim 6.5\% \tag{4.5.11}$$

The errors are much smaller than the current experimental and theoretical ones (see Tables 1.2 and 1.3 in Sections 1.7.1 and 1.9 respectively). These measurements are thus interesting inputs to test the various theoretical models. They could be selective between the Standard Model and beyond SM theories.

4.6 Conclusions

With the present study on the $B^+ \to K^+\mu^+\mu^-$ and $B^+ \to K^{*+}\mu^+\mu^-$ decays, many positive results have been achieved. A complete review can be found in [84] and [85].

All the software chain, from event generation to reconstruction and analysis, has been tested using GRID facilities and it is now available in the ATLAS official software distribution. The analysis strategy of the two decay channels for the ATLAS data taking, which will begin at the end of 2007, is ready. The analysis C++ code has been implemented in the ATLAS official software framework.

The most interesting quantities for the rare semileptonic beauty decays are the differential dimuon invariant mass and the forward-backward asymmetry. New Physics might result in significant enhancement compared to the Standard Model predictions and thus their measurement, as well as the measure of the branching ratio, provide an indirect search for New Physics. The study on simulated data shows that the trigger and the offline analysis cuts do not change the shape of the dimuon mass spectrum and the FBA distribution.

Also background rejection strategy is ready and it has been tested on $250k$ background events. Due to limited background MonteCarlo statistic, only a preliminary background estimation has been done. An upper limit to 13000 events at 95% CL can be given for an integrated luminosity of 30 fb^{-1}. This limit have to be compared with the expected signal yield, 4000 events and 2300 events respectively for $B^+ \to K^+\mu^+\mu^-$ and $B^+ \to K^{*+}\mu^+\mu^-$ decays. Compatibly with the available MonteCarlo statistic, this comparison is done extrapolating background events from a wider mass window around PDG B^+ mass value. The signal is clearly visible over the background level: the statistical significance is very high for both decays.

This method leads to an overestimate of the expected background yield. As shown in the ATLAS Technical Design Report ([34]), the expected number of $b\bar{b}$ background events after 30 fb^{-1} for the rare decay $B_d^0 \to K^{*0}\mu^+\mu^-$ is about 300, to be compared with the expected 2000 signal events. But, compatibly with the low MonteCarlo available statistic, this is the only way to demonstrate the visibility of the decays over the background events and to have some prediction on branching ratio measurements. The errors expected on branching ratio measurements are $\sim 3.5\%$ and $\sim 6.5\%$ respectively for $B^+ \to K^+\mu^+\mu^-$ and $B^+ \to K^{*+}\mu^+\mu^-$ decays. These errors on the branching ratio measurements are much smaller than the current experimental and theoretical ones and this allows to conclude that these measurements are interesting inputs to test the SM versus $SUSY$ theories predicting significant enhancements of these branching ratios.

The present study is being refined by using more MonteCarlo data (background), including also minimum bias pp events and considering pile-up effects to evaluate the possibility to extend the ATLAS studies on rare semileptonic B-decays at high luminosity ($L = 10^{34}\ cm^{-2}s^{-1}$). The contribution of minimum bias events is expected to be poor with respect to the background taken into account ([86]), but an accurate estimation of background yield is needed to perform precise measurements of the forward-backward asymmetry and differential decay rate.

Chapter 5

Muon System Performance at 2004 H8 Test Beam

This chapter presents the studies performed on muon sagitta reconstruction with the ATLAS Muon Barrel chambers at the H8 Combined Test Beam at CERN. The H8 setup has given an unique possibility to measure this quantity in a realistic setup before the installation of the ATLAS experiment. The sagitta resolution of the Barrel Muon Spectrometer has been measured for various muon momenta, thus disentangling the intrinsic resolution term from the multiple scattering contribution. The results obtained from the analysis of the data collected during the 2004 Test Beam have been compared to the prediction from the GEANT4 simulation of the Test Beam setup. This comparison constitutes an important validation step for the GEANT4 simulation of the Muon Spectrometer, the second on Test Beam data together with [87]. A complete review of this study can be found in [88].

5.1 Introduction

An extensive set of tests of the ATLAS Muon Spectrometer has been developed at the H8 beam line at the CERN Super Proton Synchrotron. The main aim is to test and to validate many aspects of the Muon System performance. The setup realized for the summer 2004 test reproduced one projective tower of the barrel and one end-cap octant ([89]). During the data taking period events with muon energies ranging from 20 GeV to 350 GeV were collected.

Extensive studies were performed with this setup: mechanical detector installation tests, integration between different technologies of the Spectrometer, the detector control system, integration between different subsystem tasks (trigger and tracking) and different software tools (the data acquisition, databases, high level trigger software, on-line and off-line monitoring and reconstruction, alignment and calibration).

A figure of merit of the Muon Spectrometer performance is the sagitta resolution. The ATLAS Muon Spectrometer has been designed ([42]) to provide a good stand-alone momentum measurement: the transverse momentum (p_T)

should be measured with a resolution of $\Delta p_T/p_T = 10\%$ at $p_T = 1\ TeV$. Since the bending of the 1 TeV muon track is such that the track sagitta varies between 500 μm in the barrel and 1 mm in the end-cap, the error on the sagitta measurement must be at level of 50 μm.

The H8 setup has given an unique possibility to measure this quantity in a realistic setup before the installation of the ATLAS experiment. The measured sagitta resolution depends not only on the intrinsic resolution but also on multiple scattering: an energy scan is needed to disentangle the two contributions. On this purpose, with the 2004 H8 data it was also possible to measure the beam momentum[1].

5.2 The H8 Muon Setup for the 2004 Test

The H8 muon beam, with energies ranging from 20 to 350 GeV, was obtained from the proton beam provided by the SPS CERN accelerator.

The upstream section of H8 test area was reserved to Calorimeter and Inner Detector tests, and it was separated from the Muon Spectrometer area by the beam dump, an iron block of 3.2 m thickness.

A schematic top view of the 2004 muon setup is shown in Figure 5.1, where the two parts, the barrel stand and the end-cap stand are visible.

Since the analysis has been performed only on data collected by the barrel detectors, in the following the main emphasis will be given to the description of the barrel stand. A detailed description of the setup can be found in [89].

The barrel part was emulating a barrel sector of the Muon Spectrometer, and it consisted of six MDT chambers and six RPC chambers, with the MDT tubes oriented in vertical position (perpendicular to the plane of the Figure 5.1) and tube layers which were forming with the beam an angle of about 15^o (0.26 rad).

The MDT chambers were: two inner large (BIL), two middle large (BML) and two outer large (BOL) chambers, installed on three rails. The chambers were fully instrumented with front-end electronics (FE) and readout with the Muon Readout Driver (MROD) ([90]) and equipped with the optical alignment system.

Each of the MDT chamber of the middle station had one RPC doublet upstream and another doublet downstream, while the MDT chamber of the outer station had one RPC doublet placed downstream, as foreseen in the layout of the ATLAS Muon Spectrometer ([42]).

The beam did not illuminate uniformly the two towers of barrel chambers (a tower is composed by a BIL, a BML and a BOL chamber). The tower at the top of Figure 5.1 was the most illuminated; therefore, only events collected with this tower have been considered in the analysis.

Two additional barrel stations were present on the beam line, upstream the barrel sector: one outer station upstream of the muon wall and one inner

[1] A beam magnet has been installed between the MDT chambers as described in Section 5.2.

barrel on a rotating support (hereafter called "rotating BIL"). The "rotating BIL" could rotate around its axis from 0^0 to $\pm 10^0$ respect to the direction normal to the beam in the horizontal plane (the plane of the Figure 5.1).

A beam magnet was installed between the "rotating BIL" and the barrel sector, in order to bend the muon track in the horizontal plane (the magnetic field generated by this dipole points along the MDT wires, the vertical coordinate). The magnet current could be controlled remotely in the counting room and varied from 0 A up to ± 600 A, thus providing a maximum field integral of about 4 Tm.

In the analysis, the RPCs have been used to perform measurement of the second-coordinate (the vertical coordinate, directed along the MDT wires and orthogonal to the precision coordinate measured by the MDT chambers.). Two external trigger systems were available: a small area trigger (SAT), given by the coincidence of the signals of two scintillators (10×10 cm^2) centered on the beam line, and installed upstream the magnet; a large area trigger (hodoscope trigger) (60×100 cm^2) given by the coincidence of the signals of two planes of six scintillating slabs (each of 10×100 cm^2). When using the hodoscope trigger, the possibility of vetoing the area covered by the small area trigger was foreseen, in order to suppress the higher rate central part of the beam and have a more uniform illumination of the chambers over the whole hodoscope trigger area.

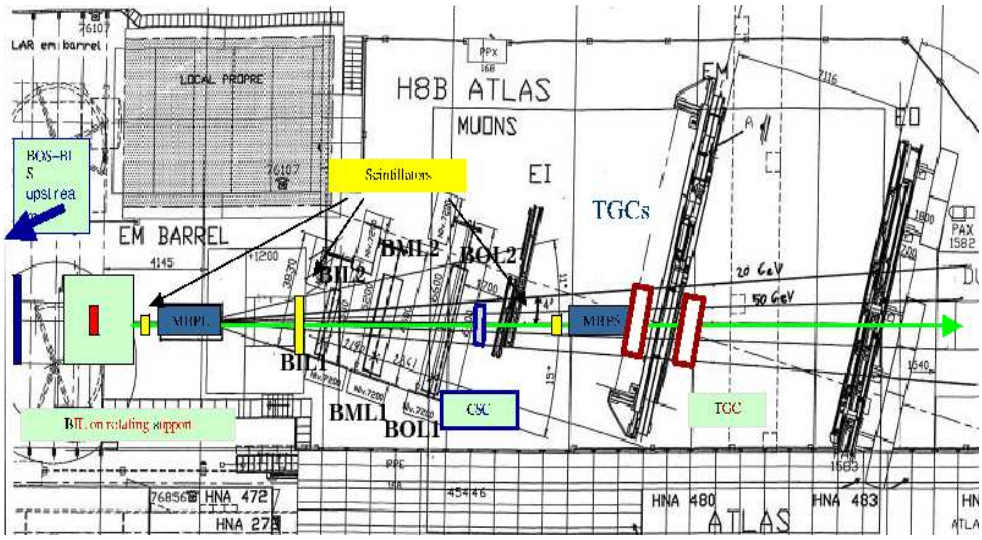

Figure 5.1: *Schematic top view of the 2004 muon setup on the H8 Test Beam area.*

5.3 Data Sets

Data on which this analysis has been performed were collected with the barrel chambers and the "rotating BIL" operated in the nominal ATLAS conditions.

The gas mixture of MDT chambers was : $Ar(93\%)$ and $CO_2(7\%)$ at 3 bar absolute pressure. The high voltage was 3080 V. The trigger system was the 10×10 cm^2. Data have been collected at three different MDT discriminator thresholds: -36, -40 and -44 mV. For each threshold a scan of beam momentum has been performed between 100 and 250 GeV, by varying the settings of the H8 beam, with these nominal values indicating the beam momentum at the H8 entry, before the crossing of the Calorimeters and of the beam dump. As it will shown with the measured momentum distributions, it is not possible to obtain a perfectly monochromatic beam.

For each group of data at the same beam momentum and at the same threshold, three runs taken in sequence has been selected to perform the analysis:

- a run during which the "rotating BIL" chamber was rotating. This sample has been used, as will be explained in Section 5.4.2, to compute the space-time relation of the gas mixture.
- a run during which the "rotating BIL" was fixed and the the magnet was switched off. This sample has been used to measure the misalignment of the "rotating BIL" respect to the barrel sector.
- a run during which the "rotating BIL" was fixed and the magnet was switched on. This sample has been used to perform both sagitta and momentum measurement.

The analysis has been performed using the package `MuonTestBeam` of the ATHENA release 10.0.0 ([49] and Section 3.7.3).

5.4 Calibration Data

5.4.1 t_0 Computing

The measured time for each MDT tube is the difference between the TDC counts of the tube and the TDC counts of the scintillator trigger. A large constant is then added to have only positive numbers. Figure 5.2 shows a typical time spectrum. The non-uniformity of the drift velocity for the $ArCO_2$ mixture is evident. The physical time window, due to hits induced by particles, is well visible.

The t_0 is defined as the beginning of the physical time window and it corresponds to the drift time associated to particles crossing the drift tube very close to the wire. In the same way, the t_{max} is the end of the physical time window, corresponding to the drift time associated to particles crossing the tube close to the wall. The difference $t_d = t_{max} - t_0$ depends on the tube drift properties. In the Test Beam run condition, t_d is the same for all tube within statistical accuracy. The t_0 value depends on delays introduced by the signal cables and front-end electronics as well as on discriminator threshold and HV setting. It is independent on the drift characteristics of the tube.

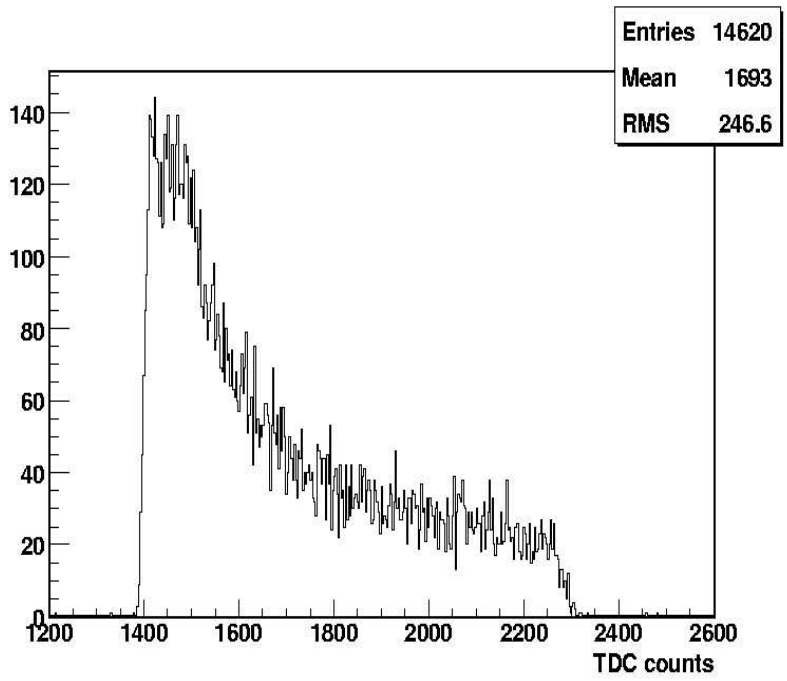

Figure 5.2: *TDC spectrum of a MDT tube (a TDC count correspond to* 0.78 *ns).*

For each tube, the parameter of the raising of the drift time spectrum has been derived from a fit with the following Fermi-Dirac function:

$$\frac{dn}{dt} = \frac{P_0}{1 + e^{\frac{P_1 - t}{P_2}}} + P_3 \tag{5.4.1}$$

Here P_3 is the noise level, P_1 is the t_0, P_0 and P_2 are related to the shape of the signal distribution. It has been shown in [91] that the accuracy in determining t_0 is about $0.5ns$ for a $20k$ track sample for tube. In order to reduce the statistical uncertainties all the data at a fixed discriminator threshold are summed up to compute the fit. Figure 5.3 show an example of a TDC spectrum raising fit.

5.4.2 Space-time Relation

An accurate knowledge of the relation between the measured drift time and the distance of the minimum approach of the particle trajectory to the wire, called drift distance, is necessary to perform the track fit. This relation is referred as *r(t)* relation.

The iterative procedure to compute the *r(t)* relation is called *autocalibration.* It makes use of the information from the measured drift time and of the precise knowledge of the wire position. The standalone C++ software tool `Calib` ([92]) has been used to perform autocalibration. `Calib` follows

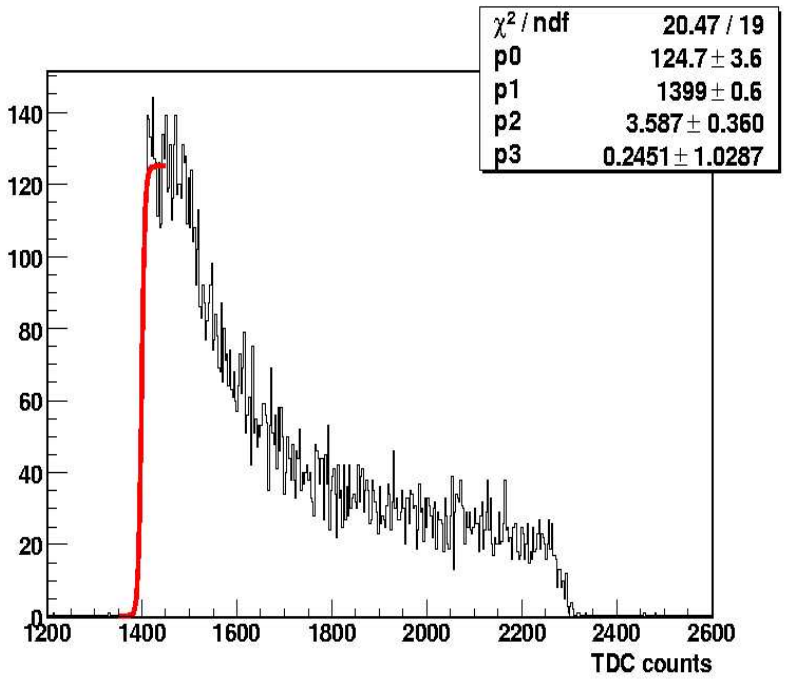

Figure 5.3: *Example of a TDC spectrum raising fit.*

the autocalibration algorithm described in [93]. The space-time relation of a tube depends on its operating condition as well as on the gas composition, pressure, temperature and, in the ATLAS environment, on the magnetic field. It is expected that tubes operating in the same conditions have the same *r(t)* relation. The algorithm for the autocalibration consists in two steps. The t_0 of each tube is computed and subtracted to measured drift time to equalize the times in different tubes. Then, assuming an appropriate function for the drift velocity (the initial *r(t)* relation), the best straight line tangent to the circles representing the hits is computed through the χ^2 method. By minimizing the average residuals to the fit, the best *r(t)* relation is evaluated. A convergence condition is required to stop iterations as described in [91]. It is important to stress that this procedure converges to an unique and bias-free solution only if the angular spread of the tracks is at least 100 *mrad* ([94]), in fact a parallel track beam correlates in an unique way the measured drift time in the tubes and the autocalibration is not sufficiently constrained.

In 2004 H8 setup, to obtain the required angular spread, the "rotating BIL" chamber was rotated around its vertical axis (along the wires) from 0^0 to $\pm 10^0$. It has been show in [95] that with this angular range the algorithm converges to the true *r(t)* relation with a 10 μm accuracy using a 20 k tracks sample.

For each data set at the same beam momentum and discriminating threshold, the *r(t)* relations of the two multilayers of the "rotating BIL" have been measured separately using the run during which the chamber was rotating. Figure 5.4 shows a typical *r(t)* relation.

The same single tube space resolution, ranging from $200\mu m$ close the wire to 50 μm close the tube wall, has been used both in autocalibration and in reconstruction for all the discriminator thresholds.

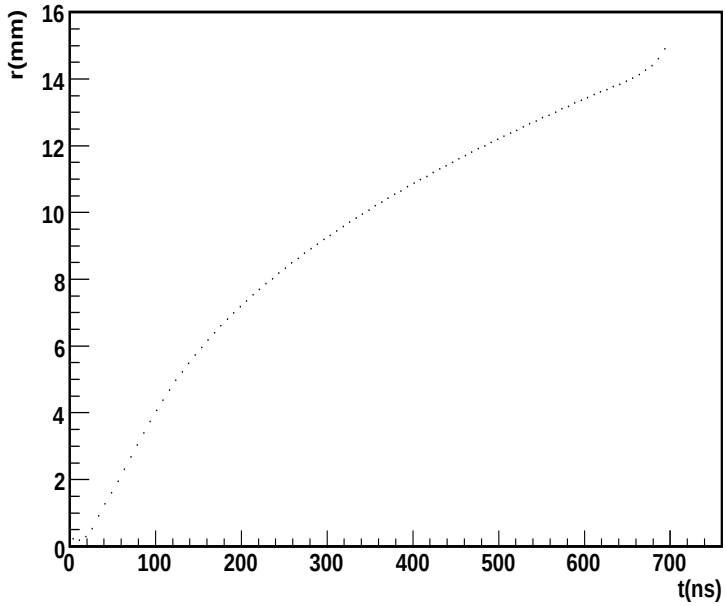

Figure 5.4: *Example of a r(t) relation for the first multilayer of the "rotating BIL".*

The chambers of the barrel sector are kept in fixed position with respect to beam axis. Since they are operated at the same conditions of the "rotating BIL", the *r(t)* relation of the first multilayer of this chamber has been used for all chambers.

A check on the computed t_0's and on *r(t)* relations has been performed investigating the residual distributions separately for each layer as a function of the signed drift distance. The sign disentangles between tracks crossing the tube to the right of the wire, to ones to the left. The residual distributions of the chambers are shown in Figure 5.5. The data refer to the run with a nominal momentum of 150 GeV and a discriminator threshold of -36 mV.

No systematic effects are observed. The large values at small drift distances are due to the difficulty to compute *r(t)* relation near the wire. Since `Calib` autocalibration procedure fails for radii smaller than 1 mm, a linear *r(t)* relation has been used in this drift range. The residual distributions of the "rotating BIL", of the BIL and the BML are within 20 μm for the overall drift range. Quite larger residuals with an asymmetric behaviour are observed for some data sets in BOL chamber.

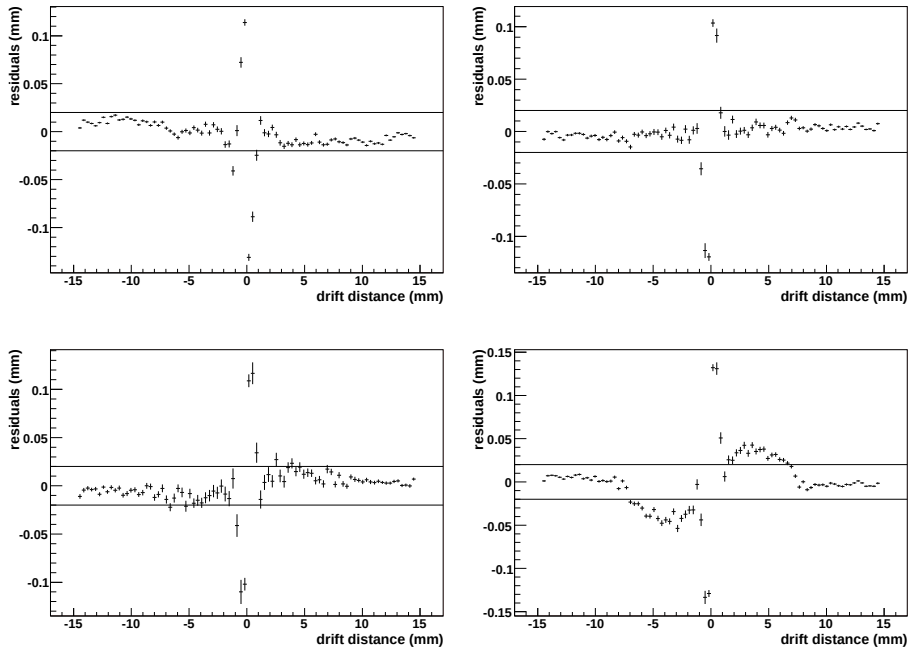

Figure 5.5: *Residual distributions as a function of signed drift distance: for the "rotating BIL" (top-left), for the BIL (top-right), for the BML (bottom-left), for the BOL (bottom-right).*

5.5 The Method to Measure the Sagitta and the Momentum

A very schematic top view of the barrel sector is shown in Figure 5.6. The magnetic field and the wires of the MDTs are directed along $y-$axis (vertical), while the precision coordinate measured by the MDTs is directed along the $z-$axis (on the horizontal plane $z-x$, orthogonal to the magnetic field). The "Rotating BIL" chamber measures the angle (ϑ_{RotBIL}) between the $x-$axis and the muon track upstream of the magnet.

The barrel chambers are measuring the same angle downstream of the field (ϑ_{barrel}). The barrel track is computed as the track that crosses the two super-points associated to the track segments separately in the BIL and BOL chambers, where the super-point is calculated as the crossing point of the track segment, reconstructed through a linear fit of the chamber's hit, at the center of the chamber. The difference between these two angles ($\Delta\vartheta_B$) allows the measurement of the beam momentum as

$$p\ (GeV) = \frac{0.3BL\ (Tm)}{\Delta\vartheta_B\ (rad)} \tag{5.5.1}$$

were BL is the bending power of the magnetic field, which is known as a function of the magnet current.

As for a given run, the orientation of the "rotating BIL" chamber and the

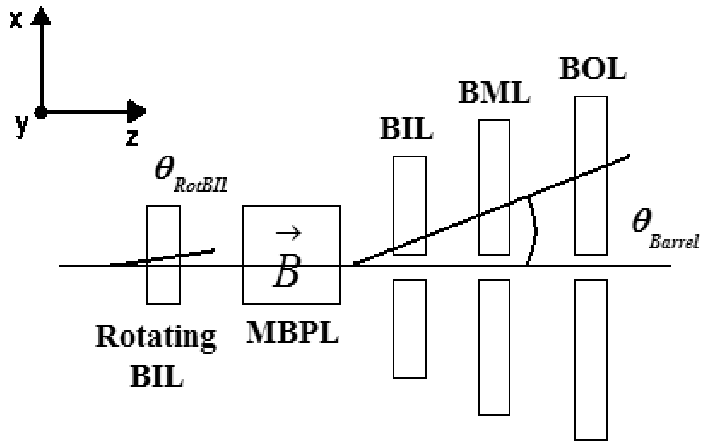

Figure 5.6: *Schematic top view of the barrel sector in the 2004 muon setup on the H8 area. The figure is not in scale.*

barrel chambers is not known, the measurement of the difference as in (5.5.1) has to be repeated with the magnetic field switched off $(\Delta\vartheta_0)$ [2].

The momentum is then given by

$$p\ (GeV) = \frac{0.3BL\ (Tm)}{(\Delta\vartheta_B - \Delta\vartheta_0)\ (rad)} \tag{5.5.2}$$

With this method the muon momentum has been measured using the Muon Spectrometer chambers for the first time. Even if the method is quite different from the one will be used in ATLAS, it is an important exercise to test the tracking performance of the Spectrometer.

Also the measurement of the sagitta cannot be performed in the same way as in the ATLAS environment, since in H8 setup the tracks crossing the chambers are straight lines. The track segments are reconstructed separately in each barrel station (BIL, BML and BOL) and the super-points are calculated, and a straight track crossing the two super-points in the two extreme chambers is computed (it is the same track used to perform muon momentum measurement). The sagitta is the distance between the BML super-point and this track. This method is sketched in Figure 5.7.

5.5.1 Correction for the Vertical Coordinate

As explained in Section 5.2, in H8 setup the barrel chambers are installed on three rails. In the final ATLAS environment, the wires of the different chambers are required to be aligned with a precision of about 2 *mrad*. A vertical length of 10 *cm*, that is the track spread allowed by the small area trigger used, takes a maximal shift of 200 μm of the chamber wire centers

[2] In case of perfect alignment $(\Delta\vartheta_0)$ is zero

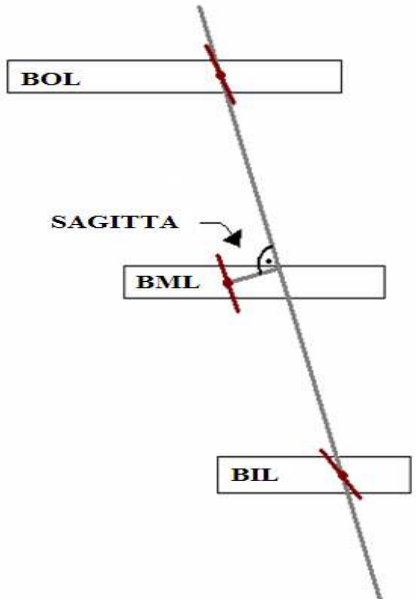

Figure 5.7: *A very schematic top view of the muon H8 barrel sector. The method used to measure sagitta is sketched.*

respect to the nominal position in the $z - x$ plane. Then the sagitta and consequently the sagitta resolution depend on the track vertical coordinate. But once this position has been measured with enough precision, the sagitta resolution becomes independent from it. The $y-$coordinate has been measured by the ϕ-strips of the RPCs, that are the strips perpendicular to the MDT wires. Only tracks that cross the system at the same $y-$coordinate have been used to compute sagitta. In the Figure 5.8 is shown the beam profile for the RPC ϕ-strips of the BML station. In particular the figure on the top reports the beam profile on the first upstream RPC chamber on both the two ϕ-strip layers. The figure on the bottom shows the beam profile on the downstream RPC chamber. Due to the geometry setup, the second chamber is more illuminated than the first.

The most illuminated ϕ-strip has been selected. It is required at least one hit from this strip in the upstream chamber, and at least one hit from it in second chamber. The results reported in the following sections are obtained after this selection has been applied.

5.6 Momentum Measurement

The momentum measurement has been performed as described in Section 5.5. For each beam momentum, the difference $\Delta\vartheta_0$ has been measured to fix misalignment due to rotations around the $y-$axis. A Gaussian fit has been performed on the $\Delta\vartheta_0$ distribution. Then, $\Delta\vartheta_B$ has been computed. The distributions of the two angular differences are shown in Figure 5.9 for the runs

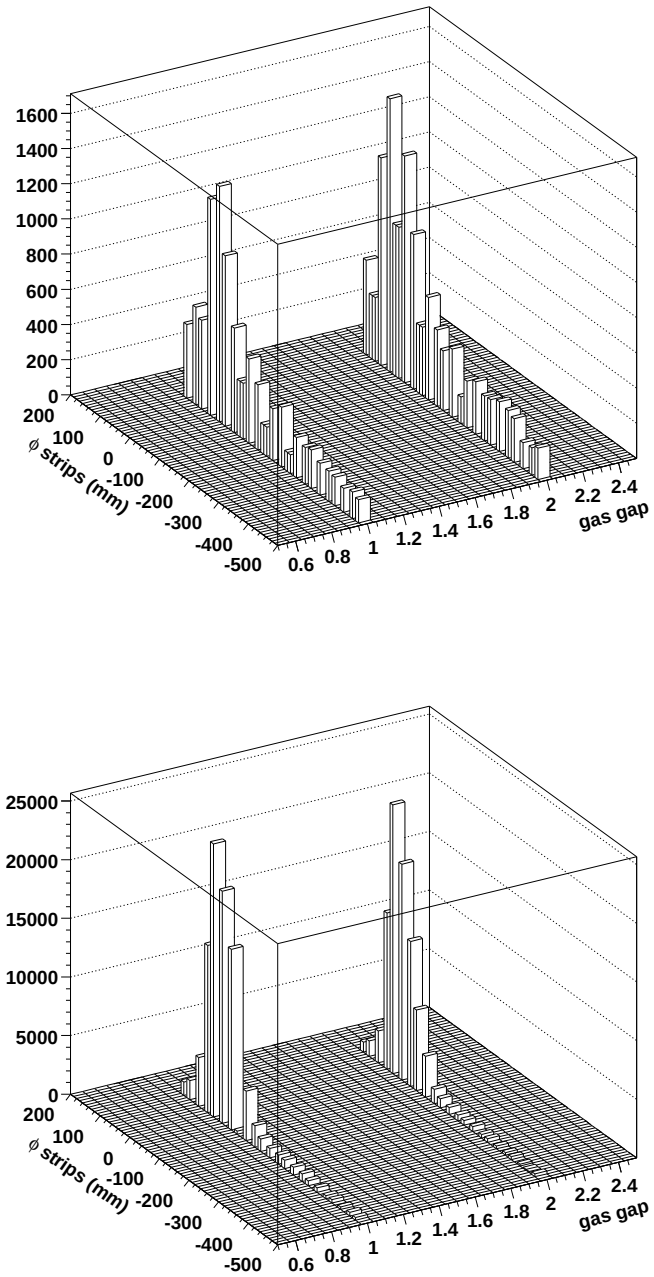

Figure 5.8: *Beam profile on the RPC ϕ-strips of the middle barrel station: on the top the two layers of the first chamber are shown and on the bottom the two layers of the second chamber.*

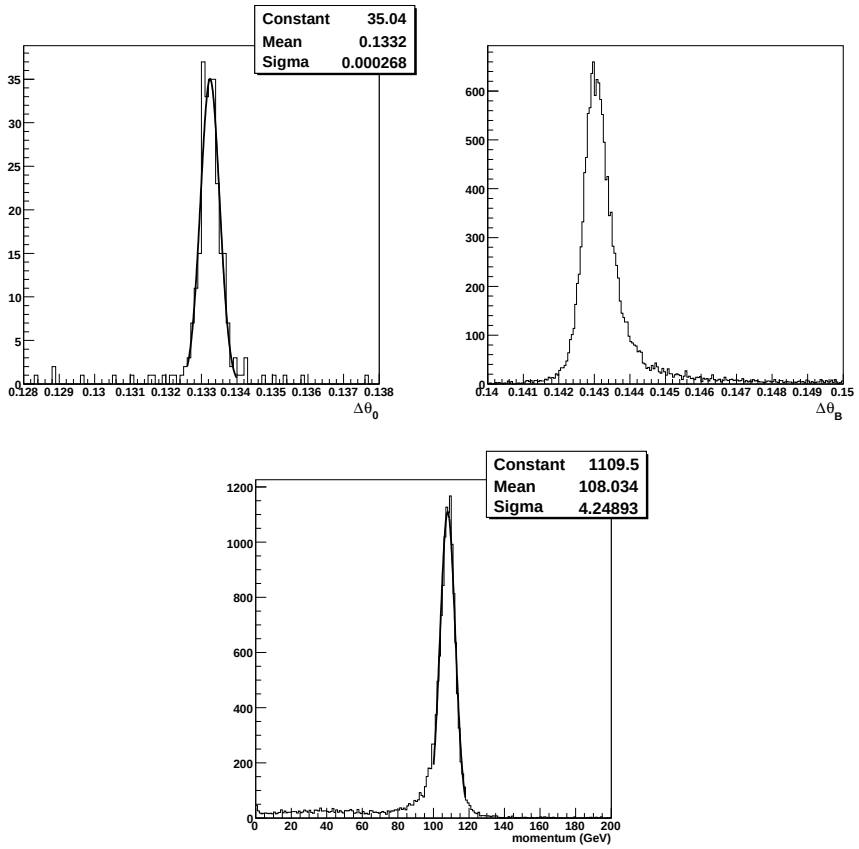

Figure 5.9: *At the top on the left, the distribution of* $\Delta\vartheta_0$*. At the top on the right, the distribution of* $\Delta\vartheta_B$*. At the bottom, the distribution of the beam momentum. The figures refer to the data set at* 120 GeV *nominal momentum.*

with 120 GeV nominal beam momentum and $-40mV$ threshold.

Also the measured momentum spectrum, computed with the formula (5.5.2), is shown. The measured momentum distributions for all the data sets at the -44 mV threshold, are illustrated in Figure 5.10.

In Table 5.1 the mean values and the standard deviations of the momentum distributions at the three different threshold obtained performing a Gaussian fit are shown. The discrepancies observed between the nominal and measured momentum are mainly due to the energy loss by the muons in the Calorimeter material and the beam dump, upstream the muon area.

5.7 Sagitta Resolution Measurement

The sagitta resolution for each data set has been evaluated after two cuts. Only events that pass the RPC cut and with a momentum larger than $p_{mean} - 2\sigma_p$ have been selected. The final sagitta distributions are shown in Figure 5.11 for the -44 mV threshold. The sagitta resolution values with errors obtained with a Gaussian fit are reported in Table 5.2.

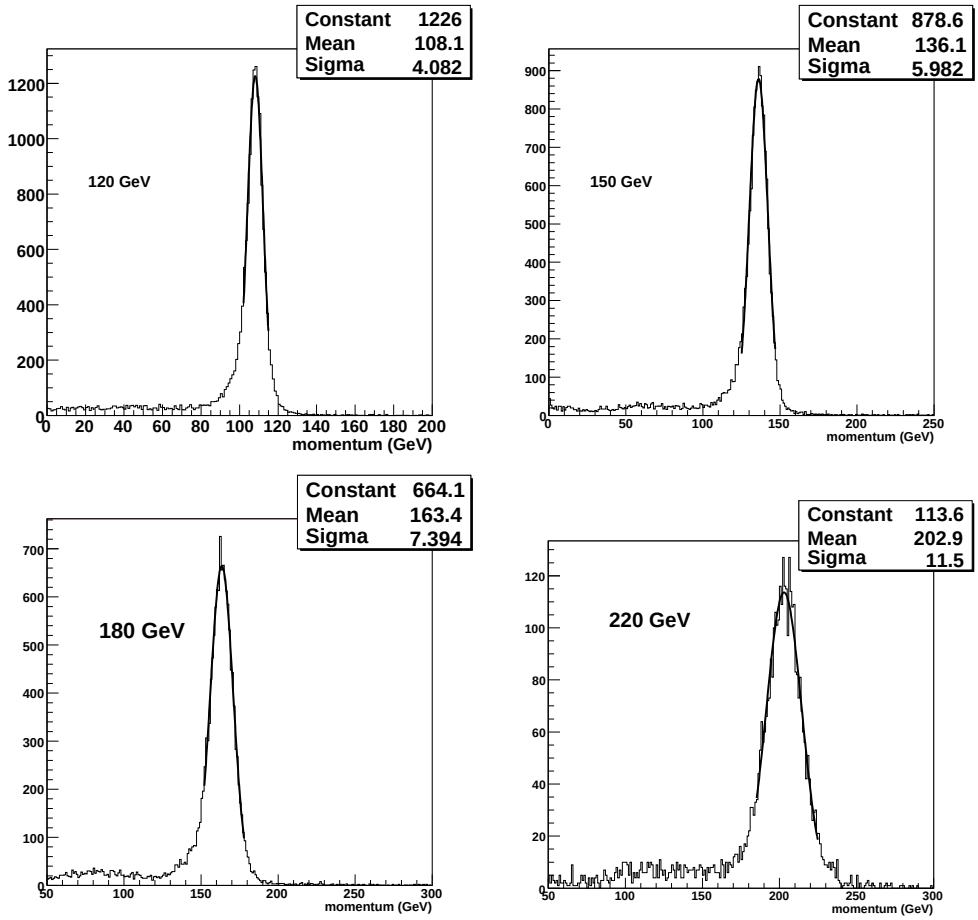

Figure 5.10: *Measured momentum distributions for the different samples at* $-44\ mV$ *threshold.*

Nominal momentum (GeV)	$-36\ mV$		$-40\ mV$		$-44\ mV$	
	p_{mean} (GeV)	σ_p (GeV)	p_{mean} (GeV)	σ_p (GeV)	p_{mean} (GeV)	σ_p (GeV)
100	88.7	4.5	88.8	4.2		
120			108.0	4.2	108.1	4.1
150	136.9	6.1	135.0	5.8	136.1	6.0
180	163.5	7.5			163.4	7.4
220	203.2	11.6	206.7	11.3	202.9	11.5
250	229.4	14.9	230.1	15.1		

Table 5.1: *Measured momentum mean value* (p_{mean}) *and the standard deviation* (σ_p) *at different nominal momenta for the three thresholds.*

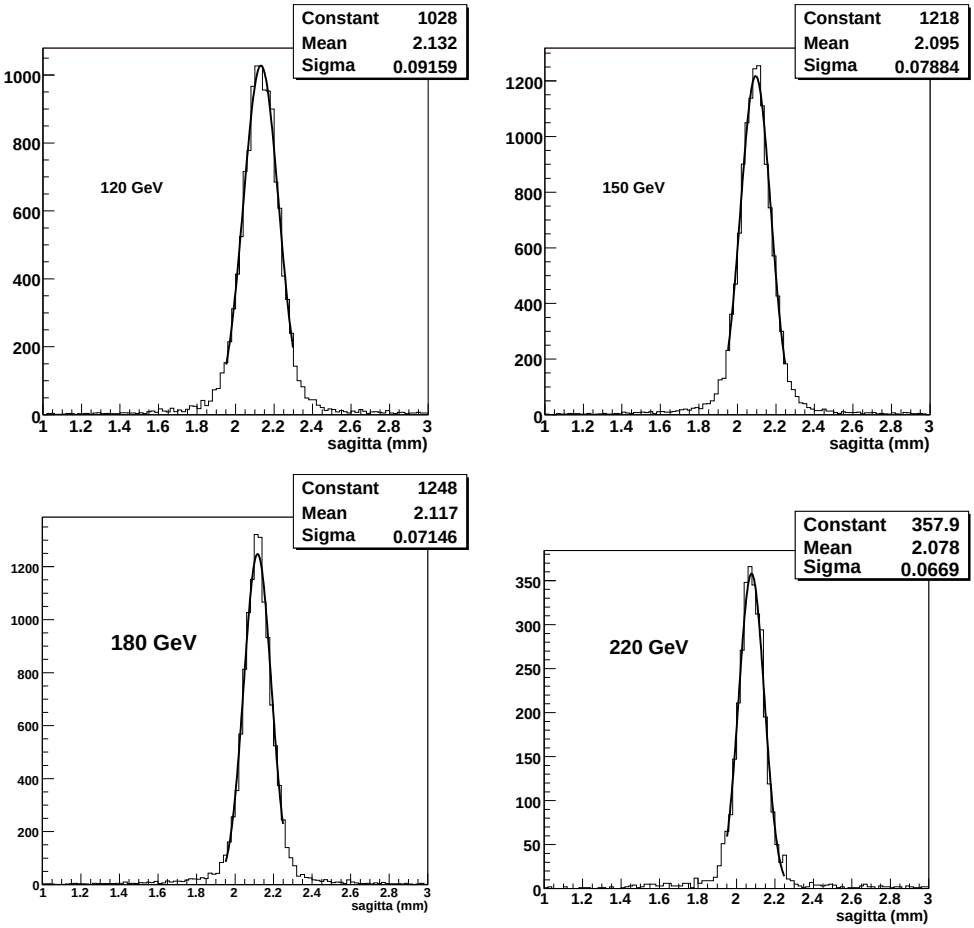

Figure 5.11: *Measured sagitta at different momentum beam for the* $-44\ mV$ *threshold.*

Nominal momentum (GeV)	$-36\ mV$ σ_S (μm)	$-40\ mV$ σ_S (μm)	$-44\ mV$ σ_S (μm)
100	97.99 ± 2.49	101.8 ± 1.1	
120		90.56 ± 0.79	91.59 ± 1.00
150	74.90 ± 1.10	76.46 ± 0.62	78.84 ± 0.82
180	70.15 ± 1.40		71.46 ± 0.71
220	62.99 ± 1.57	65.00 ± 2.00	66.9 ± 1.20
250	59.61 ± 1.96	62.0 ± 1.40	

Table 5.2: *Measured sagitta resolution at different nominal momenta.*

5.8 The GEANT4 Test Beam Simulation

The simulation of the H8 Test Beam has been performed with GEANT4 (see Section 3.6.1) running in the ATHENA framework. The package `CTB_G4Sim` handles the full Combined Test Beam (CTB) simulation, describing in detail the Inner Detector, the LAr and Tile Calorimeters and the muon chambers inner structures and positions in the CTB global reference system, as displayed in Figure 5.12

The ATHENA `SingleParticle` generator has been used to produce the muon beam. Beam momentum composition and angular distribution have been tuned on the real data measurements. In the present simulation, it has been took advantage of the muon momentum measurements performed using the barrel chambers to realistically describe the muon beam. Any additional detector or dead material upstream the muon sector has been removed from the simulation, this has been estimated the best way to stay close to the real data for sagitta comparison, avoiding uncertainties coming from beam interactions with the other sub-detectors.

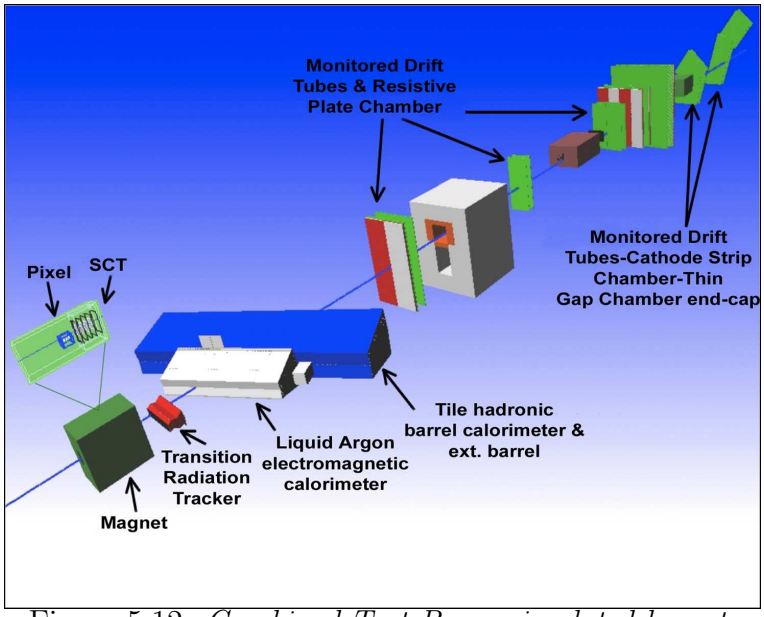

Figure 5.12: *Combined Test Beam simulated layout.*

The digitization methods adopted in [97] allows to use parametric *r(t)* relations. Here different resolution curves from experimental measurements ([100]) have been chosen, according to the selected discriminator thresholds. The signal propagation along the wire is not considered here. The contribution of this effects to the tube resolution has been estimated to be negligible. As a first check of digitization procedure, data and simulation residuals have been compared finding a good agreement, as shown in Figure 5.13.

The simulation has been optimized to describe secondary particle production and hard scattering inside the tube, internal tracks and muon hits shielded by secondaries. The analysis foresaw comparisons at different discriminator thresholds and accordingly, a cut on the energy released by muons in the sen-

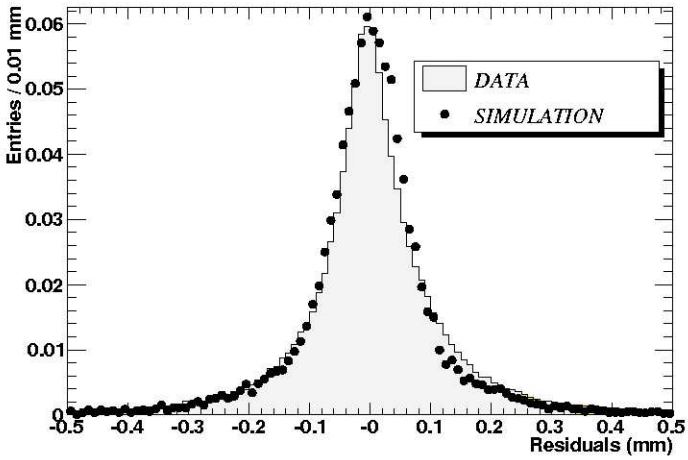

Figure 5.13: *Residuals for the real data and simulation.*

sitive gas has been applied at the simulation level (respectively, 575 eV for the -36 mV threshold or 21.3 primary electrons (PE), 640 eV for the -40 mV threshold or 24 PE, 705 eV for the -44 mV threshold or 26 PE).

The same reconstruction algorithm, MOORE, running on the real data samples has been used for the pattern recognition and track fitting performed on simulated data. The same version of the Detector Description, contained in NOVA database ([99]), has been used in simulation, digitization and reconstruction.

5.9 Sagitta Resolution versus Momentum

The three curves of the measured sagitta resolution versus the measured momentum at the different thresholds are shown in Figure 5.14 for real data using the sagitta resolution values reported in Table 5.2, and the mean values of the beam momentum reported in Table 5.1. Figure 5.15 shows the same curves but obtained with GEANT4 simulation.

The measured sagitta resolution depends mainly on two independent terms: the intrinsic resolution, that is a constant term independent from beam momentum, and the multiple scattering, that depends on muon momentum. The points of Figures 5.14 and 5.15 have been fitted with function (5.9.1):

$$\sigma = \sqrt{P_1^2 + (P_2/p)^2} \tag{5.9.1}$$

P_1 is the constant term related to intrinsic resolution, P_2 is the term related to multiple scattering.

The term of intrinsic resolution obtained from the fit at the different threshold for both real data and simulated ones are reported in Table 5.3.

The P_2 term can be translated in to the term $< x/X_0 >$ that is the average

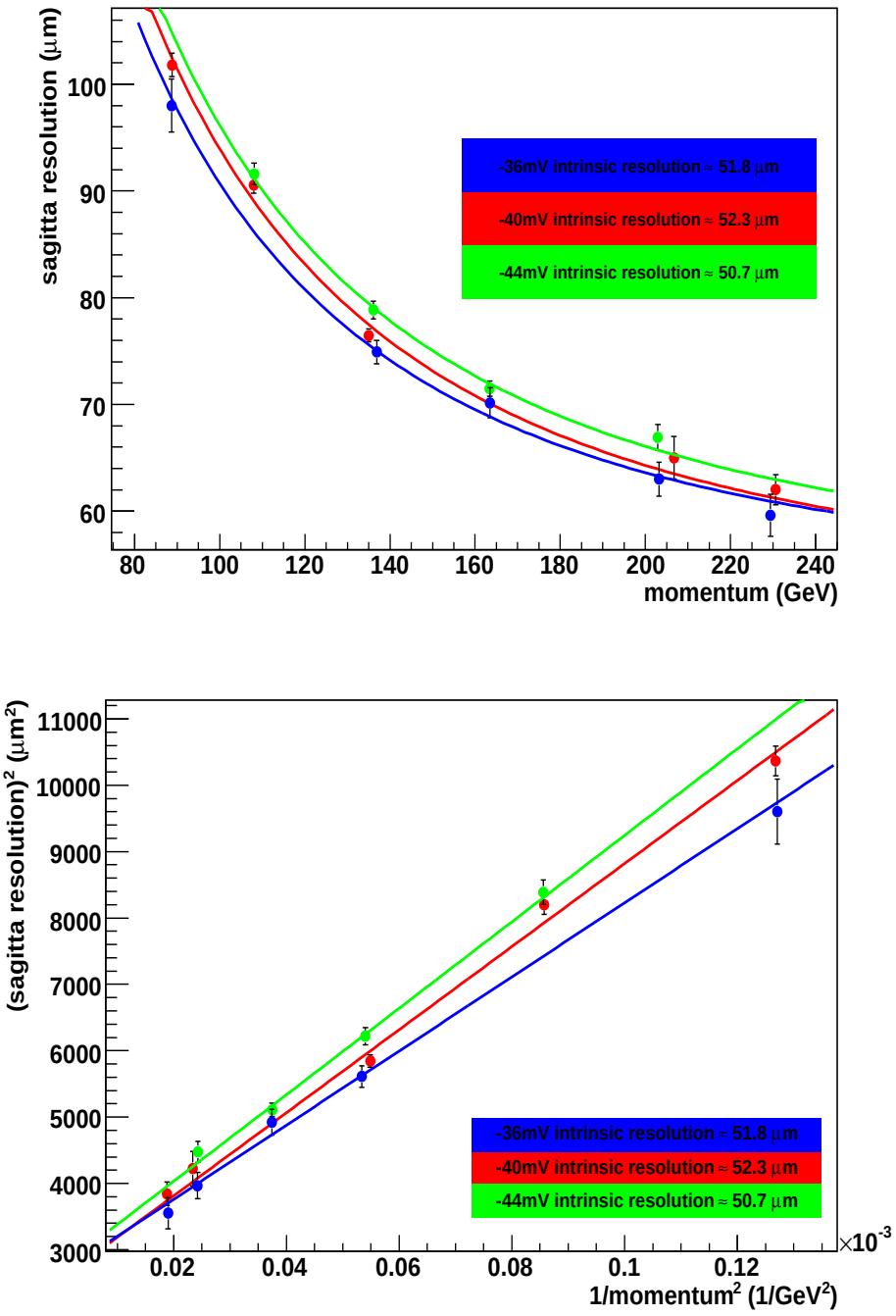

Figure 5.14: *Sagitta resolution as a function of momentum (top) and as a function of* $1/P$ *(bottom) for real data. The extrapolation and its error when momentum tends to infinity are immediate in the bottom plot.*

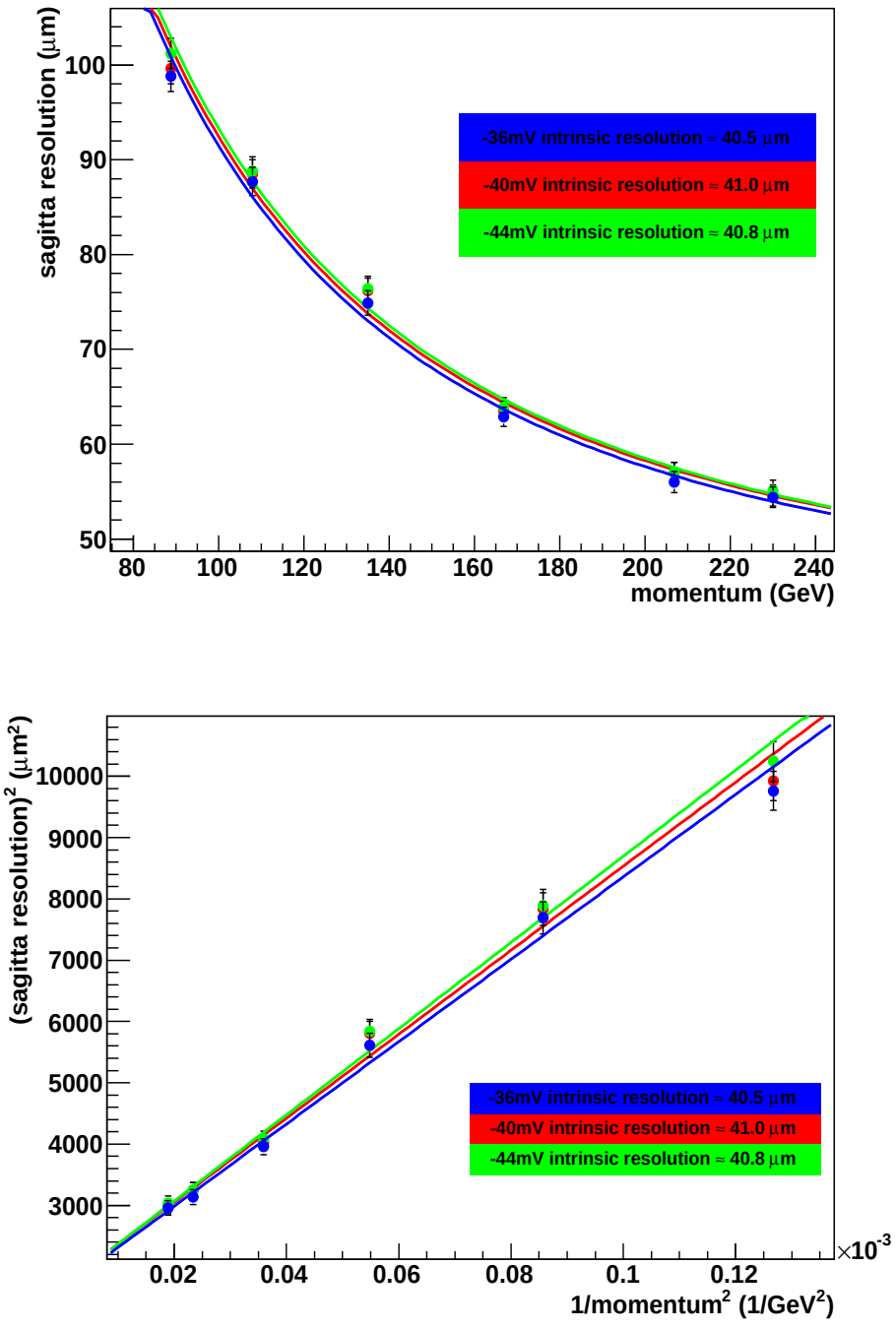

Figure 5.15: *Sagitta resolution as a function of momentum (top) and as a function of* $1/P$ *(bottom) for simulated data.*

Threshold (mV)	Intrinsic sagitta resolution Real Data (μm)	Intrinsic sagitta resolution Simulated data (μm)
-36	51.8 ± 1.9	40.5 ± 1.4
-40	50.7 ± 1.5	41.0 ± 1.4
-44	52.3 ± 1.7	40.8 ± 1.4

Table 5.3: *Intrinsic sagitta resolution values obtained by fit at the different thresholds both for real data and simulated ones.*

distance crossed by the track in radiation length units. The plan reported in Figure 5.16 has been used to perform the calculation. It has been supposed the scattering happens exactly in the BML super-point.

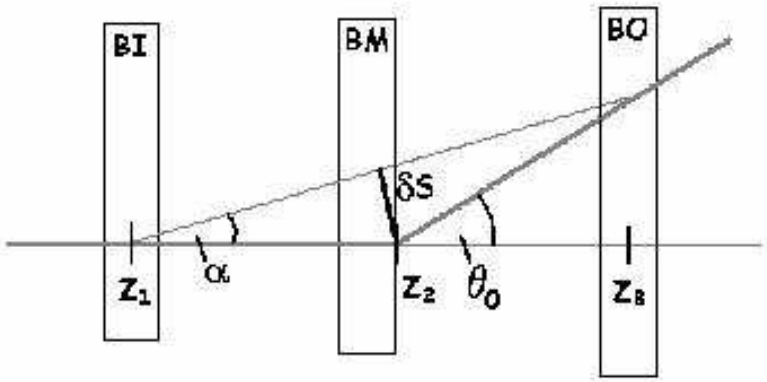

Figure 5.16: *A top schematic view of the barrel chambers. The method to valuate the multiple scattering contribute to sagitta resolution is schematized.*

The sagitta resolution term related to multiple scattering is given by the formula :

$$\sigma_s(multiple\ scatt) = \frac{P_2}{p} \simeq \frac{(Z_2 - Z_1)(Z_3 - Z_2)}{(Z_3 - Z_1)}\sigma_{\theta_0} \tag{5.9.2}$$

where $(Z_2 - Z_1), (Z_3 - Z_2)$ and $(Z_3 - Z_1)$ are the known distances between the chambers, σ_{θ_0} is the r.m.s. of the multiple scattering angle. It is given by the formula ([96]):

$$\sigma_{\theta_0}(rad) = \frac{13.6MeV}{p}\sqrt{x/X_0}[1 + 0.0038ln(x/X_0)] \simeq \frac{13.6MeV}{p}\sqrt{x/X_0}. \tag{5.9.3}$$

Substituting (5.9.3) in (5.9.2), the relationship between P_2 and $< x/X_0 >$ is given by the following expression:

$$P_2 \simeq \frac{(Z_2 - Z_1)(Z_3 - Z_2)}{(Z_3 - Z_1)} 13.6 MeV \sqrt{< x/X_0 >} \tag{5.9.4}$$

The values of $< x/X_0 >$ obtained by the fit both on real data and simulated ones are reported in Table 5.4. This term accounts for about 9 mm of aluminum of MDT tubes and for the material of the two RPC chambers.

Threshold	$< x/X_0 >$ Real Data	$< x/X_0 >$ Simulated data
-36	26.1 ± 2.1	31.5 ± 1.9
-40	29.3 ± 1.0	33.2 ± 2.0
-44	30.5 ± 1.7	33.0 ± 1.2

Table 5.4: $< x/X_0 >$ *values obtained by fit at the different thresholds both for real data and simulated ones.*

5.10 Conclusions

The sagitta resolution as a function of the muon momentum has been measured for momenta ranging from 100 GeV to 250 GeV, and for various electronic thresholds of the MDT precision chambers.

The beam momentum was measured at the entrance of the barrel Muon Spectrometer sector, to account for energy losses in the upstream material, and remove tails in the beam energy distribution. The sagitta resolution has then been measured as a function of the muon momentum, allowing thus to disentangle the two contributions coming respectively from multiple scattering and intrinsic resolution of the tracking detectors. The intrinsic resolution has been found to be ~ 50 μm in according with the value estimated in the ATLAS Muon Spectrometer technical proposal (see Section 2.6). In particular an intrinsic sagitta resolution of (50.7 ± 1.5) μm has been measured for an MDT threshold of -40 mV, the threshold chosen for the ATLAS experiment.

The multiple scattering and the intrinsic sagitta resolution measured on the Test Beam data have been compared with the GEANT4-based simulation of the H8 setup. The ATLAS offline framework ATHENA was used for both events reconstruction and simulation. It is important underline that in simulation the uncertainties on the wire locations and the chamber alignments have been not taken into account.

The good agreement found constitutes an important validation of the Spectrometer simulation, in terms of detector material description and detector response modeling (digitization).

Chapter 6

Gamma and Neutron Irradiation Tests of MDT Chambers

ATLAS MDT chambers (see Section 2.6.1) have to operate for more than 10 years in the harsh LHC background environment due mainly to low energy photons and neutrons. The expected overall maximum counting rate is about 500 Hz/cm^2. For a gas gain of 2×10^4, the overall accumulated charge can be as high as 0.6 $C/cm/wire$, which the MDTs must be able to withstand in 10 years of LHC operations. In addition, problems in tracking and pattern recognition may arise. Moreover, the foreseen upgrade to Super-LHC ($L = 10^{35}cm^{-2}s^{-1}$) ([101]) will involve background rates ten times higher.

After prolonged activity under high particle rates, wire chambers can be subject to a performance degradation; some deposits on the anode, as films or protrusions, can be found. This effect, mainly dependent on the operative conditions such as gas mixture and high voltage, manifests itself as a loss of gas gain. Moreover, high occupancy can affect track reconstruction: high hit multiplicity and spurious hits could mask the physical track signal.

To study the behaviour of MDT chambers under massive irradiation of gammas and neutrons at the level of Super-LHC, two extensive tests were performed at the Gamma and Neutron Facilities of the ENEA Casaccia Research Center ([102],[103]), irradiating two test detectors during 2005. These tests have been realized by the INFN groups of University of Calabria and Roma 3 University.

In this chapter, the analysis of the accumulated charge spectra for the monitoring of the chamber gas gain is presented, both at high background rate and after massive gamma and neutron irradiation.

6.1 Radiation Background in ATLAS Muon Spectrometer

High particles fluxes in the Muon System have a major impact on the Spectrometer design ([42],[33]). They influence parameters such as the rate capability of chambers, the aging of the detectors, the granularity and redundancy of the trigger instrumentation, the pattern recognition efficiency, or the momentum resolution tails induced by incorrect hit association.

The ATLAS muon instrumentation has been designed to offer the rate capability and robustness to the high occupancies required for running at nominal $L = 10^{34} cm^{-2} s^{-1}$ luminosity, including a safety factor 5 on estimated rate.

The background in the Muon Spectrometer can be classified into two categories ([104]):

- **primary background**: primary collision products penetrating particles into the Muon Spectrometer through the Calorimeter, which are correlated in time to the pp interaction. Conventional sources of primary background are semileptonic decays of light ($\pi, K \rightarrow \mu X$) and heavy ($c, b, t \rightarrow \mu X$) flavours, gauge boson decays ($W, Z, \gamma^* \rightarrow \mu X$), shower muons and hadronic punch-through. At small $p_T < 10\ GeV$, the largest component of the background are muons from π/K decays in flight. At moderate $p_T > 10\ GeV$, the cross-section is dominated by charm and beauty decays. At larger $p_T > 30\ GeV$, top and Z decays also give a sizable contribution.

- **radiation background**: gaseous background consisting mostly of neutrons and photons in the 1 MeV range, produced by secondary interactions in the forward Calorimeter, shielding material, the beam pipe and machine elements. Low-energy neutrons, which are an important component of the hadronic absorption process, escape the absorber and produce a gas of low-energy photons through nuclear $n - \gamma$ processes. This background enters into the Spectrometer from all directions and is not longer correlated in time to the primary pp interaction. Despite the detection efficiencies for neutrons and photons are very low, the low-energy neutral particle background will dominate the counting rate in most areas of the Spectrometer.

The absolute background rate predictions, shown in Figure 6.2, have been obtained with GCALOR ([105]) simulation for the Jan03 baseline geometry ([104]) averaged in scoring regions represented in Figure 6.1.

6.2 MDT Response to Background Radiation

6.2.1 Response to Neutrons

The absolute neutron fluences as a function of neutron energy expected in various regions of the Muon Spectrometer are shown in Figure 6.3 ([104]).

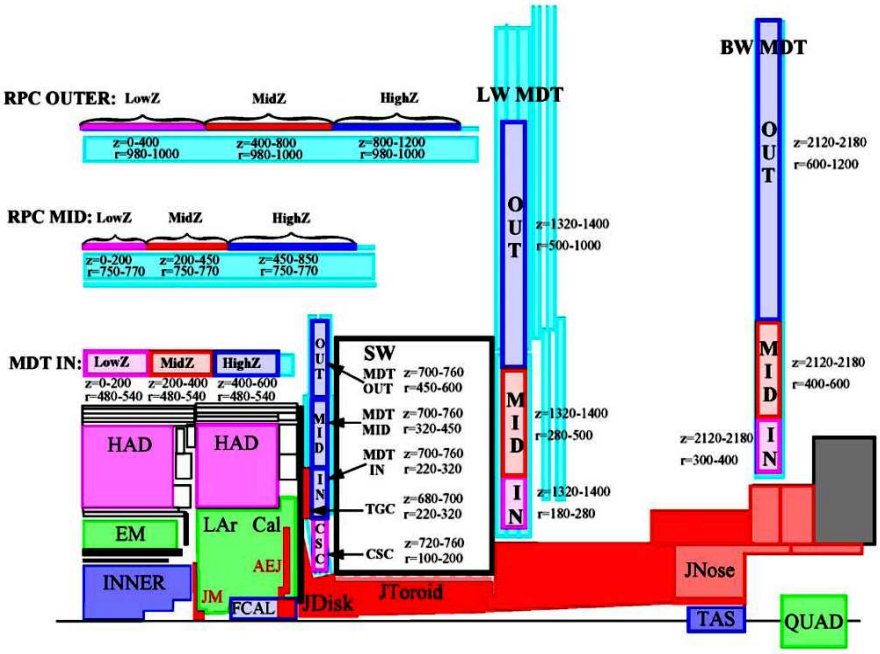

Figure 6.1: *Scoring regions used by GCALOR to quote fluences in the Muon System.*

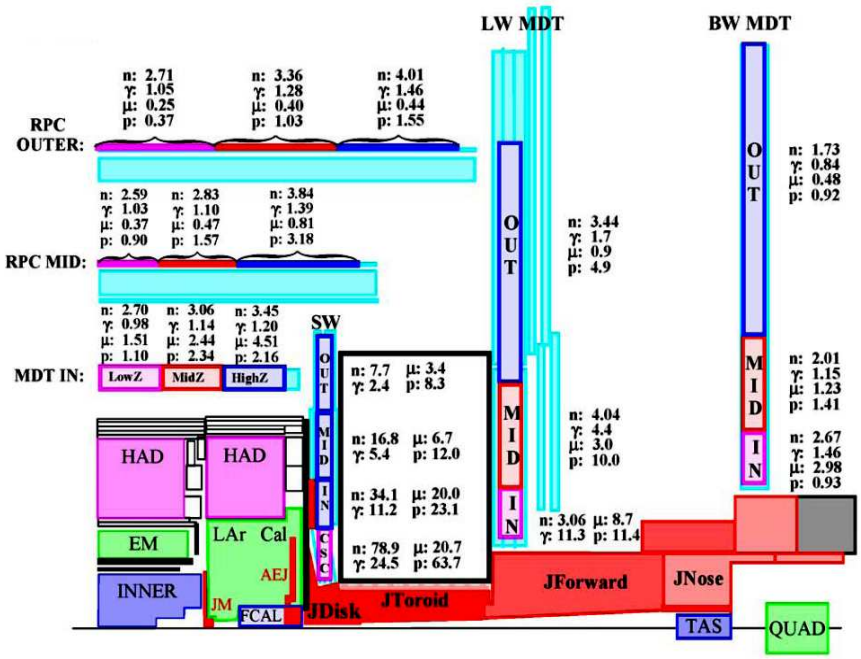

Figure 6.2: *Fluences in the muon chambers locations at high luminosity* $L = 10^{34} cm^{-2} s^{-1}$ *as predicted by GCALOR. The neutron and* γ *fluence is in units of* kHz/cm^2 *and the* μ *and proton fluence in* Hz/cm^2.

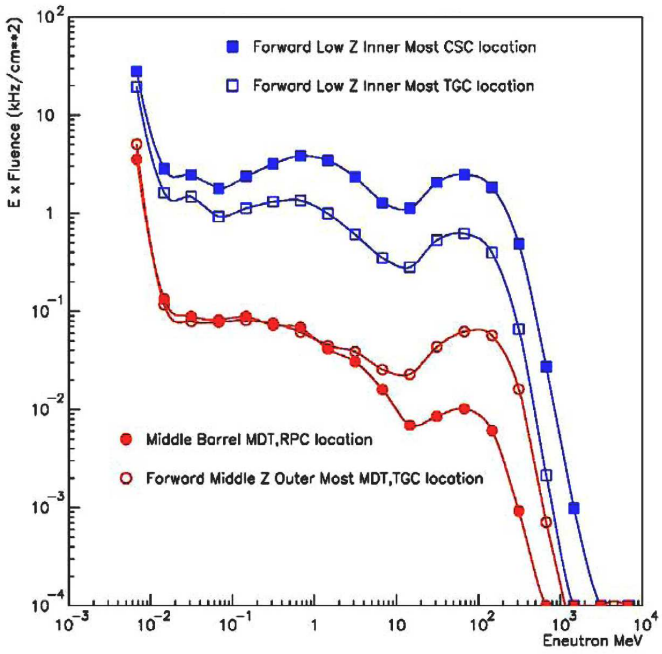

Figure 6.3: *Neutron fluences in various regions of the Muon Spectrometer: all neutrons with energies below* 10 KeV *are collapsed in a single bin. There are 6 orders of magnitude (or 12 bins) down to the thermal neutron energy.*

Neutron-induced background hits in drift tubes are due to a large variety of reactions. Above all the neutrons contribute to the photon spectrum via (n, γ) reactions. The thermal neutrons create background hits in the tubes due to β-decay following neutron capture in the counting gas or in the tube wall. The mean energy deposition from thermal neutron reactions is close to the 14 KeV ($\sim$ 540 ionization electrons) deposited on average by a minimum ionizing particle. Fast neutrons mainly give rise to background hits in the tube due to the recoil of nuclei and on average the energy deposited in the tube is about 14 KeV. At higher energies charged secondaries, mainly protons from quasi-elastic neutron scattering in the chamber wall or surrounding material are the source of the signal. The detection efficiency for neutrons in the MDT is shown in Figure 6.4 ([104]).

6.2.2 Response to Photons

The absolute photon rate as a function of photon energy expected in the middle barrel region of the Muon Spectrometer is shown in Figure 6.5 ([104]).

The detection efficiency for photons in the MDT chambers is shown in Figure 6.6 ([104]). The efficiency below 100 KeV is due to photo-electric effect in the gas, while the raising curve in the 1 MeV region is due to Compton scattering in either the counting gas or the tube wall. The magnetic field will curl the tracks of these low energy Compton electrons and the mean charge

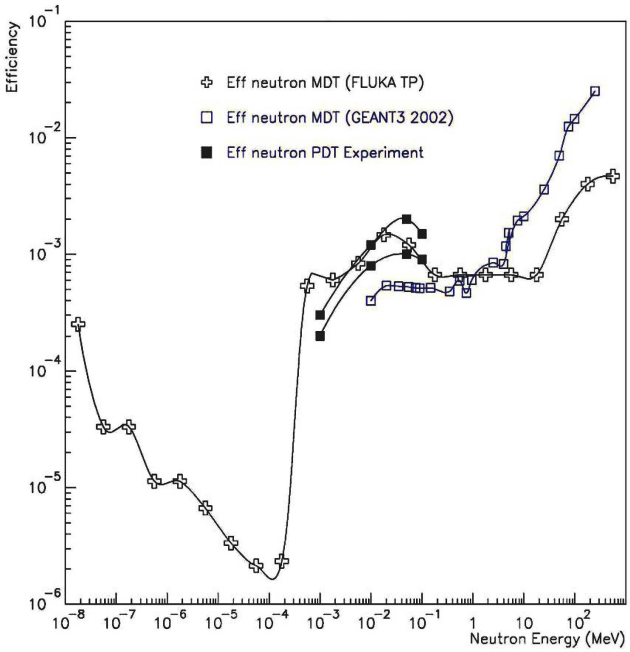

Figure 6.4: *MDT efficiency for neutrons.*

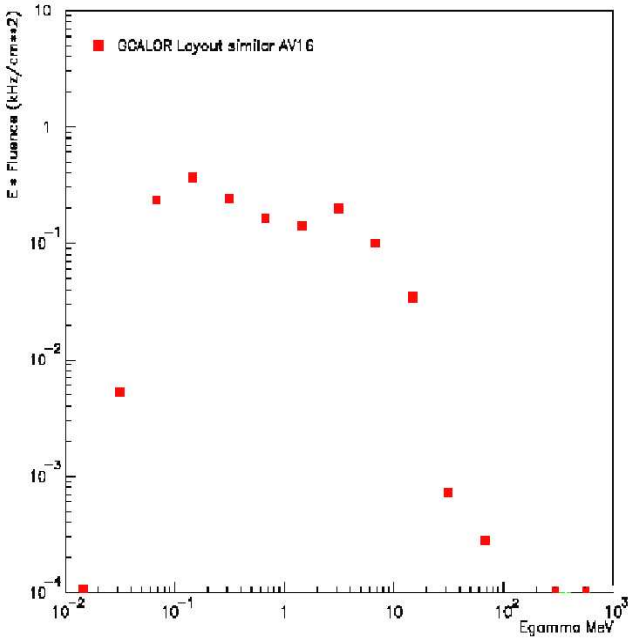

Figure 6.5: *The expected absolute photon rate as a function of photon energy in the middle barrel region of the Muon Spectrometer.*

deposed in the counting gas is about twice the charge deposited by a muon. Around 10 MeV, pair production becomes important and interactions in the material surrounding the chamber play an important role.

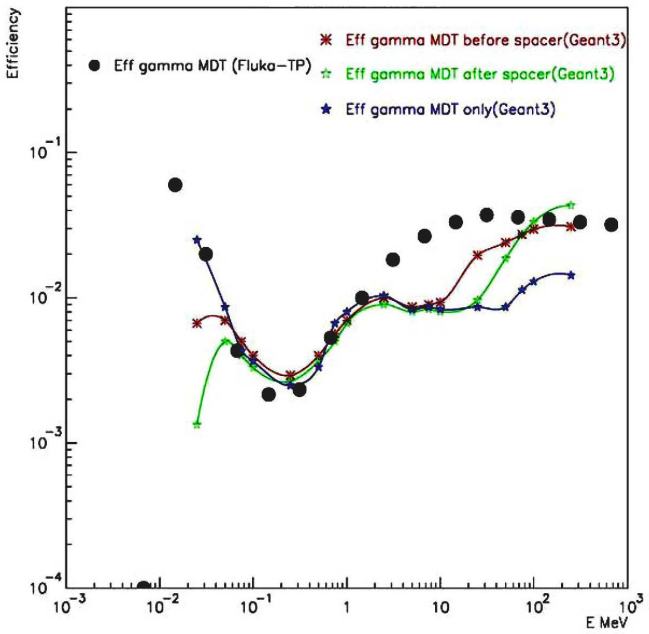

Figure 6.6: *Efficiency for photons in MDT chambers calculated with Geant simulation.*

6.3 The "Calliope" Gamma Facility

The "Calliope" gamma facility is a pool-type irradiation facility ([103],[106]) consisting in a high intensity ^{60}Co source in a large volume shielded cell. The radioisotope emits two photons of 1.17 MeV and 1.32 MeV. The activity of the source was 6.7×10^{14} Bq. The "Calliope" plant offers the possibility to choose the dose rate for sample irradiation and the maximum dose rate is about 5.4×10^3 Gy/h. The detectors under irradiation were placed at about 3.8 m far from the center of the source, where the measured dose in air resulted to be of 15.3 Gy/h corresponding to about 7.2×10^8 $photons/cm^2/s$.

6.4 The "Tapiro" Neutron Facility

The "Tapiro" nuclear reactor ([103],[106]) is a fast neutron source. The source has a cylindrical core with a radius of 6.20 cm and a height of 10.87 cm. The fuel is a metal alloy ($U98.5\%, Mo1.5\%$) with a fully enriched (93.5%) ^{235}U and its critical mass is 21.47 kg. The maximum neutron flux at the core center is 4×10^{12} $n/cm^2/s$ at the maximum nominal power of 5 kW. The test chamber

was hosted in the epithermal column where fast neutrons produced in the fission reactions are moderated towards epithermal energies. A sketch of the epithermal column is shown in Figure 6.7. The neutron energy spectrum at the position of the experimental setup ranges between 0.1 eV and 1 MeV and shows a broad peak around 1 KeV, as shown in Figure 6.8, and covers more than 8 orders of magnitude of the expected neutron energy range in the ATLAS Muon Spectrometer.

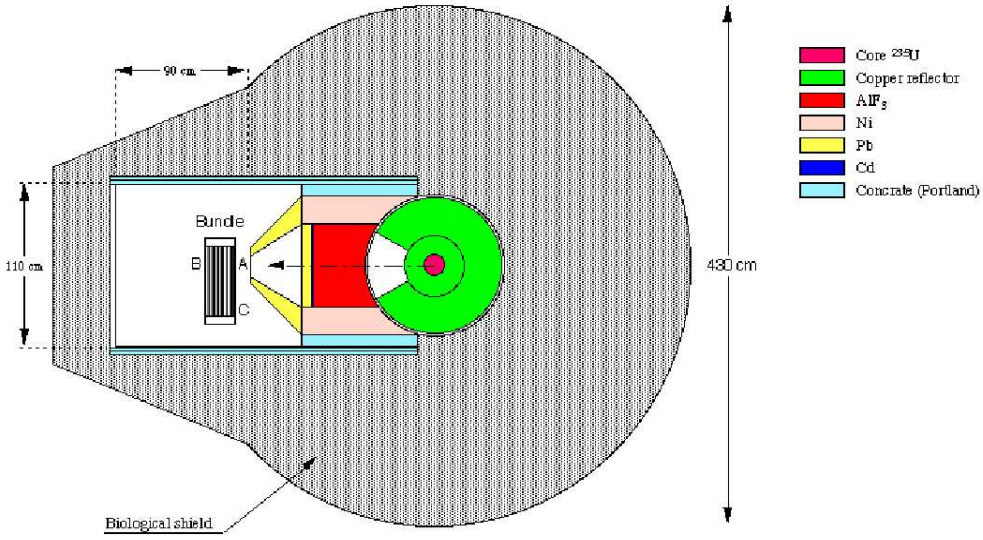

Figure 6.7: *Horizontal cross-section of the "Tapiro" nuclear reactor. The test detector in epithermal column is also visible.*

At the "Tapiro" neutron facility there are two photon background sources: gammas from the beam line associated with the nuclear reactions into the core and gammas from the surrounding material due to neutron absorption. In both cases, the energy of these gammas ranges in the 1 MeV region. The second component is relevant for the studies on the MDT performance in a high rate background, since the mean life of these excited nuclei is quite long ($\sim$ 10 hours) compared with the duration of a cosmic ray tracking run (typically 15 hours). From a previous experiment ([106]), the gamma dose in air at the maximum reactor power amount to $\sim 0.04\ Gy/min$ (corresponding to about $1.2 \times 10^8\ Hz/cm^2$).

6.5 The Test Detectors

48 identical drift tubes, 470 mm long, were built and tested following the standard ATLAS wiring and quality control procedure ([107],[42]) in the High Energy Laboratory of the University of Calabria. The two 6×4 drift tube chambers were built gluing together six tubes (placed one next to the other

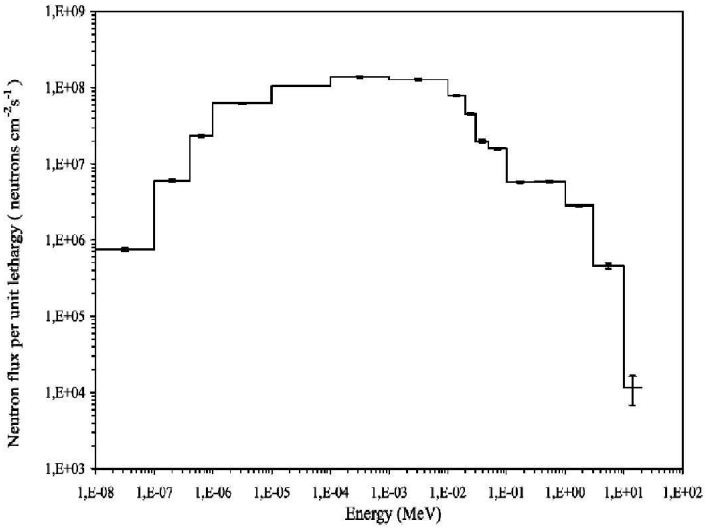

Figure 6.8: *Energy spectrum of the "Tapiro" nuclear reactor in the epithermal column.*

with a separation of 0.02 mm) to form each layer and then gluing the different layers one in top of the other. The wire pitch is expected to be 30.035 mm and the uncertainty on the wire position to respect the theoretical one has turned out to be less than 20 μm in the plane orthogonal to the wire. The chambers were equipped with the ATLAS on chamber gas distribution system components. The gas inlet and outlet to each chamber were provided by two aluminum manifolds connected to the tubes in the same layer connected with plastic rings. Each capillary supplies gas to three tubes in the same layer connected in series with the same plastic rings. The employed gas mixture $ArCO_2$ (97% : 7%) was supplied through bottles of a certified premixed gas. The pressure and the flux of the gas mixture into the chambers were regulated and measured through a pressure and mass flow meter controllers respectively. The gas tightness of the chambers was estimated by the pressure drop rate either before and after the irradiation period. The gas leak of all the two chambers resulted well under the ATLAS standard limits (2×10^{-8} $bar \cdot l/s$ *per tube*). The gas flow during the test period was 3.5 l/h per chamber, corresponding to about ten complete volume exchanges per day. After assembly, the chambers have been tested with cosmic rays in the Roma Tre INFN laboratory ([108]).

6.5.1 Front-end and DAQ Electronics

The MDT chambers are read out by a front-end chip (ASD) ([109]) mounted on a front-end board (mezzanine card). The ASD chip provides amplification, shaping and discrimination of the signals from the wires for a total of 24 channels. The discriminated signal is sent to the TDC ([110]) that measures the

threshold crossing time with a precision of 0.78 ns. The shaped signal is sent also to a Wilkinson ADC ([111]) that provides the measurement of the leading edge charge (the ADC gate can be set into the time interval $10 - 50$ ns at the leading edge of the signal). This information has been used as the diagnostic for monitoring the chamber gas gain. The sensitivity of the full analog signal chain for the expected signal range amounts to 10 mV/fC. The integration gate has been set to 25 ns and the discrimination threshold correspond to the collection of the first 23 primary electrons (PE). From previous studies on this front-end electronics ([108]), emerges that the sensitivity of this ADC at the working point, in terms of electrons collected at the anode wire, is about 1 $ADC_{channel}/0.85$ $PE = 1$ $ADC_{channel}/2.7$ fC. Note that each PE produce an avalanche with a multiplication factor $G_0 = 2 \times 10^4$ at the working point (3080 V anodic high voltage).

6.6 MDT Chamber Aging under Gamma Irradiation

6.6.1 Trigger System and Setup

Both chambers have been used for the gamma irradiation test. For each chamber, a coincidence of three scintillator counters was used as a trigger for cosmic rays. The counters were placed into two boxes and completely wrapped with a 2 cm thick layer of lead, two below the test chambers and the other in the one above. Figure 6.9 shows the final setup.

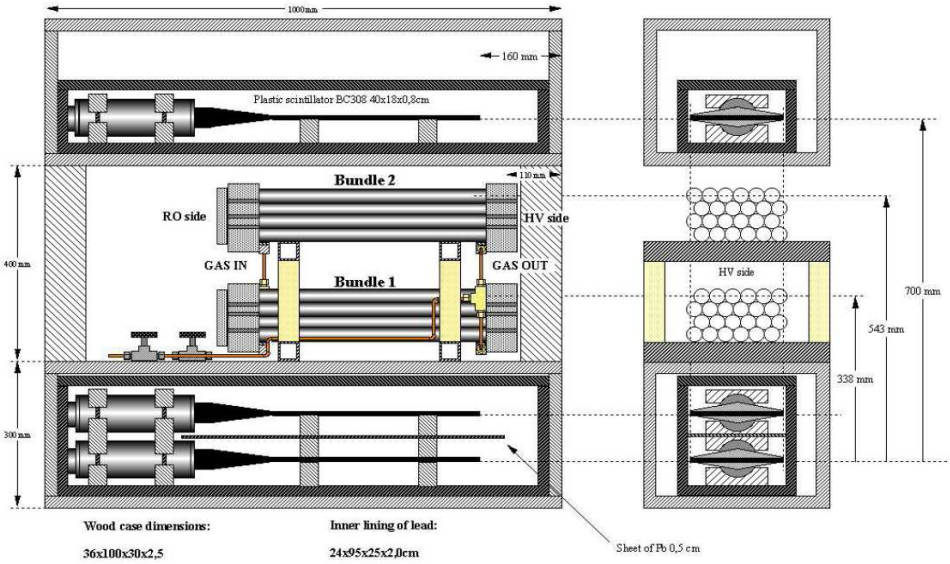

Figure 6.9: *"Calliope" test setup. The two test chambers with their electronics and the boxes containing the scintillator counters.*

6.6.2 Data Samples

Before starting the irradiation period, a run with cosmic rays trigger was taken and used as reference. While the ^{60}Co source was switched on, the chambers were operating at 3800 V with gas mixture at 1.1 bar. In fact, in standard conditions (3080 V and gas mixture at 3 bar), the current drawn by each tube under irradiation could not increase over about the measured value 15 μA because of space-charge accumulation. By rising the voltage and lowering the pressure, the current drawn by each tube could reach 1580 μA resulting in an accumulated charge of 4.8 $C/cm/wire$ at the end of the whole irradiation period, corresponding to $\sim$ 80 years of ATLAS data taking. Periods of photon irradiation were followed by data taking with the cosmic rays trigger and source turned off, with MDTs operated in standard conditions for performance monitoring. Five different runs are available for analysis corresponding to an average accumulated charge per tube of 0.0, 0.8, 1.3, 3.2, 4.8 $C/cm/wire$.

During the test, gas temperature (T), flow and absolute pressure (P) were continuously recorded.

6.6.3 Collected Charge Analysis

The measurement of the collected charge can be very useful to investigate variation in the tube gain and in the overall tube's response signal. The central region of the accumulated charge distribution can be fitted with the empirical function

$$f(x) = p_1 e^{-\frac{(x-p_2)^2}{xp_3}} \tag{6.6.1}$$

where p_2 is the value corresponding to the maximum of the distribution. In Figure 6.10 a fit of a typical ADC spectrum for a drift tube is shown.

The gas gain depends on the environmental conditions ([111]). Is it was decided to correct the peak value x_{max} to take into account temperature and pressure variations in each run with temperature $T+\Delta T$ and pressure $P+\Delta P$, with respect to the reference value T_0 and P_0 of the first run. The corrected $X_{max}^{T_0,P_0}$ value has been obtained applying in turn a temperature and pressure correction:

$$X_{max}^{T_0,P} = X_{max}^{T,P}\left(1 - 9.86\frac{\Delta T}{T_0}\right), \tag{6.6.2}$$

$$X_{max}^{T_0,P_0} = X_{max}^{T_0,P}\left(1 + 9.86\frac{\Delta P}{P}\right). \tag{6.6.3}$$

For each channel the relative variation of the peak position with respect to the reference run has been computed. The overall mean value has then been calculated for each run. In Figure 6.11 the mean relative variation of ADC

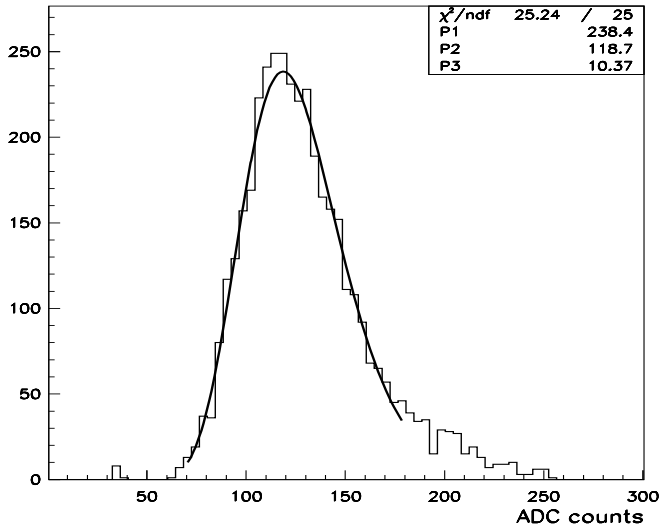

Figure 6.10: *Typical ADC spectrum and fit parameters.*

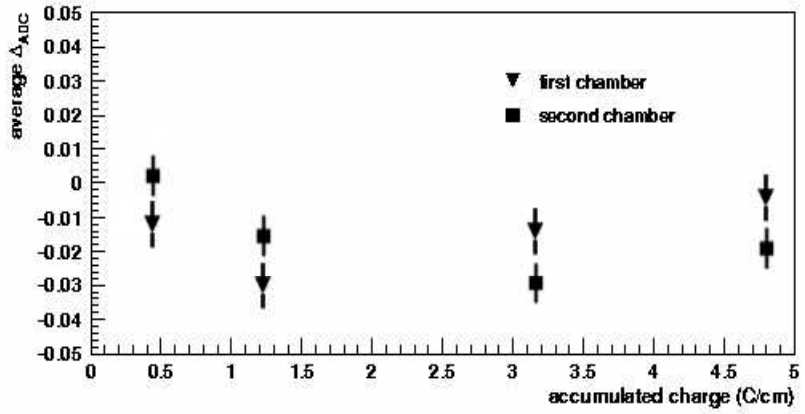

Figure 6.11: *ADC peak mean relative variation with respect to the accumulated charge for the two test chambers.*

peak position with respect to the accumulated charge is shown for both the test chambers. The mean standard deviation has been assumed as error on mean value. It can be seen that there are no gas gain drops: values are within 2 experimental standard deviations.

6.7 Massive Neutron Irradiation test

One of the two MDT bundles, already irradiated with photons at the "Calliope" facility, has been irradiated with neutrons. The main goals for the neu-

tron test were the search for ageing evidence on the drift tubes after gamma and neutron massive irradiation and the study of the tracking performances in an ATLAS-like high rate radiation environment using the reactor turned on at a low power.

6.7.1 Trigger System and Setup

The trigger was made of the coincidence of three scintillator counters contained inside two boxes wrapped in a layer of lead, 2 *cm* thick; Cadmium sheets and Boron powder were used to shield the scintillator from neutrons and improve the trigger performance when it was used with the reactor turned on at a low power. Figure 6.12 shows the final setup. Also the neutron beam line and the collimator are visible.

During the test, gas temperature, flow and absolute pressure were continuously recorded.

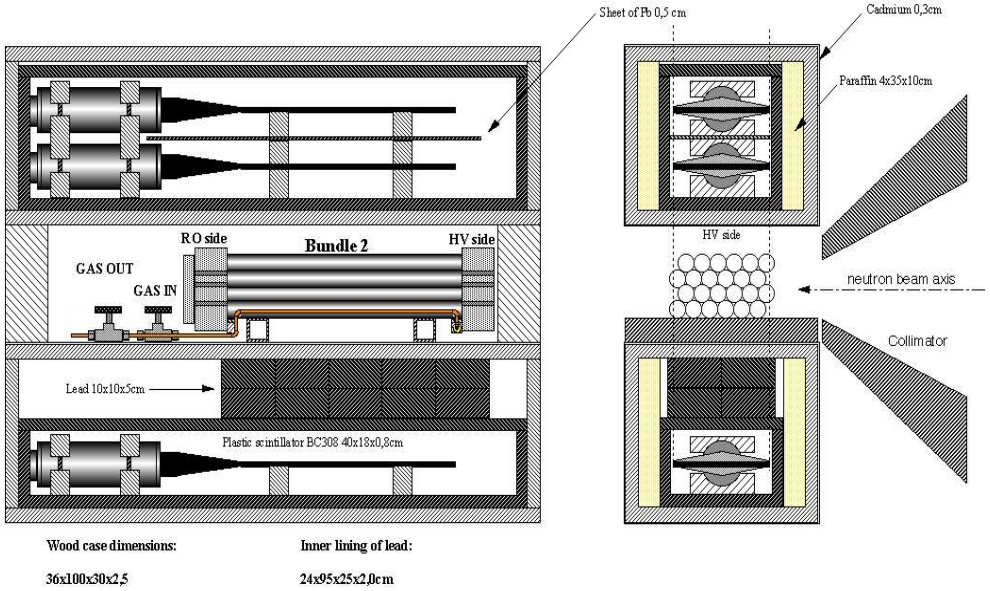

Figure 6.12: *Neutron test setup. The test chamber with its electronics and the boxes containing the scintillator counters. Neutron beam line and the collimator are visible.*

6.7.2 Data Samples

Dedicated data have been collected in order for aging and tracking performance studies. Before starting the neutron irradiation, a run with cosmic rays trigger was taken and used as reference.

To perform ageing studies, the chamber, operating at the standard ATLAS conditions, was exposed day-time for about 6-8 hours to neutron fluxes from $6.45 \times 10^6\ Hz/cm^2$ to $2.58 \times 10^7\ Hz/cm^2$ corresponding to "Tapiro" reactor

operating in a range of thermal power between 100 W and 400 W. During irradiation the trigger was switched off and no data were registered. Currents drawn by tubes were constantly monitored: they range about 5 μA to 8 μA per tube. Cosmic rays were acquired in runs of about 15 hours by switching on scintillators while the reactor was off. At the end of the irradiation period, 1.38×10^{12} n/cm^2 were integrated, corresponding $\sim$ 40 ATLAS years for a inner MDT positioned at high Z (see Figure 6.2).

To perform tracking studies in a ATLAS-like high rate environment, runs of about 6-8 hours were taken day by day with the reactor operating at a thermal power of 50 mW and 100 mW, corresponding to a neutron flux of 4×10^3 Hz/cm^2 and 8×10^3 Hz/cm^2 respectively. Between two subsequent irradiations, nightly data with cosmic rays were used to monitor any alteration in MDT behaviour.

Tables 6.1 and 6.2 summarize the collected data samples.

run number		**integrated flux** (n/cm^2)
reference	86	0
ageing	98	1.39×10^{11}
	99	4.08×10^{11}
	100	7.66×10^{11}
	113	1.38×10^{12}

Table 6.1: *List of runs for the neutron aging test and the integrated neutron flux.*

run number		**reactor power (W)**	**flux** (Hz/cm^2)
reference	86	0	0
tracking	89	50	4×10^3
	90	0	0
	91	50	4×10^3
	92	0	0
	93	50	4×10^3
	95	100	8×10^3

Table 6.2: *List of runs for the tracking sample: the reactor thermal power and the neutron flux are also reported.*

6.7.3 MDT Chamber Performances in a High Rate Background

Tracking in a high background environment could be difficult for several reasons. First of all a high count rate in a tube could affect the tube behaviour mainly for the modification of the electric field, because of the accumulation of

space-charge close to the wire. This can be investigated by studying the ADC response.

Making some pattern recognition can be complex if the number of hits in the chamber becomes larger. Moreover, background hits can mask track hits if they occur in the same tube (given the tube dead time of 700 ns) resulting in a loss of efficiency.

The distribution of hit multiplicity for the three sets of runs (reactor off, reactor at 50 mW and 100 mW) is given in figure 6.13. These distributions are normalized to 1 for comparison, as the run duration in the three cases was different. It emerges that turning the reactor on, the relative amount of both events with a large number of hits (due to neutron and photon hits) and events with few hits (0-3) (due to an increase of the trigger rate because of a not perfect trigger shielding) increase.

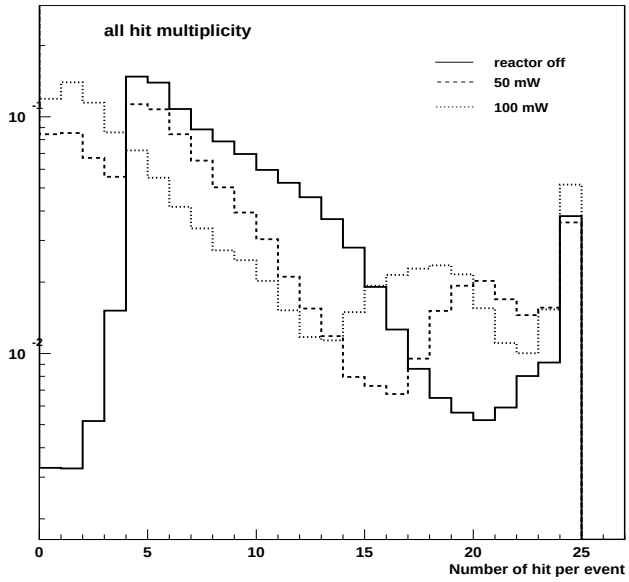

Figure 6.13: *Hit distribution per event: the reactor off distribution is well noticeable.*

To reduce background sources, only signals from 4 aligned tubes in a trigger gate fill the ADC distributions. Only data from the same tube are compared to exclude systematic errors like dependence on pramplifiers or slightly different gas mixtures. As the peak position depends on the drift distance of the primary electrons, it is appropriate to compare only pulses with the same drift distance to have a more precise measurement of the ADC peak position. Accumulated charge distributions have thus been studied in 10 drift distance intervals covering the whole tube radius. The central region of the accumulated charge spectra have been fitted with the empirical function as in Section 6.6.3, to get the peak position. As temperature and pressure were almost constant

over all the data taking period, no corrections on peak position have been applied. The peak position as a function of the drift distance for one of the tubes is shown in Figure 6.14. The curve reproduces the trend expected from MDT GARFIELD simulation ([112]) both for reactor on and off data. Variations between the three different environmental conditions are within the statistical errors. For the same tube the relative variation of the peak position for all the available runs with respect to the reference one is shown in Figure 6.15. Pulses correspond to drift distances ranging between 6 and 7.5 mm. No gas gain drops are visible compatibly to experimental errors. Similar behaviours have been found for all the drift tubes and for the other drift radius intervals.

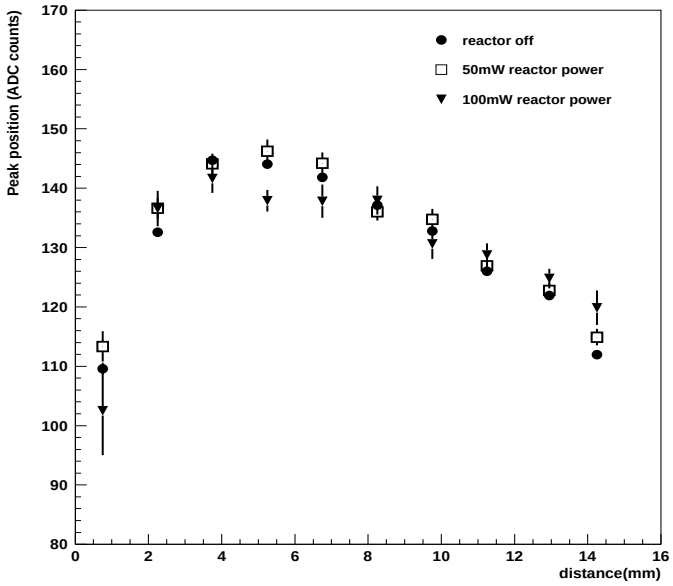

Figure 6.14: *ADC peak versus drift distance for a MDT drift tube and three different environmental conditions. The typical trend as predicted by MDT GARFIELD simulation is visible and no differences between the three data series are observed.*

6.7.4 Ageing Studies

ADC spectra analysis follows the strategy performed for the performance studies in a high rate background. As temperature and pressure were almost constant over all the data taking period, no corrections on peak position have been applied. In Figure 6.16 the ADC peak position as a function of the drift distance is shown for all the ageing data samples. The statistical error of the single peak position is $\sim 4\%$. No significative variations due to ageing effects are visible. Similar behaviours have been found for all the drift tubes.

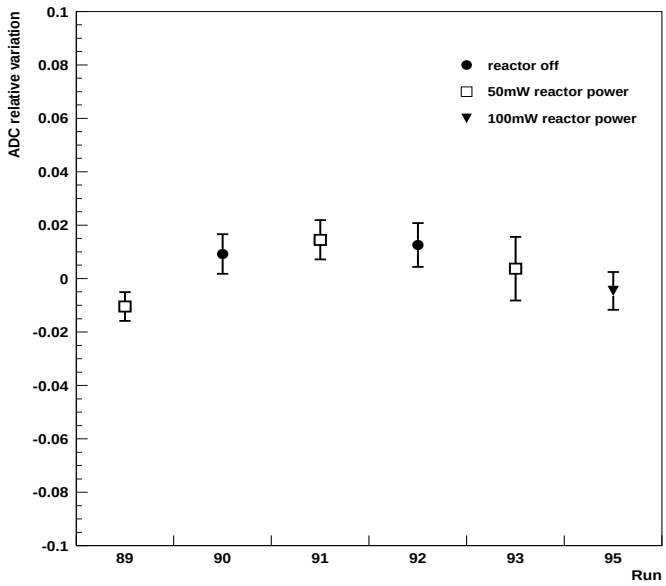

Figure 6.15: *ADC peak relative variation both for tracking and reactor off samples for one on the drift tubes.*

6.8 Conclusions

A complete analysis report on neutron and gamma irradiation tests can be found in [113], [114] and [115].

After the intensive gamma irradiation test on two final MDT test chambers, a charge of 4.8 C/cm per tube has been accumulated, corresponding to $\sim$ 80 years of ATLAS data taking. A good behaviour of the chambers has been observed. No significant gas drop is observed looking at the measured charge deposit. Additional kinds of analysis have been performed by the other members of the collaboration. Results are here summarized. The pressure drop rate before and after the irradiation period was measured and it turned out to be constant ($10^{-8}\ bar \cdot l/s$). This implies a stable behaviour of chambers and gas system instrumentation. Negligible variations of the drift properties results from drift time spectra and space-time relation studies and the single tube efficiency remains constant with increasing accumulated charge. No evidences of deposits or damages on the surfaces of the wires resulted from chemical SEM/EDX analysis.

An intensive irradiation campaign was carried out at the "Tapiro" nuclear reactor facility, at ENEA Casaccia laboratories, on a MDT test chamber. The main purpose were to study the MDT behaviour under ATLAS-like neutron rates, and to test chamber robustness after an integrated neutron flux corresponding to $\sim$ 40 years of real data taking, in view of the foreseen upgrade to Super-LHC. Cosmic ray data were acquired and analyzed to look for possible

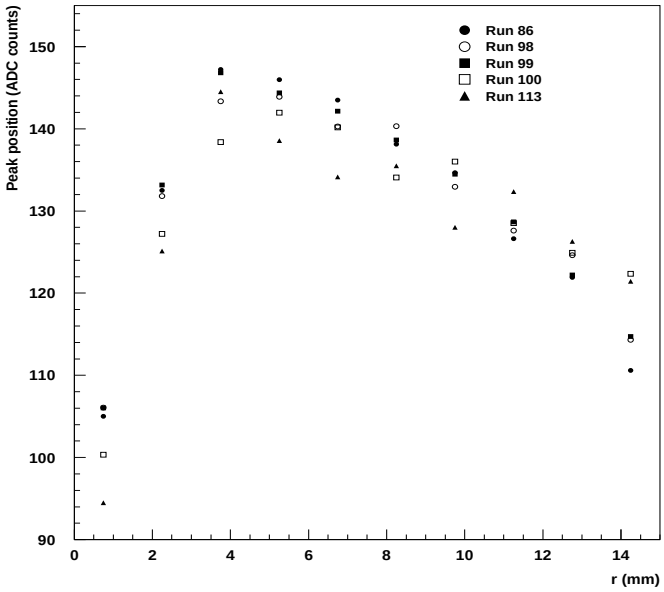

Figure 6.16: *ADC peak versus drift distance for a MDT drift tube for all the ageing data samples. The statistical error of the single peak position is* $\sim 4\%$. *No variations are visible within errors.*

loss in gas gain or tracking efficiency, and to validate some pattern recognition techniques in a dirty environment. No significant variation from the standard MDT behaviour was observed, neither at high background neutron rates, nor after massive irradiation. Also a chemical analysis on some wires surface was performed, by means of SEM and EDX techniques: no major pollution was found with respect to a reference sample taken from the same W-Re spool.

Conclusions

The work discussed in this thesis is divided into three main contributions: the study of the two rare $B^+ \to K^{*+}\mu^+\mu^-$ and $B^+ \to K^+\mu^+\mu^-$ decays, the study of the performance of the ATLAS Muon Spectrometer and the Monitored Drift Tube chamber behaviour after gamma and neutron massive irradiation.

The study on simulated data for the rare semileptonic B decays takes up a great part of this PhD thesis. These flavour changing neutral current decays occur via box or penguin diagrams, which make them very sensitive to physics beyond Standard Model. Moreover, $\Delta B = 1$ transitions are very weakly constrained experimentally and may thus reveal the limits of the CKM paradigm.

The event generation has been carried out using Pythia and EvtGen MonteCarlo generators both for signal and background samples. The event yields in 30 fb^{-1} integrated luminosity have been estimated using the GEANT4-based full detector simulation in the DC3 "detector as built" framework. GRID facilities have been extensively used for such simulation.

In spite of low statistics for background sample, the expected event yields and the $S/\sqrt{B}$ ratios have been assessed at a sufficient level to estimate the sensitivity on branching ratio measurements.

Assuming $\mathcal{BR}(B^+ \to K^+\mu^+\mu^-) = 0.34{\times}10^{-6}$ and $\mathcal{BR}(B^+ \to K^{*+}\mu^+\mu^-) = 0.97 \times 10^{-6}$, the events expected in 30 fb^{-1} are 4000 and 2300 at $S/\sqrt{B} = 35$ and $S/\sqrt{B} = 19$ respectively for the two channels.

These yields allow the measurement of the exclusive branching ratios with a relative (statistical) precision of $\sim 3.5\%$ for $B^+ \to K^+\mu^+\mu^-$ and $\sim 6.5\%$ for $B^+ \to K^{*+}\mu^+\mu^-$. This is better than the theoretical errors on the Standard Model estimates and thus sufficient to test the SM versus $SUSY$ theories predicting significant enhancements of these branching ratios.

Because of the clear dimuon signal, the ATLAS detector is well suited to study these decays and can reach good precision on measurements of physics parameters.

The present study will be improved by using more MonteCarlo data for background estimation, and considering pile-up effects to evaluate the possibility to extend the ATLAS studies on rare semileptonic B decays at running with nominal high luminosity ($L = 10^{34}\ cm^{-2}s^{-1}$).

The ATLAS Muon Spectrometer has been designed to provide a good stand-alone momentum measurement of high energy muons. The muon mo-

mentum will be measured by means of track bending in the magnetic field provided by large superconducting air-core toroidal magnets, using trigger and high precision tracking chambers. The transverse momentum is expected to be measured with a resolution $\Delta p_T/p_T = 10\%$ at $p_T = 1\ TeV$. To reach this performace, the instrinsic spatial resolution of the Muon System must be at level of 50 μm. This value has to account for intrinsic MDT tube resolution, calibration systematics, wire location and alignment.

The Muon Spectrometer 2004 test on the H8 beam line at CERN has given the possibility to measure the intrinsic resolution before the ATLAS installation. An intrinsic resolution of $(50.7 \pm 1.5)\mu m$ has been obtained, in complete agreement with the estimated value. This results is compatible with the one obtained by means of the GEANT4-based simulation. It is important to stress that this is an important validation test of the official ATLAS simulation software and that in this study the muon momentum has been measured for the first time using the Muon Spectrometer sub-detector.

MDT chambers, the precision tracking system of the ATLAS Muon Spectrometer, have to operate for more than 10 years in the harsh LHC background environment due mainly to low energy photons and neutrons. The expected overall maximum counting rate is 500 Hz/cm^2. Moreover, the upgrades for Super-LHC will involve background rates ten times higher. To study the MDT behaviour under gamma and neutron massive irradiation and in a high rate background, two tests were performed at the ENEA Casaccia Research Center Facilities, irradiating two MDT test detectors.

The ADC accumulated charge spectra analysis has been carried out in order to check for any gas gain drop due to ageing effects or space charge accumulation during tracking in an high rate background.

In the gamma irradiation test, a charge of 4.8 $C/cm/wire$ has been accumulated, corresponding to $\sim$ 80 years of ATLAS data taking. A good behaviour of the chamber has been observed. No significant gas drop is observed looking at the measured charge deposit.

For the neutron irradiation test, the main purposes were to study MDT behaviour under ATLAS-like neutron rates, and to test chamber robustness after an integrated neutron flux corresponding to $\sim$ 40 years of real data taking. No significant gas gain variations were observed, neither at high background neutron rates, nor after massive irradiation.

Bibliography

[1] A. Ali et al., *Improved Model-indipendent Analisys of Semileptonic and Radiative B Decays*, Phys. Rev. D **66**, 034002 (2002)

[2] A. Ali, *Review of Heavy Quark Physics - Theory*, hep-ph/0412128

[3] A.J. Buras, *Flavour Dynamics: CP Violation and Rare Decays*, hep-ph/0101336

[4] F. Mandl and G. Shaw, *Quantum Field Theory*, Jon Wiley & Sons, October 1993

[5] L. Itzykson et al., *Quantum Field Theory*, Mc Graw-Hill, 1980

[6] W.M. Yao et al., *Review of Particle Physics*, Journal of Physics **G 33**, 1 (2006)

[7] N. Cabibbo, *Unitary Symmetry and Leptonic Decays*, Phys. Rev. Lett. **10**, 531 (1963);
M. Kobayashi and K. Maskawa, *CP-Violation in the Renormalizable Theory of Weak Interaction* Prog. Theor. Phys. **49**, 652 (1973)

[8] L. Wolfenstein, *Parametrization of the Kobayashi-Maskawa Matrix*, Phys. Rev. Lett. **51** 1945, (1983)

[9] R. Fleischer, *Flavour Physics and CP Violation*, hep-ph/0405091

[10] G. Buchalla et al., *Weak Decays Beyond Leading Logarithms*, Rev. Mod. Phys.**68**, 1125 (1996)

[11] D. Wyler, *Goals and Methods of Flavour Physics*, CERN 2000-007

[12] A.J.Buras, *Weak Hamiltonian, CP Violation and Rare Decays*, hep-ph/9806471

[13] A.J.Buras, *Theoretical Review of B-Physics*, hep-ph/9509329

[14] A.J.Buras, *Flavour Dynamics: CP Violation and Rare Decays*, hep-ph/0101336

[15] E. Fermi, *An attempt of a theory of beta radiation*, Z. Phys. 88, 161-177 (1934)

[16] The BaBar Collaboration, *The BaBar Physics Book*, SLAC-R-504, P.F.Harrison and H.Quinn eds, October 1998

[17] N. Isgur and M.B. Wise, *Relationship between Form Factors in semileptonic $\bar{B}$ and D decays and exclusive rare $\bar{B}$ meson decays*, Phys. Rev. D **42** 2388, (1990)

[18] N. Isgur and M.B. Wise, *Weak Decays of Heavy Mesons in the Static Quark Approximation*, Phys. Lett. B **232**, 113 (1989)

[19] P. Ball, *Weak Decay Form Factors from QCD Sum Rules on the Light-Cone*, hep-ph/0306251

[20] K. Anikeev et al., *B-Physics at the Tevatron: RunII and Beyond*, hep-ph/0201071

[21] A. Ali et al., *A Comparative Study of the Decays $B \to (K, K^*)l^+l^-$ in Standard Model and Supersymmetric Theories*, Phys. Rev. **D 61** (2000)

[22] C. Bobeth et al., *Photonic penguins at two loops and m_t-dependence of $BR[B \to X_s l^+ l^-]$* , Nucl. Phys. **B 574**, 291 (2000)

[23] H.H. Asatrian et al., *Calculations of two-loop virtual corrections to $b \to s l^+ l^-$ in the standard model* Phys. Rev. **D 65**, 074004 (2000)

[24] A.H. Chamseddine et al., *Supergravity Unification*, Nucl. Phys. **B 101**, 145-153 (2001)

[25] A. Ali and E. Lunghi, *Extended minimal flavour violating MSSM and implication for B physics*, Eur. Phys. J. **C 21**, 683-700 (2000)

[26] Qi-Shu Yan et al., *Exclusive Semileptonic Rare Decays $B \to (K, K^*)l^+l^-$ in Supersymmetric Theories*, hep-ph/0004262

[27] C. Bobeth et al., *Analysis of Neutral Higgs-Boson Contributions to the Decays $B_s \to l^+l^-$ and $B \to K l^+ l^-$*, hep-ph/0104284

[28] A. Ishikawa et al. (The Belle Collaboration), *Measurement of Forward-Backward Asymmetry and Wilson Coefficients in $B \to K^* ll$*, Phys. Rev. Lett. **96**, 251801 (2006)

[29] K. Abe et al. (The Belle Collaboration), *Measurement of the Differential q^2 spectrum and Forward-Backward Asymmetry for $B \to K^{(*)} l^+ l^-$*, hep-ex/0410006

[30] B. Aubert et al. (The BaBar Collaboration), Measurements of branching fractions, rate asymmetries, and angular distributions in the rare decays $B \to Kll$ and $B \to K^* ll$, Phys. Rev. **D 73**, 092001 (2006)

[31] K. Desler and D.A. Edwards, *Accelerator Physics of Collider*, Review of Particle Physics, Phys. Lett. **B 592**,1 (2004)

[32] http://lhc.web.cern.ch/lhc/, Home Page

[33] ATLAS Collaboration, *ATLAS Technical Proposal for a General Purpose p-p Experiment at the Large Hadron Collider at CERN*, CERN/LHCC/94-43

[34] ATLAS Collaboration, *ATLAS Detector and Physics Performance Technical Design Report*, CERN/LHCC/99-15

[35] ATLAS Collaboration, *Inner Detector Technical Design Report*, CERN/LHCC/96-16

[36] R. Wigmans, *Advances in Hadron Calorimetry*, Cern-PPE/91-39

[37] R. Wigmans, *High Resolution Hadron Calorimetry*, Ferbel, Singapore, World Scientific, 1991

[38] ATLAS Collaboration, *Liquid Argon Calorimeter Technical Design Report*, CERN/LHCC/96-41

[39] R.L. Chase et al., *A Fast Monolithic Shaper for the ATLAS E.M. Calorimeter*, ATL-LARG-95-010

[40] Y. Jacquier et al., *Strengths and Weaknesses of Digital Filtering*, ATL-LARG-97-080

[41] ATLAS Collaboration, *Tile Calorimeter Technical Design Report*, CERN/LHCC/96-42

[42] ATLAS Collaboration, *ATLAS Muon Spectrometer Technical Design Report*, CERN/LHCC/97-22

[43] ATLAS Collaboration, *Trigger, DAQ and Computing Technical Design Report*, CERN/LHCC/2003-022

[44] ATLAS Collaboration, *ATLAS Trigger Performance*, CERN/LHCC/1998-15

[45] J. Baines et al., *Resource Estimates for the ATLAS B-Physics Trigger*, ATL-DAQ-COM-2002-013

[46] M. Smizănská, *ATLAS: B Physics Reach*, Eur. Phys J **C 34**, 385-392 (2004)

[47] LCG Project Collaboration, *LCG Technical Design Report*, CERN-LHCC-2005-024

[48] http://lcg.web.cern.ch

[49] ATLAS Collaboration, *ATHENA Developer Guide*, `http://atlas.web.cern.ch/Atlas/GROUPS/SOFTQARE/OO/architecture/General/Tech.Doc/Manual/2.0.0 DRAFT/AthenaUserGuide/pdf`

[50] http://atlas.web.cern.ch/Atlas/GROUPS/SOFTWARE/DC/

[51] D. Adams et al., *The ATLAS Computing Model*, ATL-SOFT-2004-007

[52] P. Nason et al., *The Total Cross Section for the Production of Heavy Quarks in Hadronic Collisions*,Nucl. Inst. Meth. **B 303**, 607-633 (1988)

[53] M. Wing, *Heavy Quark Production at HERA and the LHC*, hep-ex/0508038

[54] P. Nason et al, *Bottom Production*, hep-ph/0003142

[55] S. Baranov and M. Smizănská, *Beauty Production Overview from Tevatron to LHC*, ATL-PHYS-98-133

[56] B. Andersson et al., *Parton Fragmentation and String Dynamics*, Phys. Rep. **97**, 31 (1983)

[57] C. Peterson et al., *Scaling Violation in Inclusive e^+e^- Annihilation Spectra* Phys. Rev. **D 27**, 105-111 (1983)

[58] T. Sjöstrand et al., *Pythia 6.3 Physics and Manual*, hep-ph/0308153

[59] M. Smizănská, *PythiaB: interface to Pythia6 dedicated to simulation of beauty events*, ATL-COM-PHYS-2003-038

[60] *Pythia6 Tuning for B-physics simulations in ATLAS*, NOTE under preparation

[61] A. Ryd et al., *EvtGen: a MonteCarlo Generator for B-Physics*, BAD 522 V6

[62] M. Smizănská and J. Catmore, *EvtGen in ATLAS*, ATL-COM-PHYS-2004-041

[63] M. Dobbs and J.B. Hansen, *HepMC: a C++ Event Record for Monte-Carlo Generators*, http://cern.ch/HepMC/

[64] S. Agostinelli et al., *Geant4 - A Simulation Toolkit*, Nucl. Inst. Meth., **A 506**, 250-303 (2003)

[65] GEANT4, http://wwwasd.web.cern.ch/wwwasd/geant4/geant4.html

[66] A. Rimoldi et al., *The simulation of the ATLAS experiment: present status and outlook*, ATL-SOFT-2004-004

[67] D. Costanzo et al., *Validation of the* GEANT4*Based Full Simulation program for the ATLAS Detector: an overview of Performance and Robustness*, ATL-SOFT-PUB-2005-002

[68] ATLAS Collaboration, *Computing Technical Design Report*, CERN-LHCC-2005-002

[69] K.A. Assamagan et al., *Final report of the ATLAS AOD/ESD*, ATL-SOFT-2004-006

[70] D. Adams et al., *Track Reconstruction in the ATLAS Muon Spectrometer with MOORE*, ATL-SOFT-2003-007

[71] R. Brun et al., ROOT: an Object-Oriented data analysis framework, User Guide 5.12, http://root.cern.ch/

[72] R. Clifft et al., *IPATREC: inner detector pattern-recognition and track-fitting*, ATL-SOFT-1994-009

[73] N.C. Benekos et al., *ATLAS Inner Detector Performance*, ATL-INDET-2004-002

[74] https://uimon.cern.ch/twiki/bin/view/Atlas/AtlasCalorimeter

[75] D. Fassouliotis et al., *Muon Identification using the MUID package* ATL-COM-MUON-2003-003

[76] J. Shank et al., *Moore as Event Filter in the ATLAS High Level Trigger*, ATL-SOFT-2003-008

[77] T. Lagouri et al., *A Muon Identification and Combined Reconstruction Procedure for the ATLAS Detector at the LHC at CERN*, ATL-CONF-2003-011

[78] S. Tarem and N. Panikashvili, *Low p_T Muon Identification in the ATLAS Detector at the LHC*, ATL-SOFT-2004-003

[79] G. Blazey et al., *Run II Jet Physics*, hep-ex/0005012

[80] J. Catmore et al., *Writing B-physics analysis code in ATHENA*, ATL-COM-PHYS-2006-013

[81] http://tarta.home.cern.ch/tarta/vtx/docu.html

[82] J. Baines et al., *B decays at the LHC*, hep-ph/0003238

[83] D. Melikhov et al., *Investigation of rare semimuonic B-decays*, ATL-PHYS-96-083

[84] A. Policicchio and G. Crosetti, *Semileptonic Rare Beauty Decays in ATLAS and CMS*, Acta Physica Polonica **B** awaiting for pubblication, also available as ATL-PHYS-CONF-2006-011

[85] P. Reznicek, A. Policicchio et al., *Rare Beauty Decays in ATLAS*, ATLAS note under preparation

[86] P. Koppenburg, *Study of rare semileptonic B decays at LHCb*, LHCb-2000-076

[87] A. Policicchio et al., *Simulation and Reconstruction of Muon Events at the H8 TestBeam*, ATL-MUON-PUB-2006-006

[88] G. Avolio, A. Policicchio et al., *Barrel Sagitta Resolution versus Momentum at 2004 H8 Test Beam and Comparison with* GEANT4 *Simulation*, ATL-COM-MUON 2006-007

[89] The H8 Muon Community, *Proposed Measurement Program for H8 Muon System Test*, ATL-MUON-COM 2004-006

[90] T.A.M. Wijnen, *The MROD data format and the tower partitioning of the MDT chambers*, ATL-DAQ 2003-023

[91] G. Avolio et al., *Test of the first BIL tracking chamber for the ATLAS muon spectrometer*, Nucl. Instr. Meth. **A 523**, 309-322 (2004)

[92] P. Bagnaia et al, *CALIB: a Package for MDT Calibration Studies*, ATL-MUON-COM 2002-004

[93] P. Creti et al., *Results from the 1998 Test Beam of the Calypso chamber filled with an* $Ar - CO_2$ *gas mixture*, ATL-MUON-2000-006

[94] A. Biscossa et al., *Calypso: a full-scale MDT prototype for the ATLAS muon spectrometer* Nucl. Instr. Meth. **A 419**, 331-335 (1998)

[95] E. Meoni et al., *BIL chamber autocalibration results with 2001 H8 Test Beam data* ATL-MUON-COM-2002-026

[96] G.R. Lynch, O.I. Dahl, *Approximations to multiple Coulomb scattering*, Nucl. Inst. Meth. **B 58**, 6-10 (1991)

[97] D. Rebuzzi et al., GEANT4 *Muon Digitization in the* ATHENA FRAMEWORK, IN PUBBLICATION

[98] AMDB Web Page, `http://atlas.web.cern.ch/Atlas/GROUPS/MUON/AMDB_SIMREC/amdb_simrec.html`

[99] NOVA Parameter Database `http://atlassw1.phy.bnl.gov/NOVA/index.php3`

[100] M. Cirilli et al, *Results from the 2003 Beam Test of a MDT BIL chamber: systematic uncertainties on the TDC spectrum parameters and on the space-time relation*, ATL-MUON 2004-028

[101] O. Brüning et al., *LHC Luminosity and Energy Upgrade: A Feasibility Study*, CERN LHC Project Report 626 (2002)

[102] http://www.casaccia.enea.it

[103] S. Baccaro et al., *Gamma and Neutron Irradiation Facilities at ENEA-Casaccia Center*, Report CERN-CMS/TN, 95-192 (RADH) (1995)

[104] S. Baranov et al., *Estimation of Radiation Background, Impact on Detectors, Activation and Shielding Optimization in ATLAS*, ATL-GEN-2005-001

[105] C. Zeitnitz and T.A. Gabriel, *The GEANT-CALOR Interface User's Guide*, http://www.staff.uni-mainz.de/zeitnitz/Gcalor/gcalor.html

[106] S. Baccaro and A. Cecilia, *Facilities for Ratiation Hardness Qualification at ENEA-Casaccia (Roma-Italy)*, Proceedings of "2^{nd} SIRAD Workshop", Legnaro (Padova, Italy) 1-2 aprile 2004, ISBN 88-7337-007-1

[107] A. Aprile et al., *Production and test of monitored drift tubes for the muon spectrometer of the ATLAS experiment*, IEEE Transaction on Nuclear Science, 49-3 (2002) 1077

[108] A. Baroncelli et al., *Assembly and test of the BIL tracking chambers for the ATLAS Muon spectrometer*,Nucl. Instr. Meth. **A 557**, 421 (2006)

[109] C. Posh et al., *MDT-ASD: CMOS fron-end for ATLAS MDT chambers*, ATL-MUON-2002-003

[110] Y. Arai, *Development of front-end electronics and TDC LSI for the ATLAS MDT* , Nucl. Instr. Meth. **A 453**, 365 (2000)

[111] W. Blum and L. Rolandi,*Particle Detection with Drift Chamber*, Springer, Berlin, 1994

[112] A. Baroncelli et al., *Charge dependent corrections to the time reponse of BIL chambers at the Roma Tre cosmic test site*, Nucl. Instrum. Methods Phys. Res., **A 533**, 344 (2004)

[113] G. Avolio, A. Policicchio et al., *Monitored Drift Tubes aging under intensive gamma irradiation*, Nucl. Instr. Meth. **A 568**, 624-633 (2006)

[114] E. Meoni, A. Policicchio et al., *ATLAS MDT Chamber Massive Irradiation Test at Enea Casaccia Neutron and Gamma Facilities* , X Pisa Meeting on Advanced Detectors, to be published on Nucl. Instr. Meth. **A**

[115] P. Branchini, A. Policicchio et al., *Neutron irradiation test on ATLAS MDT chambers*, submitted to Nucl. Instr. Meth. **A**

List of Figures

List of Tables